

# **Insight into the Carbon Cycle from Continuous Measurements of Oxygen and Carbon Dioxide at Weybourne Atmospheric Observatory, UK**

Philip Wilson

Submitted in candidature for the degree of Doctor of Philosophy

University of East Anglia  
School of Environmental Sciences

October 2012



This copy of the thesis has been supplied on condition that anyone who consults it is understood to recognise that its copyright rests with the author and that use of any information derived there from must be in accordance with current UK Copyright Law. In addition, any quotation or extract must include full attribution

## **ABSTRACT**

Atmospheric measurements of carbon dioxide (CO<sub>2</sub>) and oxygen (O<sub>2</sub>) are a valuable tool to better understand the global carbon cycle. Technological improvements have resulted in near-real-time continuous measurements of both O<sub>2</sub> and CO<sub>2</sub> becoming viable. The increased time resolution of continuous measurements compared to discrete flask samples provides greater insight into atmospheric variations and short-term processes. These measurements will become even more relevant as the research focus shifts from the global to regional scale, for example anthropogenic emissions verification.

This thesis presents a 4.5 year record of atmospheric CO<sub>2</sub> and O<sub>2</sub> measurements made at Weybourne Atmospheric Observatory (WAO) on the north Norfolk coast in the United Kingdom. In situ, continuous measurements cover the period October 2007 to April 2012. Data for the tracer 'Atmospheric Potential Oxygen' (APO) are also presented.

The analytical methodology is described in detail and the data are examined on interannual, seasonal, synoptic and diurnal timescales. The precision of ambient air measurements is about  $\pm 0.03$  ppm for CO<sub>2</sub> and  $\pm 2.0$  per meg for O<sub>2</sub>. The average amplitude of the WAO seasonal cycle is 14.9 ppm for CO<sub>2</sub>, 134.2 per meg for O<sub>2</sub> and 59.0 per meg for APO, similar to other stations at similar latitudes. Interannual variability in the seasonal cycle amplitude is also investigated. Growth rates over the 4.5 year period are 2.4 ppm yr<sup>-1</sup> for CO<sub>2</sub>, -25 per meg yr<sup>-1</sup> for O<sub>2</sub> and -13 per meg yr<sup>-1</sup> for APO, also similar to other nearby stations. Short-term analyses reveal clear diurnal cycles in both CO<sub>2</sub> and O<sub>2</sub> that vary seasonally throughout the year. No diurnal cycle is observed in APO. A number of short-term events are explored and confirm that WAO experiences both clean marine air masses from the Arctic and North Atlantic, as well as fossil fuel pollution signals from the UK and continental Europe.

# TABLE OF CONTENTS

<b>ABSTRACT</b>	<b>2</b>
<b>TABLE OF CONTENTS</b>	<b>3</b>
<b>LIST OF FIGURES</b>	<b>5</b>
<b>LIST OF TABLES</b>	<b>8</b>
<b>ACKNOWLEDGEMENTS</b>	<b>9</b>
<b>CHAPTER 1 – INTRODUCTION</b>	<b>11</b>
1.1 Introduction to chapter	12
1.2 The carbon cycle	14
1.2.1 The global carbon cycle	14
1.2.2 Anthropogenic influence on the carbon cycle and the greenhouse effect	18
1.3 Oxygen	20
1.3.1 The role of oxygen in the global carbon cycle	21
1.3.2 Oxygen measurements	24
1.3.3 Atmospheric Potential Oxygen (APO)	27
1.4 Future directions of carbon cycle related research	30
1.5 Structure of this thesis	31
1.6 References	32
<b>CHAPTER 2 - METHODS</b>	<b>38</b>
2.1 Introduction to chapter	39
2.2 Air Inlets	40
2.3 Drying	41
2.4 Gas handling	45
2.5 Analysers	46
2.6 Data acquisition and software	51
2.7 Calibration	56
2.7.1 Theory behind Zero Tank corrections to the C-term of the CO <sub>2</sub> calibration equation	58
2.7.2 Target Tank role and results	62
2.7.3 Hierarchy and macro control of calibration	66

2.7.4	Stability of Working Tank concentrations	67
2.8	Intercomparison activities	69
2.9	References	73
<b>CHAPTER 3 – THE WEYBOURNE CO<sub>2</sub>, O<sub>2</sub> AND APO RECORDS</b>		<b>74</b>
3.1	Site description	75
3.2	Data analysis methods specific to this chapter	76
3.2.1	Hpspline curve fitting	76
3.2.2	Modelled results	77
3.3	Complete data record	78
3.4	Curve fitting details and results	84
3.4.1	Long-term trends	87
3.4.2	Examination of seasonal cycle	93
3.5	Comparison with model-predicted seasonality	100
3.6	References	103
<b>CHAPTER 4 – SHORT-TERM AND EVENT ANALYSIS OF THE WEYBOURNE RECORDS</b>		<b>107</b>
4.1	Introduction to chapter	108
4.2	Data analysis methods specific to this chapter	108
4.2.1	Particle dispersion model footprints	108
4.3	Diurnal cycles	109
4.4	Meteorological based filtering	116
4.5	Examination of pollution events	131
4.6	Examination of clean air and oceanic signals	138
4.7	References	142
<b>CHAPTER 5 – CONCLUSIONS AND OUTLOOK</b>		<b>144</b>
5.1	References	151
<b>ABBREVIATIONS</b>		<b>154</b>

## LIST OF FIGURES

<b>FIGURE 1.1:</b> Schematic of the greenhouse effect	13
<b>FIGURE 1.2:</b> Schematic of the global carbon cycle	15
<b>FIGURE 1.3:</b> CO <sub>2</sub> and O <sub>2</sub> concentrations as observed at Mauna Loa and the South Pole	21
<b>FIGURE 1.4:</b> Plot of O <sub>2</sub> /N <sub>2</sub> vs. CO <sub>2</sub> demonstrating the vector approach to balancing the global carbon budget	24
<b>FIGURE 2.1:</b> Gas handling schematic of the Weybourne Atmospheric Observatory (WAO) O <sub>2</sub> and CO <sub>2</sub> system	39
<b>FIGURE 2.2:</b> Photographs of an air inlet installed at WAO	40
<b>FIGURE 2.3:</b> Photograph of the four glass fridge traps in the refrigerator	42
<b>FIGURE 2.4:</b> Photographs of the chiller unit	44
<b>FIGURE 2.5:</b> Schematic of the Siemens Ultramat 6E CO <sub>2</sub> analyser	48
<b>FIGURE 2.6:</b> Plots demonstrating the 'ΔΔ' value used in O <sub>2</sub> measurements	50
<b>FIGURE 2.7:</b> Example of 'DIG' diagnostic plots	53
<b>FIGURE 2.8:</b> Screenshot of the 'Schematic' tab of the user interface of the WAO software	54
<b>FIGURE 2.9:</b> Screenshot of the 'Cylinders' tab of the user interface of the WAO software	55
<b>FIGURE 2.10:</b> Screenshot of the 'Macros/Calibration' tab of the user interface of the WAO software	55
<b>FIGURE 2.11:</b> Screenshot of the 'Settings/Dropbox' tab of the user interface of the WAO software	56
<b>FIGURE 2.12:</b> Plots of the CO <sub>2</sub> and O <sub>2</sub> values of Target Tank runs at WAO for the entire duration of the data record	63
<b>FIGURE 2.13:</b> Plots of the CO <sub>2</sub> and O <sub>2</sub> values of Target Tank runs at WAO since 2009	64
<b>FIGURE 2.14:</b> One hour of stable air data from WAO used to calculate system precision during measurement of outside air.	66
<b>FIGURE 2.15:</b> Plots of the variability in Working Tank mole fraction of CO <sub>2</sub> and O <sub>2</sub> for all Working Tanks	68

<b>FIGURE 2.16:</b> Plot of the variability in Working Tank mole fraction of O <sub>2</sub> for Working Tanks from October 2010 to April 2012	69
<b>FIGURE 2.17:</b> Results of Cucumber intercomparison cylinders run at WAO for both CO <sub>2</sub> and O <sub>2</sub>	71
<b>FIGURE 2.18:</b> Results of GOLLUM intercomparison cylinders run at WAO for both CO <sub>2</sub> and O <sub>2</sub>	72
<b>FIGURE 3.1:</b> Satellite image, map and photograph of WAO	75
<b>FIGURE 3.2:</b> The 3 regions used in the model runs	78
<b>FIGURE 3.3:</b> Complete 2-minute dataset of CO <sub>2</sub> , O <sub>2</sub> and APO from WAO 1 <sup>st</sup> October 2007 to 30 <sup>th</sup> April 2012	79
<b>FIGURE 3.4:</b> Hourly averaged dataset of CO <sub>2</sub> , O <sub>2</sub> and APO from WAO 1 <sup>st</sup> October 2007 to 30 <sup>th</sup> April 2012	80
<b>FIGURE 3.5:</b> Daily averaged dataset of CO <sub>2</sub> , O <sub>2</sub> and APO from WAO 1 <sup>st</sup> October 2007 to 30 <sup>th</sup> April 2012	81
<b>FIGURE 3.6:</b> Hpspline curve fits for CO <sub>2</sub> , O <sub>2</sub> and APO from WAO	85
<b>FIGURE 3.7:</b> Map showing positions of other atmospheric observatories	88
<b>FIGURE 3.8:</b> Annual CO <sub>2</sub> growth rates at WAO	91
<b>FIGURE 3.9:</b> Annual O <sub>2</sub> growth rates at WAO	91
<b>FIGURE 3.10:</b> Annual APO growth rates at WAO	92
<b>FIGURE 3.11:</b> UK annual CO <sub>2</sub> emissions from fossil fuel burning	93
<b>FIGURE 3.12:</b> Annual seasonal cycles of CO <sub>2</sub> , O <sub>2</sub> and APO at WAO	98
<b>FIGURE 3.13:</b> Comparison of modelled APO seasonality to curve fit	101
<b>FIGURE 4.1:</b> One week of data from WAO showing CO <sub>2</sub> , O <sub>2</sub> , APO, irradiance and temperature	111
<b>FIGURE 4.2:</b> Average diurnal cycle in CO <sub>2</sub> at WAO for each of the four seasons	114
<b>FIGURE 4.3:</b> Average diurnal cycle in O <sub>2</sub> at WAO for each of the four seasons	115
<b>FIGURE 4.4:</b> Wind and concentration roses for CO <sub>2</sub> , O <sub>2</sub> and APO at WAO	117
<b>FIGURE 4.5:</b> Wind and concentration roses of CO <sub>2</sub> , O <sub>2</sub> and APO during the winter months of December January and February at WAO	118
<b>FIGURE 4.6:</b> Wind and concentration roses of CO <sub>2</sub> , O <sub>2</sub> and APO during the spring months of March, April and May at WAO	119
<b>FIGURE 4.7:</b> Wind and concentration roses of CO <sub>2</sub> , O <sub>2</sub> and APO during the summer months of June, July and August at WAO	120

<b>FIGURE 4.8:</b> Wind and concentration roses of CO <sub>2</sub> , O <sub>2</sub> and APO during the autumn months of September, October and November at WAO	121
<b>FIGURE 4.9:</b> 2-minute WAO CO <sub>2</sub> , O <sub>2</sub> and APO data arriving from 90 – 180° (Europe)	124
<b>FIGURE 4.10:</b> 2-minute WAO CO <sub>2</sub> , O <sub>2</sub> and APO data arriving from 180 - 255° (southern England and London)	125
<b>FIGURE 4.11:</b> 2-minute WAO CO <sub>2</sub> , O <sub>2</sub> and APO data arriving from 255 – 330° (northern England and Scotland)	125
<b>FIGURE 4.12:</b> 2-minute WAO CO <sub>2</sub> , O <sub>2</sub> and APO data arriving from 330 – 90° (the North Sea)	126
<b>FIGURE 4.13:</b> Annual seasonal cycles of CO <sub>2</sub> from data filtered by wind sector	128
<b>FIGURE 4.14:</b> Annual seasonal cycles of O <sub>2</sub> from data filtered by wind sector	129
<b>FIGURE 4.15:</b> Annual seasonal cycles of APO from data filtered by wind sector	129
<b>FIGURE 4.16:</b> 1 week of CO <sub>2</sub> , O <sub>2</sub> and APO data from WAO starting on 8 <sup>th</sup> January 2010	133
<b>FIGURE 4.17:</b> Plot of O <sub>2</sub> concentration versus CO <sub>2</sub> concentration to determine O <sub>2</sub> :CO <sub>2</sub> ratio	134
<b>FIGURE 4.18:</b> NAME footprints of air sampled at WAO on the 13 <sup>th</sup> January 2010	135
<b>FIGURE 4.19:</b> three 1-week periods of CO <sub>2</sub> , O <sub>2</sub> and APO data from WAO for three events in the weeks starting on 12 <sup>th</sup> November, 3 <sup>rd</sup> and a7 <sup>th</sup> December 2010	137
<b>FIGURE 4.20:</b> NAME footprints of air sampled at WAO on the 16 <sup>th</sup> November, 7 <sup>th</sup> and 20 <sup>th</sup> December 2010	138
<b>FIGURE 4.21:</b> : 1 week of CO <sub>2</sub> , O <sub>2</sub> and APO data from WAO starting on 23 <sup>rd</sup> July 2011	139
<b>FIGURE 4.22:</b> NAME footprints of air sampled at WAO on the 23 <sup>rd</sup> and 24 <sup>th</sup> July 2011	139
<b>FIGURE 4.23:</b> NAME footprints of air sampled at WAO on the 25 <sup>th</sup> July 2011	140
<b>FIGURE 4.24:</b> NAME footprints of air sampled at WAO on the 26 <sup>th</sup> and 27 <sup>th</sup> July 2011	141
<b>FIGURE 4.25:</b> NAME footprints of air sampled at WAO on the 29 <sup>th</sup> July 2011	142

## LIST OF TABLES

<b>TABLE 1.1:</b> Relative abundances of gases in the earth's atmosphere	20
<b>TABLE 3.1:</b> Long term trends for CO <sub>2</sub> , O <sub>2</sub> and APO at Weybourne Atmospheric Observatory	87
<b>TABLE 3.2:</b> Comparison of long-term trends for CO <sub>2</sub> , O <sub>2</sub> and APO observed at Weybourne Atmospheric Observatory with other European observatories	89
<b>TABLE 3.3:</b> Seasonal amplitudes at 6 month intervals for CO <sub>2</sub> , O <sub>2</sub> and APO at Weybourne Atmospheric Observatory	94
<b>TABLE 3.4:</b> Comparison of seasonal amplitude for CO <sub>2</sub> , O <sub>2</sub> and APO observed at Weybourne Atmospheric Observatory with other European observatories	95
<b>TABLE 3.5:</b> Summary of zero crossing days for CO <sub>2</sub> , O <sub>2</sub> and APO observed at Weybourne Atmospheric Observatory	99
<b>TABLE 4.1:</b> Summary of contribution from 4 different wind quadrants at different times of the year at Weybourne Atmospheric Observatory	122
<b>TABLE 4.2:</b> Seasonal amplitudes at 6 month intervals for CO <sub>2</sub> filtered by wind sector	127
<b>TABLE 4.3:</b> Seasonal amplitudes at 6 month intervals for O <sub>2</sub> filtered by wind sector	127
<b>TABLE 4.4:</b> Seasonal amplitudes at 6 month intervals for APO filtered by wind sector	127
<b>TABLE 4.5:</b> O <sub>2</sub> :CO <sub>2</sub> ratios for 3 pollution events in November and December 2010	137

## **ACKNOWLEDGEMENTS**

First and foremost I need to thank Andrew Manning for his help and supervision throughout my PhD. In a subject area that I was initially unfamiliar with his expert guidance and attention to detail ensured that I got up to speed as quickly as possible and avoided many pitfalls I might otherwise have befallen. Andrew has always made himself available and give time to helping his students and deserves a lot of credit for this. His help while writing this thesis has also been invaluable.

On a day to day basis UEA's technical support has always been helpful and I thank everyone that I've bothered from time to time throughout my PhD. A special mention must go to Andy Macdonald who taught me a lot of the lab skills I've needed, and showed me just how neat intricate plumbing could be. I probably worked most closely with Andy in the lab and enjoyed every second. In the electronics department Dave Blomfield and Nick Griffin provided valuable assistance setting up and maintaining the electronics of the system at Weybourne. Stuart Rix in the workshop was also always happy to help and offer solutions when presented with problems.

Alex Etchells, the department's self-taught software engineer and founder of ENVsoft, deserves special thanks. He not only wrote and rewrote the software to control the Weybourne software, catering for my every whim but also helped out beyond his remit on many occasions; informing my amateur electronic knowledge or setting cylinder pressures when he had to go to Weybourne for other jobs and doing it all with a smile. It has been a pleasure working with him.

I extend my thanks to the CRAM group in general, it started out with just Andrew, Andy and myself but has grown over time and I hope it continues to grow and develop into interesting new areas as time goes on. I must thank Grant Forster for his help at Weybourne, especially in recent months, as well as for his advice and sense of humour. Marica Hewitt has also been extremely helpful and thoughtful; checking everything's ok and taking care of many time consuming tasks when I've been occupied, for this I'm very grateful. Penelope Pickers, the newest member of

the CRAM group has also been a great help over the past month or so. Finally I would like to thank Michael Patecki for the time he spent with me when I was first getting to grips with O<sub>2</sub> measurements at the start of my PhD.

I also need to thank my supervisory committee and apologise for the meetings at short notice and late reports. I thank you for your advice and expertise over the last few years; Andy Watson, Bill Sturges and Corinne Le Quéré. Corinne and Clare Enright I must also thank for the model runs included at the end of chapter 3.

I also thank the Natural Environment Research Council (NERC) for funding my PhD studentship through the South Atlantic project (Grant No. NE/F005733/1).

The NAME dispersion model footprints are a fantastic resource for a station like Weybourne and they have helped no end in my analysis of the data, particularly when looking at short-term events in chapter 4. For these runs, and for explaining how they're generated I thank Zoë Fleming at the university of Leicester.

Last but by no means least I must personally thank those close to me for their support in many and varied ways during my PhD (and in some cases for a lifetime leading up to it). Thank you for your wisdom, patience, understanding and occasional distractions to my Mum, Dad, Zoë, Nomi, Polly, Jenny and the close group of friends I feel incredibly fortunate to have.

## **CHAPTER 1 – INTRODUCTION**

## 1.1 Introduction to chapter

Greenhouse gases contribute to shaping the climate of the Earth. Without the naturally occurring greenhouse gases retaining some of the energy from solar radiation that would otherwise be reflected back into space, the Earth's surface temperature would be about 30°C cooler on average and unsuitable for life. The fact that some of the less abundant gases, making up only a tiny fraction of the Earth's atmosphere, are responsible for this effect was first recognised during the 19th century by Joseph Fourier and confirmed by John Tyndall (Tyndall, 1881) and Knut Ångström (Ångström, 1901). Tyndall is considered a pioneer in the field of spectroscopy as he recognised that the properties of certain molecules lead them to absorb radiant heat, that is, electromagnetic energy in the infrared range of wavelengths (2-70  $\mu\text{m}$ ). It is these molecular properties that lead to the greenhouse effect: short wavelength radiation from the sun enters the Earth's atmosphere, where it is absorbed by energy transitions within molecules and re-emitted as longer wavelength infrared radiation. Certain frequencies of infrared radiation match the resonant frequency of the molecular bonds of some atmospheric species and so this radiation is absorbed, causing individual bonds and atoms to vibrate before the energy is reemitted in all directions. This has the net effect of retaining some infrared radiation close to the surface of the Earth that would otherwise be emitted back into space, thereby increasing surface temperatures. This is shown schematically in Figure 1.1. A further process that retains energy close to the surface of the Earth is caused by the temperature gradient of the atmosphere, in particular the cooling further from the surface of the Earth in the troposphere (the tropospheric temperature lapse rate). In a layer of the troposphere, the warmer molecules closer to the surface of the Earth emit radiation at a greater rate than cooler molecules further from the surface. This leads to the net result that more infrared radiation is re-emitted downwards towards the surface of the Earth than upwards where it may be exchanged back into space.

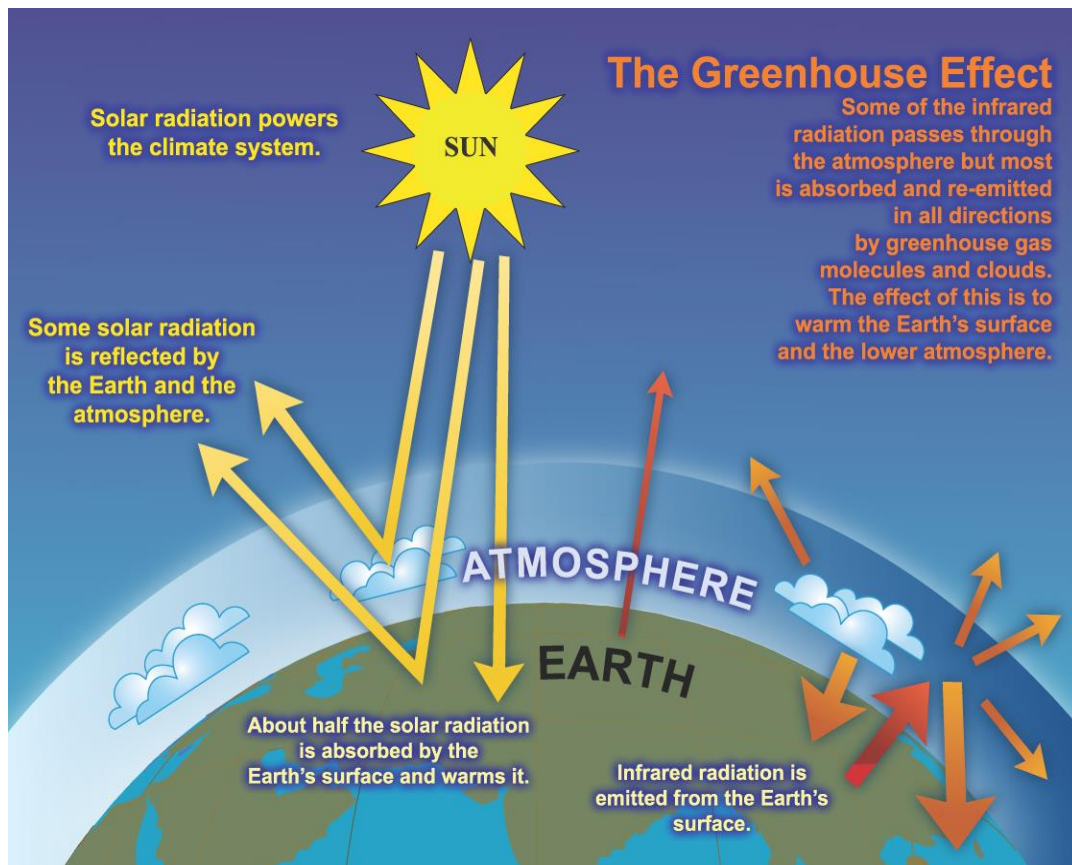


Figure 1.1 Schematic explaining the greenhouse effect.

For a molecule to absorb infrared radiation it must undergo a change in dipole moment (the spatial distribution of charge about the molecule) and so symmetric, simple, diatomic molecules such as nitrogen ( $N_2$ ) and oxygen ( $O_2$ ), the two main constituents of air, are unaffected by infrared radiation. Instead, the molecules primarily responsible for the greenhouse effect are water vapour and carbon dioxide ( $CO_2$ ). Many other trace gas species in the atmosphere such as methane ( $CH_4$ ), nitrous oxide ( $N_2O$ ) and a large number of chlorofluorocarbons (CFCs) and hydrofluorocarbons (HFCs) are also greenhouse gases, but these have a much smaller (though not negligible) contribution to the overall greenhouse effect. Despite the fact that all of these other species exhibit a stronger ability to absorb infrared radiation than  $CO_2$ , their atmospheric concentrations are so low that their influence is minor. Some greenhouse gases are present naturally and, as alluded to above, the natural greenhouse effect is essential for the habitable temperature we experience on Earth. Industrialisation, however, has led to the rapid burning of fossil fuels and an associated increase in the atmospheric concentration of  $CO_2$  that has reinforced the natural greenhouse effect to the point that the Earth's surface is

now warming at an alarming rate (Jones and Moberg, 2003). This effect is not a new discovery; in 1896, while investigating possible causes for glacial-interglacial temperature cycles, Svante Arrhenius calculated that a doubling of atmospheric CO<sub>2</sub> would lead to a 4 °C rise in the Earth's surface temperature (Arrhenius, 1896).

The water vapour content of air is closely linked to temperature and equilibrates rapidly in the event of a change in temperature (Soden et al., 2002). Thus, water vapour is considered a feedback agent, responding to and reinforcing changes in temperature, rather than being a forcing agent, causing the changes. CO<sub>2</sub> is the most important anthropogenic greenhouse gas; human activity continues to play a dominant role in atmospheric CO<sub>2</sub> concentrations and thus it is essential to understand the processes and mechanisms affecting atmospheric CO<sub>2</sub> and the wider carbon cycle as fully as possible in order to better understand the complex climate system we live in and to make more accurate predictions of future climate.

## 1.2 The carbon cycle

### 1.2.1 The global carbon cycle

Figure 1.2 shows an overview of the global carbon cycle, as presented in the Intergovernmental Panel on Climate Change's (IPCC) Fourth Assessment Report on Climate Change (AR4) (IPCC, 2007). The figure summarises the interactions between different reservoirs of carbon on Earth. The major reservoirs can be broadly classified into four categories; the geologic reservoir, the terrestrial reservoir, the oceanic reservoir and the atmospheric reservoir.

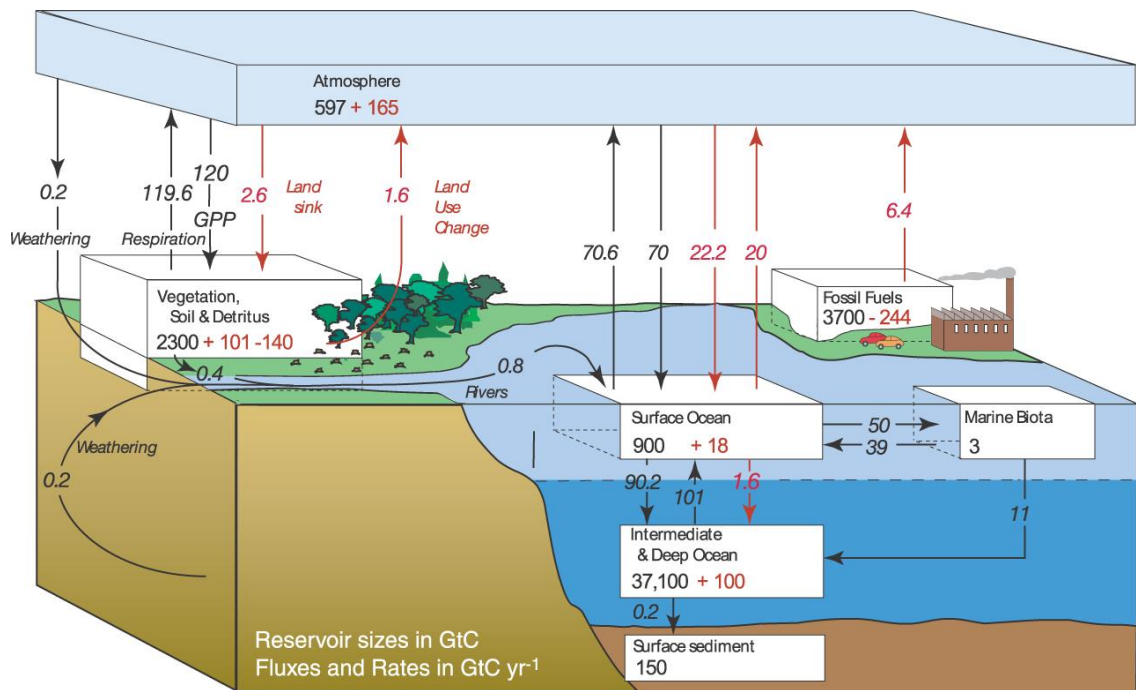


Figure 1.2 Schematic of the global carbon cycle showing the atmosphere, terrestrial biosphere and the oceans, and the fluxes between these major reservoirs. Anthropogenic fluxes are shown in red and natural fluxes in black (IPCC, 2007).

The geologic reservoir contains the vast majority of the carbon found on Earth. Carbon is stored as inorganic compounds in rocks, for example as calcium carbonate ( $\text{CaCO}_3$ ) in limestone and marble, and as organic compounds, for example the long chain alkanes found in fossil fuels. Exchanges between the geologic reservoir and other reservoirs are relatively very slow, occurring on geologic timescales over thousands or millions of years. For example, the natural process of deposition of  $\text{CaCO}_3$  from marine organisms to form sedimentary rocks such as limestone occurs over many hundreds of years, and the heat and pressure required to turn this rock into marble takes centuries more. Subsequently, the weathering and erosion of rock that returns the carbon to the atmospheric and oceanic reservoirs is also an extremely slow process. On time scales of years, decades and a few centuries, therefore, the geologic reservoir can be thought of as essentially a form of permanent carbon storage, with the carbon locked away and playing only a very minor role in the contemporary carbon cycle, with a few notable exceptions such as periodic volcanic eruptions. In total the geologic reservoir contains approximately 80,000,000 Pg C; over 60,000,000 as

sedimentary carbonate rocks and 15,000,000 Pg C in organic form as kerogens (Falkowski et al., 2000).

The terrestrial carbon reservoir includes all the organic and inorganic carbon compounds that are essential to, and make up, the life forms that live on the land. The ability of carbon atoms to form a varied array of bonds with other atoms has led to its central role in the development of life on Earth. It forms the backbone of the molecules that make up the vast majority of all animals and plants. Carbon can be 'fixed' from the atmosphere via the process of photosynthesis, meaning to be incorporated into organic carbon molecules, and can be released back to the atmosphere by the reverse process of respiration whereby organic molecules are broken down. A large amount of carbon is also present in soils, usually as dead and decaying organic matter. Exchanges between the terrestrial and atmospheric reservoirs can occur relatively rapidly and with significant fluxes on short time scales (days to years). Exchange with the geologic reservoir, for example coal formation, and directly with the oceanic reservoir, by erosion and deposition in streams and oceans, are much slower processes and do not occur in great magnitudes over short time scales. Terrestrial organic matter contains in the region of 550 Pg C, while soils contain about 1500 – 2000 Pg C (Houghton, 2007).

The oceanic carbon reservoir can be divided into a surface ocean reservoir of 900 Pg C and a deep ocean reservoir of approximately 37,100 Pg C (Houghton, 2007). A small fraction of oceanic carbon is present as organic compounds (about 3 Pg C) but the vast majority is present as dissolved inorganic carbon (DIC) in seawater. Exchange of carbon on short time scales is mainly via the interface with the atmosphere; sedimentation of inorganic carbon does occur but the process of forming new sedimentary rocks, oil and natural gas is extremely slow.

The atmospheric reservoir of carbon consists primarily of CO<sub>2</sub> gas. At today's global atmospheric concentration of about 390 ppm (parts per million), CO<sub>2</sub> equates to an atmospheric reservoir of 828 Pg C (this is higher than the value of 762 Pg C given in figure 1.2 since 390 ppm CO<sub>2</sub> is a more recent, higher atmospheric concentration, resulting from the ongoing burning of fossil fuels). Contributions from other carbon containing gases such as methane (1.8 ppm),

carbon monoxide (0.1 ppm) and other trace gases containing carbon is so small as to be negligible in terms of calculating a global carbon budget. On short time scales, the atmospheric reservoir is the key interface as it can exchange carbon relatively quickly in significant quantities with both the terrestrial and oceanic reservoirs.

Before the industrial revolution the global carbon cycle had been in equilibrium, and atmospheric concentrations of CO<sub>2</sub> had been stable in the range of 260 – 280 ppm for about 10,000 years (Monnin et al., 2001). The system was still dynamic, with carbon continually being exchanged between the atmosphere and the terrestrial and oceanic reservoirs. Photosynthesis converts CO<sub>2</sub> to terrestrial plant biomass or to phytoplankton in the oceans. Terrestrial plant, animal and soil respiration and decomposition returns CO<sub>2</sub> to the atmosphere, as does biomass burning. At the surface of the ocean CO<sub>2</sub> is constantly exchanged, either moving from the gaseous phase in the atmosphere to become dissolved, aqueous CO<sub>2</sub> in the ocean or vice-versa, shown in equation 1.1. CO<sub>2</sub>, in common with most gases, has a low solubility coefficient and is only sparingly soluble in seawater. As such, one would expect the vast majority of the total carbon from the atmosphere and oceans to be stored in the atmosphere, however, CO<sub>2</sub> undergoes a series of geochemical reactions in seawater that converts it to much more soluble inorganic compounds. First, CO<sub>2</sub> combines with water to form carbonic acid (equation 1.2), then the carbonic acid dissociates to form a bicarbonate anion and a proton (equation 1.3), and then in turn the bicarbonate anion may dissociate to form a carbonate ion and a further proton (equation 1.4).



Each reaction has its own equilibrium constant and the position of the equilibrium is dependent on pressure, temperature and the presence of other ions. In the ocean at the present-day pH value (approximately 8.2), there is a strong tendency towards the bicarbonate ion with a much smaller contribution from the carbonate ion and less still from dissolved CO<sub>2</sub>; the approximate proportions in the present-

day ocean are 90%, 9% and 1% respectively for bicarbonate, carbonate and dissolved CO<sub>2</sub>. This conversion of dissolved CO<sub>2</sub> to much more soluble ions is what drives the ocean's capacity to absorb large amounts of CO<sub>2</sub> from the atmosphere and is the reason why the oceanic reservoir contains in the region of 50 times as much carbon as the atmospheric reservoir (Sarmiento and Gruber, 2002).

The interaction between the oceanic and atmospheric reservoirs occurs at the interface between them, the surface of the ocean, however, the vast majority of carbon in the ocean is found in deeper waters. The mechanisms that remove carbon from the surface ocean and deposit it in deeper waters are referred to as the solubility pump and the biological pump. The biological pump refers to the sinking of dead organic matter that contains carbon, often small CaCO<sub>3</sub>-containing organisms. These organisms sink through the water column whilst being decomposed by bacteria. This decomposition means that much of their carbon content is recirculated throughout the ocean, with only a small fraction reaching very deep waters. The solubility pump refers to the downwelling of more dense, colder water from the surface at certain areas of the world, particularly in the higher latitudes of the world's oceans. Colder water is more soluble to CO<sub>2</sub> (and other gases) and so becomes enriched in DIC while at the surface, then transports the carbon down to the depths as it descends. Once carbon reaches the deep ocean it can remain there for hundreds to thousands of years.

### 1.2.2 Anthropogenic influence on the carbon cycle and the greenhouse effect

The carbon cycle was in a state of equilibrium for about 10,000 years prior to the industrial revolution that began around 1750 (Monnin et al., 2001). At this time, humans began to burn increasing quantities of one of the long-term stores of carbon, fossil fuels in the form of coal and peat. Increasing populations and industrialisation also led to increased rates of deforestation and land use change around this time, reducing the natural terrestrial carbon sink. This led to an increasing net flux of CO<sub>2</sub> into the atmosphere that has shifted the equilibrium of the carbon cycle so that the global average atmospheric CO<sub>2</sub> concentration has risen from the preindustrial value of ~280 ppm to 389.6 ppm by 2011 (Peters et

al., 2012). This documented rise in atmospheric CO<sub>2</sub> does not demonstrate the complete picture of how much additional carbon has been put into the atmosphere by human activities, however, since, on average, 43% of fossil fuel CO<sub>2</sub> emissions have been absorbed by the terrestrial and oceanic reservoirs. When CO<sub>2</sub> emissions from land-use change are included in the calculation, the fraction absorbed by the terrestrial and oceanic reservoirs is, on average, about 57% (Le Quéré et al., 2009), although this latter value is subject to greater uncertainty due to greater uncertainty in land-use change emissions.

The addition of extra CO<sub>2</sub> into the atmosphere by humans has effectively short-circuited the natural carbon cycle by taking the long-term store of fossil carbon and rapidly releasing it to the atmosphere, forcing the equilibrium of the system so that the two main natural sinks have increased in magnitude and offset the atmospheric increase (Sarmiento and Gruber, 2002). In other words, under a higher CO<sub>2</sub> environment, the terrestrial biosphere grows more rapidly and the ocean carbon sink also responds by increasing the amount of CO<sub>2</sub> it absorbs from the atmosphere. It is very unclear, however, if the natural sinks can keep pace with the exponentially increasing emissions, with some recent studies suggesting that the natural sinks are starting to become less efficient (Le Quéré et al., 2009; Watson et al., 2009; Raupach et al., 2008). Interpretation of available data remains inconclusive, however, with other studies suggesting that, so far, the natural sinks are keeping pace with emissions (Knorr, 2009; Sarmiento et al., 2010; Gloor et al., 2010).

The additional CO<sub>2</sub> that is accumulating in the atmosphere has been proven to be due to human activities, with a predominant fossil fuel source, based on a number of pieces of evidence. One of the most conclusive arguments relates to the fact that fossil fuels by their nature are depleted in <sup>14</sup>C. <sup>14</sup>C is a radioactive isotope of carbon that decays over time (half-life about 5,700 years), and because fossil fuels are extremely old, they contain almost no <sup>14</sup>C. Nuclear bomb testing in the 1950s and 1960s dramatically increased the background levels of <sup>14</sup>C found in the atmosphere as <sup>14</sup>CO<sub>2</sub>. Since the ban on atmospheric testing of nuclear bombs, it has been observed that the levels of <sup>14</sup>CO<sub>2</sub> in the atmosphere are decreasing, and at a rate that can not be explained by either radioactive decay nor dissolution in the

oceans. This decrease is proof that the atmosphere is becoming diluted in  $^{14}\text{CO}_2$  due to the burning of fossil fuels that do not contain  $^{14}\text{C}$  (Keeling, 1960). This dilution of  $^{14}\text{CO}_2$  in the atmosphere by fossil fuel burning is referred to as the Seuss effect.

The increasing concentration of  $\text{CO}_2$  in the atmosphere enhances the natural greenhouse effect. A rise from 280 ppm  $\text{CO}_2$  to 390 ppm  $\text{CO}_2$  means that there are almost 40% more  $\text{CO}_2$  molecules present in the atmosphere than in 1750. The more  $\text{CO}_2$  and other greenhouse gases present in the atmosphere, the more the planet as a whole will warm.

### 1.3 Oxygen

Oxygen ( $\text{O}_2$ ) is the second most abundant gas in the Earth's atmosphere, as shown in table 1.1, which also shows the relative abundance of the other major constituents of the atmosphere.

Gas	Abundance (%)
Nitrogen ( $\text{N}_2$ )	78.084
Oxygen ( $\text{O}_2$ )	20.939
Argon (Ar)	0.934
Carbon dioxide ( $\text{CO}_2$ )	0.0390
Neon (Ne)	0.0018
Helium (He)	0.00052
Methane ( $\text{CH}_4$ )	0.00018
Krypton (Kr)	0.00011
Hydrogen ( $\text{H}_2$ )	0.000055
Nitrous oxide ( $\text{N}_2\text{O}$ )	0.000032
Carbon monoxide (CO)	0.00001

Table 1.1. Relative abundances of gases in the Earth's atmosphere. Abundances shown are in dry air, water vapour accounts for approximately 0.4% of the Earth's atmosphere and most is near to the surface where it accounts for 1-4% of the make-up of the atmosphere.

Oxygen is not a greenhouse gas; the oxygen molecule is diatomic and symmetrical and so is not optically active in the infrared range of wavelengths emitted by the

Earth. It was realised some time ago, however, that the interplay between CO<sub>2</sub> and O<sub>2</sub> in key processes such as photosynthesis, respiration and fossil fuel burning, together with the absence of an inter-dependency in other processes such as ocean carbon chemistry, meant that concurrent measurements of atmospheric CO<sub>2</sub> and O<sub>2</sub> could be quite informative about the wider carbon cycle (Carpenter, 1937; Keeling, 1988; Machta, 1980). Figure 1.3 illustrates the anti-correlated trend in concentrations of CO<sub>2</sub> and O<sub>2</sub> by showing the concentration records for both species from Mauna Loa in Hawaii and from measurements at the South Pole.

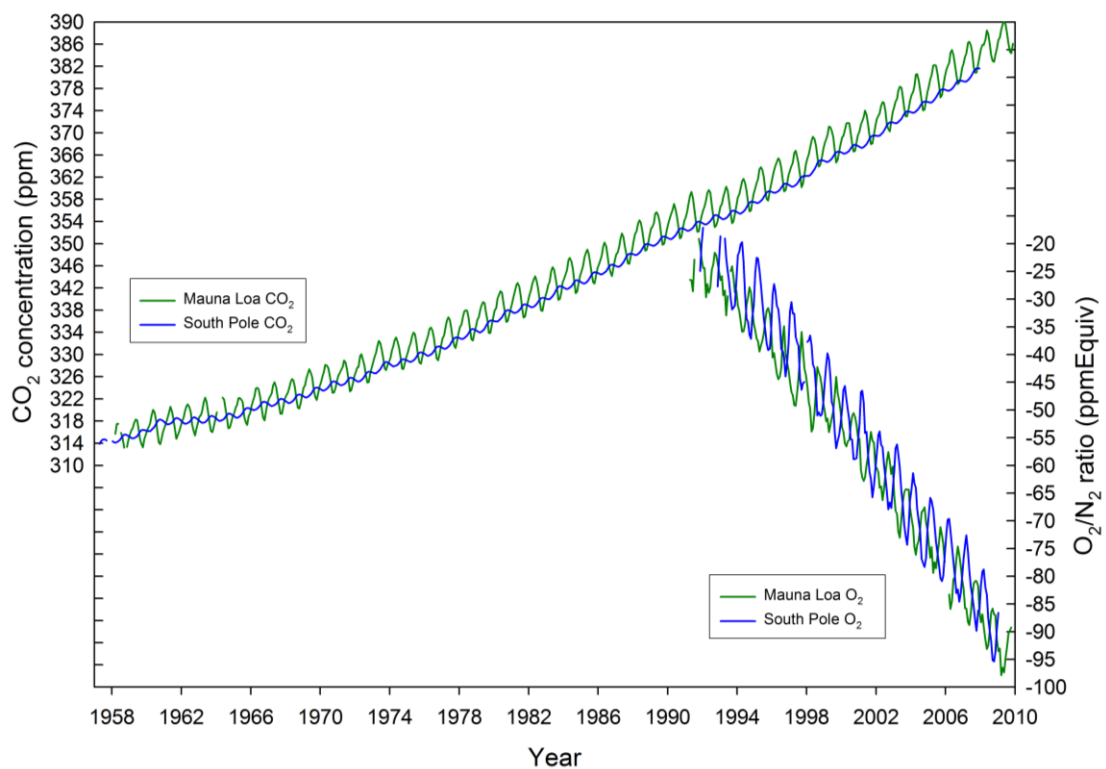


Figure 1.3. CO<sub>2</sub> concentrations and O<sub>2</sub>/N<sub>2</sub> ratios measured at Mauna Loa (green) and the South Pole (blue). This plot shows that as CO<sub>2</sub> concentrations are observed to be rising over time, O<sub>2</sub> concentrations are observed to be falling at a slightly greater rate since there is not the natural buffering effect of chemistry within the oceans for O<sub>2</sub>. This plot also shows the anti-correlated nature of the seasonal cycles in CO<sub>2</sub> and O<sub>2</sub>.

### 1.3.1 The role of oxygen in the global carbon cycle

The key use of oxygen measurements with respect to the carbon cycle has been to partition and quantify the global land and ocean carbon sinks in the overall carbon budget (Keeling and Shertz, 1992; Keeling and Manning, 2012). Other methods to

partition carbon sinks do exist but they rely either on models (Sarmiento et al., 1995; Heimann and Maier-Reimer, 1996) or on direct measurements of carbon containing species (e.g.  $^{13}\text{C}/^{12}\text{C}$  ratio measurements or measurements of  $\text{pCO}_2$  and DIC in the surface ocean (Tans et al., 1990; Sarmiento et al., 1995)). The atmospheric oxygen carbon sink partitioning method is the only direct method that is independent of measurements of carbon containing compounds and avoids some of the large uncertainties associated with these other methods. The atmospheric oxygen method has become a powerful tool for constraining the global land and ocean carbon sinks and, for example, has been used in the past two IPCC Assessment Reports (Houghton et al., 2001; Solomon et al., 2007).

The global carbon cycle schematic shown in Figure 1.2 can be simplified to an overall global budget of  $\text{CO}_2$  as shown in equation 1.5 and an analogous budget for  $\text{O}_2$  as shown in equation 1.6.

$$\Delta\text{CO}_2 = F - O - L \quad (1.5)$$

$$\Delta\text{O}_2 = -\alpha_F F + \alpha_L L + Z \quad (1.6)$$

In these equations,  $\Delta\text{CO}_2$  and  $\Delta\text{O}_2$  are the global atmospheric changes in  $\text{CO}_2$  and  $\text{O}_2$  respectively;  $F$  is the anthropogenic carbon source from fossil fuel burning and cement production;  $O$  represents the net oceanic carbon sink;  $L$  is the net land biotic carbon sink incorporating uptake by the land biosphere, land use change effects and biomass burning, and  $Z$  is the net effect of  $\text{O}_2$  atmosphere-ocean exchange including changes in  $\text{O}_2$  solubility induced by temperature changes, biological pump efficiency and oceanic circulation patterns. All of these quantities are typically expressed in units of moles per annum.  $\alpha_F$  and  $\alpha_L$  represent the global average  $\text{O}_2/\text{CO}_2$  molar exchange ratios for fossil fuel combustion and land biotic processes (photosynthesis and respiration), respectively, where the ratios are expressed as moles of  $\text{O}_2$  consumed per mole of  $\text{CO}_2$  produced (Manning and Keeling, 2006).

Global inventories of fossil fuel use and cement production can be used to obtain values for  $F$ .  $Z$  can be estimated from ocean heat flux data and based on the physical property of decreasing  $\text{O}_2$  solubility as temperature rises, as well as ocean

biogeochemical model results (Bopp et al., 2002; Plattner et al., 2002) or observations of the dependence of dissolved  $O_2$  and phosphate concentrations on temperature (Keeling and García, 2002).  $\alpha_F$  values for the different types of fossil fuels are well established; 1.17 for coal, 1.44 for oil and liquid fossil fuels and 1.95 for natural gas (Keeling, 1988). Manning and Keeling (2006) calculated a global average value in the 1990s for  $\alpha_F$  of  $1.39 \pm 0.04$ , using fossil fuel emissions data from Marland (2008). The  $O_2/CO_2$  land biotic exchange ratio ( $\alpha_L$ ) is poorly constrained. A widely used global average value of  $1.10 \pm 0.05$  was defined based on a limited dataset from laboratory studies (Severinghaus, 1995). This value has been highlighted as possibly an overestimate by two recent studies (e.g. Ciais et al., 2007; Randerson et al., 2006), although Keeling and Manning (2012) contend that 1.10 is indeed the most appropriate value to use when estimating land and ocean carbon sinks from atmospheric  $O_2$  and  $CO_2$  data.  $\alpha_L$  is unlikely to be constant and may vary both temporally and spatially. Any disruption to the key processes associated with the land biosphere may change the stoichiometric coefficients for  $O_2$  and  $CO_2$  in photosynthesis and respiration, for example sudden land use changes, increased soil decomposition as global temperatures increase or increased growth due to a  $CO_2$  fertilisation effect (Keeling et al., 1996; Stephens et al., 2007b). Further work is required to better understand the terrestrial  $O_2/CO_2$  molar exchange ratio and to reduce the associated uncertainties, however, the global average value can be used to calculate the magnitude of the land biotic sink,  $L$ , in equation 1.6. Once a value for  $L$  is obtained this can be substituted into equation 1.5 in order to determine the magnitude of the oceanic sink,  $O$ . It is also worth noting that a change in the value of  $\alpha_F$  has a far larger effect on the calculated values of the land and ocean sinks than a change in the  $\alpha_L$  value. This can be seen from the vector diagram in figure 1.4.

This approach to balancing the global carbon budget can be shown in vector graphics form, as illustrated in figure 1.4, but first it is worth considering how atmospheric oxygen measurements are made and reported before defining an atmospheric tracer that is very useful when attempting to distinguish between terrestrial and oceanic processes that influence atmospheric oxygen.

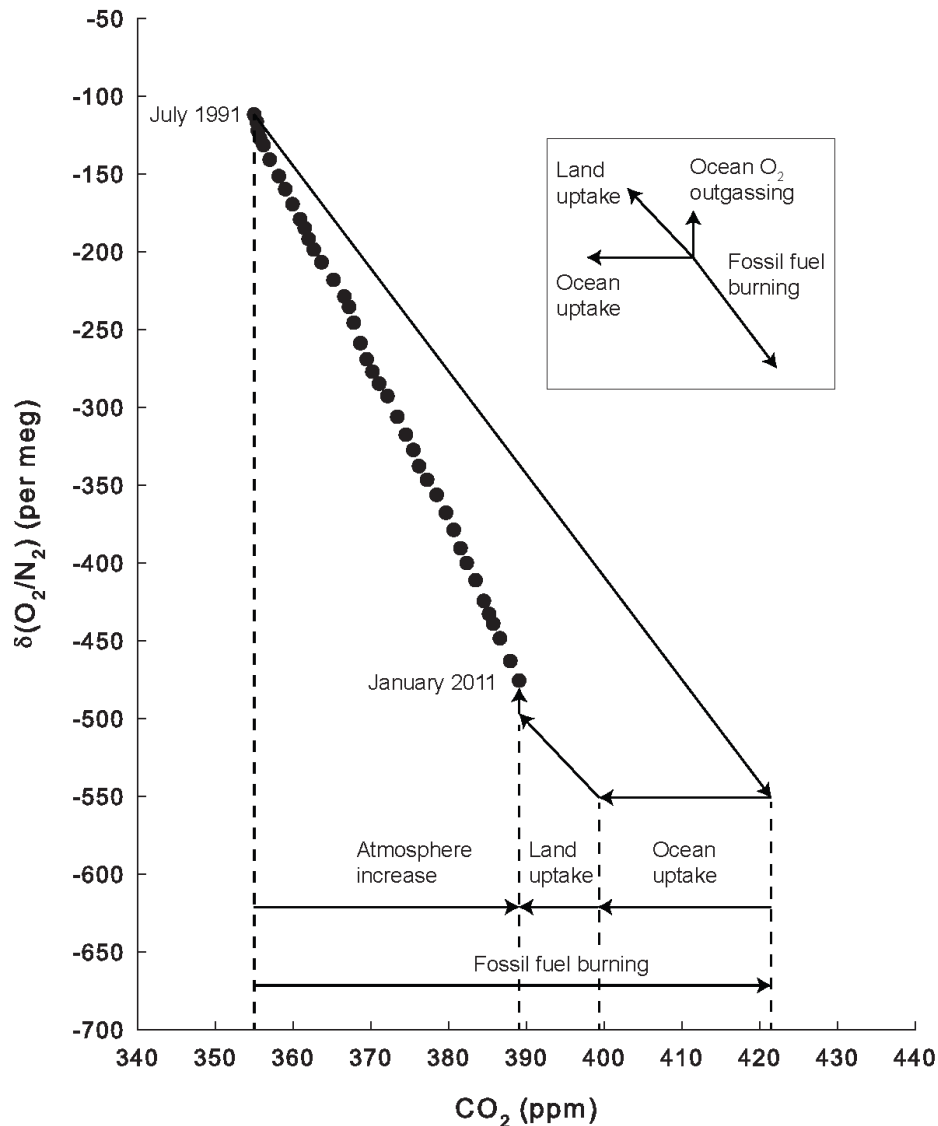


Figure 1.4.  $\delta(\text{O}_2/\text{N}_2)$  versus  $\text{CO}_2$  (both globally and annually averaged) over the period July 1991 through January 2011, computed every six months (solid circles). If the only influence on  $\delta(\text{O}_2/\text{N}_2)$  and  $\text{CO}_2$  over this period had been fossil-fuel burning, the atmospheric composition would have changed according to the long downward arrow. The remaining arrows indicate the unique combination of land and ocean uptake required to account for the observations, where a small additional  $\text{O}_2$  source from oceanic  $\text{O}_2$  outgassing is also specified (depicted by small vertical arrow). Global averages are based on data from Alert, Canada (82.5°N), La Jolla, USA (32.9°N) and Cape Grim, Australia (40.7°S) stations. Land uptake is assumed to occur with a ratio of 1.1 moles  $\text{O}_2$  produced per mole  $\text{CO}_2$  consumed. Figure reproduced with permission from Keeling and Manning (2012).

### 1.3.2 Oxygen measurements

The absolute changes in the concentration of  $\text{O}_2$  in the atmosphere are of the same order of magnitude as those observed for  $\text{CO}_2$ ; of the order of 1-5 ppm yr<sup>-1</sup> annual

changes, a few ppm in meridional and zonal gradients, and up to ~30 ppm in seasonal cycle amplitudes. These changes for O<sub>2</sub>, however, must be detected against a much higher background concentration of 209,392 ppm O<sub>2</sub> (Tohjima et al., 2005a) versus 389.6 ppm CO<sub>2</sub> (Peters et al., 2012). The challenge to meet this sensitivity requirement with a robust analytical technique meant that routine atmospheric O<sub>2</sub> measurements could only be initiated in the early 1990s after development of an interferometric technique applied to O<sub>2</sub> measurements (Keeling, 1988).

Since the development of the interferometric method, a number of other techniques have been developed for measuring atmospheric O<sub>2</sub>. The expansion to different techniques has helped to improve the overall precision of O<sub>2</sub> measurements as well as meeting certain challenges; for example, measurements can now be made continuously (Manning et al., 1999), rather than from discrete flask samples, and direct measurements can be made at field sites and in field campaigns in some very demanding environments such as on board aircraft (Wofsy, 2011) or shipboard platforms (Thompson et al., 2007; Stephens et al., 2003). The range of analytical techniques now available to measure atmospheric O<sub>2</sub> include mass spectrometry (Bender et al., 1994), paramagnetic analysis (Manning et al., 1999), vacuum ultra-violet absorption (Stephens et al., 2003), gas chromatography (Tohjima, 2000), and fuel cell technology (Stephens et al., 2007a).

Routine O<sub>2</sub> measurements were started by Professor Ralph Keeling at the Scripps Institution of Oceanography (SIO), currently with a network of about 10 stations collecting flask samples for O<sub>2</sub> analysis at the SIO laboratory (Keeling and Manning, 2012). Another observational network was run for many years by Professor Michael Bender, first at the University of Rhode Island and then at Princeton University (Bender et al., 2005), but this network has recently been disbanded, with some of the stations being incorporated into existing and new networks run by SIO and UEA. Other institutions that make routine O<sub>2</sub> measurements include: Max Planck Institute for Biogeochemistry (MPI-BGC, Germany), University of Bern (Switzerland), University of Groningen (The Netherlands), Laboratoire des Sciences du Climat et de l'Environnement (LSCE, France), National Institute for Environmental Studies (NIES, Japan), Tohoku University (Japan), National Center

for Atmospheric Research (NCAR, USA) and the National Institute of Water and Atmospheric Research (NIWA, New Zealand).

Changes in atmospheric O<sub>2</sub> concentration are usually reported as changes in the ratio of O<sub>2</sub> to N<sub>2</sub> in dry air. Since atmospheric N<sub>2</sub> concentrations are much less variable than O<sub>2</sub>, changes in the O<sub>2</sub>/N<sub>2</sub> ratio mainly reflect changes in O<sub>2</sub> concentration. The advantage of reporting the O<sub>2</sub>/N<sub>2</sub> ratio rather than O<sub>2</sub> concentration is that it is insensitive to changes in other atmospheric gases, for example the seasonal changes or long-term rise in CO<sub>2</sub>. The early pioneers of O<sub>2</sub> measurements laid the groundwork for this methodology and reported the O<sub>2</sub>/N<sub>2</sub> ratio as a relative deviation from a known reference standard. Since changes are very small, this value is multiplied by 10<sup>6</sup> and the results are expressed in ‘per meg’ units (see equation 1.7) (Keeling and Shertz, 1992). This terminology is an adaption of that typically used when measuring isotopic abundances, where isotope ratios are also related to a reference ratio, multiplied by 10<sup>3</sup> and reported in per mil (‰) units.

$$\delta \left( O_2/N_2 \right) = \left( \frac{(O_2/N_2)_{sample}}{(O_2/N_2)_{reference}} - 1 \right) \times 10^6 \quad (1.7)$$

Most analytical techniques used for measuring O<sub>2</sub> are sensitive to the O<sub>2</sub> mole fraction (the notable exception being mass spectrometry that measures the O<sub>2</sub>/N<sub>2</sub> ratio directly), for which a correction for CO<sub>2</sub> dilution must be applied. This correction accounts for any change in the mole fraction of CO<sub>2</sub>, which must be measured concurrently, and is shown in equation 1.8.

$$\delta \left( O_2/N_2 \right) = \frac{\delta X_{O_2} + (\Delta CO_2 \times S_{O_2})}{(1 - S_{O_2}) \times S_{O_2}} \quad (1.8)$$

Where S<sub>O<sub>2</sub></sub> is the standard mole fraction of O<sub>2</sub> in air (taken as 0.209392 (Tohjima et al., 2005a)), δX<sub>O<sub>2</sub></sub> is the measured change in O<sub>2</sub> mole fraction and ΔCO<sub>2</sub> the measured change in CO<sub>2</sub> mole fraction. This dilution correction could be expanded to include other atmospheric species that may dilute O<sub>2</sub> in air, but in practice variations in other species are almost always small enough to be negligible with regard to their influence on O<sub>2</sub>. One notable exception is when atmospheric Ar

changes are significant, as sometimes happens when preparing O<sub>2</sub>/N<sub>2</sub> calibration standards with high pressure compressor systems. From this equation it can be calculated that a 1 μmol mol<sup>-1</sup> change in O<sub>2</sub> mole fraction, while keeping CO<sub>2</sub> constant, equates to a 6.04 per meg change in O<sub>2</sub>/N<sub>2</sub> ratio. If, instead, there is a 1 μmol mol<sup>-1</sup> change in CO<sub>2</sub> mole fraction at the same time as there is a 1 μmol mol<sup>-1</sup> change in O<sub>2</sub> in the opposite direction (e.g. an exchange), then this equates to a 4.77 per meg change in O<sub>2</sub>/N<sub>2</sub> ratio.

### 1.3.3 Atmospheric Potential Oxygen (APO)

Atmospheric Potential Oxygen (APO), defined in equation 1.9, is the weighted sum of atmospheric O<sub>2</sub> and CO<sub>2</sub>, with the contribution from CO<sub>2</sub> weighted by the terrestrial molar exchange ratio, α<sub>L</sub>.

$$APO = O_2 + \alpha_L CO_2 \quad (1.9)$$

This definition results in the APO tracer being mostly insensitive to O<sub>2</sub> and CO<sub>2</sub> exchanges with the terrestrial biosphere where the two gases are strongly coupled, and so variations in APO are caused only by processes unrelated to terrestrial biosphere exchanges such as marine processes and combustion. APO was first defined by Stephens et al. (1998) as:

$$\delta APO = \delta \left( O_2 / N_2 \right) + 1.1 \times \frac{(CO_2 - 350)}{S_{O_2}} \quad (1.10)$$

δ(O<sub>2</sub>/N<sub>2</sub>) is as defined above in per meg, CO<sub>2</sub> is the measured carbon dioxide mole fraction (sometimes written as X<sub>CO<sub>2</sub></sub>) in ppm and 1.1 is the value typically used for α<sub>L</sub>. S<sub>O<sub>2</sub></sub> (sometimes written as X<sub>O<sub>2</sub></sub>) is the standard mole fraction of O<sub>2</sub> in air, generally taken as 0.209392, and 350 is an arbitrary reference. δAPO is reported in per meg units. While insensitive to terrestrial photosynthesis and respiration, APO is sensitive to air – sea exchanges of O<sub>2</sub>, CO<sub>2</sub> and N<sub>2</sub>. APO will also be affected by fossil fuel burning, since the oxidative ratio of most fossil fuels differs from the value of 1.1 used to account for terrestrial photosynthesis and respiration.

Combining the APO equation (1.9) with the equations for the CO<sub>2</sub> (1.5) and O<sub>2</sub> (1.6) global budgets to produce an APO global budget (equation 1.11) allows a different route to calculating the magnitude of the ocean and land carbon sinks (Manning and Keeling, 2006):

$$\Delta APO = (-\alpha_F + \alpha_L)F - \alpha_L O + Z \quad (1.11)$$

Here  $\Delta APO$  is the globally averaged change in APO in moles per year. Equations 1.10 and 1.11 both express a change in APO and so they can be combined. Subsequently solving for the ocean carbon sink,  $O$ , allows it to be calculated directly from measurements of APO in per meg units according to:

$$O = \left[ (-\Delta(\delta APO) \times M_{air} \times S_{O_2}) + (-\alpha_F + \alpha_L)F + \left( \frac{Z_{eff}}{M_C} \right) \right] \frac{1}{\alpha_L} \quad (1.12)$$

Where  $M_{air}$  is the mass of air in the atmosphere and  $Z_{eff}$  represents the net effect of oceanic outgassing on the oceanic and land biotic carbon sinks, in units of Pg C yr<sup>-1</sup>.  $Z_{eff}$  also takes into account the offset caused by N<sub>2</sub> outgassing.  $Z_{eff}$  is expressed by:

$$Z_{eff} = \left( Z - \Delta N_2 \frac{X_{O_2}}{X_{N_2}} \right) \times M_C \quad (1.13)$$

$M_C$  is the molar mass of carbon (12.01 g mol<sup>-1</sup>). This means that the oceanic carbon sink will increase by the amount  $Z_{eff}$  and the land biotic carbon sink will decrease by the same amount. Once  $O$  has been determined from equation 1.12, the land biotic sink can be calculated from measurements of CO<sub>2</sub> mole fraction. To do this equation 1.5, expressing the budget in CO<sub>2</sub>, can be rearranged and solved for  $L$ . The change in total CO<sub>2</sub> ( $\Delta CO_2$ ) can be calculated from multiplying the observed change in CO<sub>2</sub> mole fraction by the mass of air in the atmosphere. This is shown below in equation 1.14:

$$L = F - O - \Delta X_{CO_2} \times M_{air} \quad (1.14)$$

The key advantage of using APO to compute the land biotic carbon sink is that it reduces uncertainty. Short-term variations in APO are much less than in O<sub>2</sub>/N<sub>2</sub> ratios and this approach also allows the global atmospheric CO<sub>2</sub> datasets to be used to derive the change in CO<sub>2</sub> mole fraction ( $\Delta X_{CO_2}$ ). Atmospheric CO<sub>2</sub>

measurement sites are much more numerous than those measuring both O<sub>2</sub>/N<sub>2</sub> and CO<sub>2</sub>.

APO exhibits a seasonal cycle (Langenfelds et al., 2002; Bender et al., 2005; Sturm et al., 2005; Tohjima et al., 2005b; Battle et al., 2006; Kozlova et al., 2008) and generally the amplitude of this cycle increases at higher latitudes. The APO seasonal cycle is mainly driven by ocean ventilation changes, marine productivity cycling and the changing solubility of O<sub>2</sub> in the oceans as temperature changes, and it has been shown that these processes mostly occur at latitudes greater than 30° (Keeling et al., 1998). The seasonal cycle is therefore more evident at stations that sample marine air as opposed to those sampling mainly continental air or air from above the boundary layer.

Analyses of the seasonal cycle in APO can be used to improve estimates of ocean biological production and ocean ventilation rates. This involves separating out the contribution to the seasonal cycle from temperature related solubility-driven air-sea exchange and that from surface water production and ventilation of O<sub>2</sub>. This was first attempted by Keeling and Shertz (1992) and involves accounting for temperature driven solubility changes to APO by using knowledge of air-sea heat fluxes. APO observations have also been used to test ocean biogeochemical models. Observed APO variations were compared to those calculated using an atmospheric transport model that transferred fluxes from ocean biogeochemical models to the atmosphere (Stephens et al., 1998; Balkanski et al., 1999). When studying how temperature-driven solubility changes affect the seasonal cycle in APO, observations can be used to test parameterisations of the air-sea gas exchange velocity (Keeling et al., 1996).

On longer, interannual time scales, APO is decreasing globally, primarily driven by the decrease in atmospheric O<sub>2</sub> caused by fossil fuel burning. The magnitude of the APO decrease is not consistent year on year as some interannual variability has been shown (Hamme and Keeling, 2008). Hamme and Keeling (2008) found that interannual variability in APO did not correlate well with heat driven air-sea fluxes or with ocean biological production, and the magnitude of the APO variability could not be explained by variations in either atmospheric circulation or fossil fuel

burning. Variations in subsurface ocean ventilation were concluded to be the main cause of interannual APO variability. By extending this conclusion, measurements of interannual APO variability could be used to test ocean biogeochemical models over longer time periods than is possible using the seasonal cycle of APO alone.

#### 1.4 Future directions for carbon cycle related research

The not inconsiderable challenge of measuring sub-ppm level changes in atmospheric CO<sub>2</sub> concentrations in a repeatable and compatible manner has been proven to be achievable in a number of different ways since Charles Keeling first began the Mauna Loa atmospheric CO<sub>2</sub> record in 1958 (Keeling, 1960). Presently, there is a wide network of CO<sub>2</sub> measurement stations throughout the world and much is known about background CO<sub>2</sub> levels and geographic and temporal variations in the seasonal cycle. The challenge to measure similar sub-ppm changes in atmospheric O<sub>2</sub> against a relatively large background concentration has also been proven possible, utilising a variety of different measurement techniques since Ralph Keeling first published such measurements in 1988 (Keeling, 1988). The network of O<sub>2</sub> sampling stations around the globe is not as numerous as for CO<sub>2</sub> but has slowly grown to give global coverage (Keeling and Manning, 2012).

One major challenge going forward is to ensure that as O<sub>2</sub> measurements proliferate, the quality of measurements is retained and they are tied to a central calibration scale so that comparisons between stations are meaningful. The effort to achieve this is on-going and must be maintained into the future.

The scientific use of carbon cycle related measurements is always increasing and novel applications are being conceived. The political and economic importance of these measurements is also growing. An increasing focus is now placed on independent verification of anthropogenic greenhouse gas emission estimates as countries and regions pledge to reduce emissions. This necessitates a larger network of regional stations collecting measurements at high frequencies. In-situ measurements are needed and analysers are being developed to become more robust, and more portable, but to retain the essential accuracy and precision required to measure sub-ppm changes in concentration. Computer models that are

increasingly relied upon to predict the repercussions of the anthropogenic alterations to the carbon cycle must be tested against real world data. Conversely, time series of data can be used to fine tune and improve how models represent the complex climate on Earth, particularly with relation to quantifying the many feedbacks involved in the carbon cycle.

## 1.5 Structure of this thesis

Following from this first introductory chapter, chapter 2 presents the O<sub>2</sub> and CO<sub>2</sub> data collection methods used at Weybourne Atmospheric Observatory (WAO). This Ph.D. has in large part been a practical one, in that a substantial amount of time and work has gone into the establishment of a very high quality data record at WAO, in addition to the regular and frequent maintenance required to collect in situ continuous time series of atmospheric concentrations. An additional relevant point is how much more technically challenging atmospheric O<sub>2</sub> measurement is compared to collecting measurements of most other atmospheric species, as perhaps evidenced by the fact that only ten laboratories world-wide are able to make such measurements.

Chapter 3 presents the full data record from WAO covering the period from October 2007 to April 2012. The data are presented both as 2-minute averages as they are collected in real-time, and as averages over longer periods of time. The details and results of the curve fitting program, 'Hpspline' are explained and shown. The long-term trends in CO<sub>2</sub>, O<sub>2</sub> and APO for the data record are calculated and an attempt is made to look at interannual variability within the constraints of having just four and a half years of data. The seasonal cycles of CO<sub>2</sub>, O<sub>2</sub> and APO recorded at WAO are explored with comparison to other published results at similar latitudes. How the seasonal amplitudes vary between 2009 and 2012 are also investigated. Finally the observations from WAO for the APO seasonal cycle are compared to those generated by an Ocean General Circulation Model coupled to a marine biogeochemistry model for the surrounding area.

Chapter 4 studies in more detail the WAO records for CO<sub>2</sub>, O<sub>2</sub> and APO and shorter timescale events. The diurnal cycle in CO<sub>2</sub> and O<sub>2</sub> are examined, including how

these vary throughout the year. Consideration is then given to the different types of air masses that are sampled at WAO. Firstly, meteorological data collected at WAO are used to generate wind and concentration roses for the entire data record and for the individual seasons throughout the year. The data are then filtered based on the wind direction recorded at the time of measurement to examine if any differences can be noted in the seasonal cycles for air collected from different wind sectors. Finally, a number of individual events are isolated from the records and examined in more detail. O<sub>2</sub>:CO<sub>2</sub> ratios are used to characterise polluted air events and the so-called 'footprints' generated by a particle dispersion model are used to examine the influence of different geographical regions on the air sampled at WAO.

Finally a concluding chapter draws together the work carried out so far measuring CO<sub>2</sub> and O<sub>2</sub> at WAO and discusses in brief some options for future research that may be undertaken as the data records continue to lengthen.

## 1.6 References

Ångström, K.: Ueber die Abhängigkeit der Absorption der Gase, besonders der Kohlensäure, von der Dichte, *Annalen der Physik*, 311, 163-173, 10.1002/andp.19013110913, 1901.

Arrhenius, S.: On the influence of carbonic acid in the air upon the temperature of the ground, *Philosophical Magazine*, 41, 237-276, 1896.

Balkanski, Y., Monfray, P., Battle, M., and Heimann, M.: Ocean primary production derived from satellite data: An evaluation with atmospheric oxygen measurements, *Global Biogeochemical Cycles*, 13, 257-271, 1999.

Battle, M., Mikaloff Fletcher, S., Bender, M. L., Keeling, R. F., Manning, A. C., Gruber, N., Tans, P. P., Hendricks, M. B., Ho, D. T., Simonds, C., Mika, R., and Paplawsky, B.: Atmospheric potential oxygen: New observations and their implications for some atmospheric and oceanic models, *Global Biogeochemical Cycles*, 20, doi:10.1029/2005GB002534, 2006.

Bender, M. L., Tans, P. P., Ellis, J. T., Orchardo, J., and Habfast, K.: A high precision isotope ratio mass spectrometry method for measuring the O<sub>2</sub>/N<sub>2</sub> ratio of air, *Geochimica et Cosmochimica Acta*, 58, 4751-4758, 1994.

Bender, M. L., Ho, D. T., Hendricks, M. B., Mika, R., Battle, M. O., Tans, P. P., Conway, T. J., Sturtevant, B., and Cassar, N.: Atmospheric O<sub>2</sub>/N<sub>2</sub> changes, 1993-2002:

- Implications for the partitioning of fossil fuel CO<sub>2</sub> sequestration, *Global Biogeochemical Cycles*, 19, doi:10.1029/2004GB002410, 2005.
- Bopp, L., Le Quéré, C., Heimann, M., Manning, A. C., and Monfray, P.: Climate-induced oceanic oxygen fluxes: Implications for the contemporary carbon budget, *Global Biogeochemical Cycles*, 16, 2002.
- Carpenter, T. M.: The constancy of the atmosphere with respect to carbon dioxide and oxygen content, *J. Amer. Chem. Soc.*, 59, 358-360, 1937.
- Ciais, P., Manning, A. C., Reichstein, M., Zaehle, S., and Bopp, L.: Nitrification amplifies the decreasing trends of atmospheric oxygen, *Global Biogeochemical Cycles*, 21 (2), doi: 10.1029/2006GB002799, 2007.
- Falkowski, P., Scholes, R. J., Boyle, E., Canadell, J., Canfield, D., Elser, J., Gruber, N., Hibbard, K., Höglberg, P., Linder, S., Mackenzie, F. T., Moore III, B., Pedersen, T., Rosenthal, Y., Seitzinger, S., Smetacek, V., and Steffen, W.: The Global Carbon Cycle: A Test of Our Knowledge of Earth as a System, *Science*, 290, 291-296, 10.1126/science.290.5490.291, 2000.
- Gloor, M., Sarmiento, J. L., and Gruber, N.: What can be learned about carbon cycle climate feedbacks from the CO<sub>2</sub> airborne fraction?, *Atmospheric Chemistry and Physics*, 10, 7739-7751, 10.5194/acp-10-7739-2010, 2010.
- Hamme, R. C., and Keeling, R. F.: Ocean ventilation as a driver of interannual variability in atmospheric potential oxygen, *Tellus Series B-Chemical and Physical Meteorology*, 60, 706-717, 10.1111/j.1600-0889.2008.00376.x, 2008.
- Heimann, M., and Maier-Reimer, E.: On the relations between the oceanic uptake of CO<sub>2</sub> and its carbon isotopes, *Global Biogeochemical Cycles*, 10, 89-110, 1996.
- Houghton, J. T., Ding, Y., Griggs, D. J., Noguer, M., van der Linden, P. J., Dai, X., Maskell, K., and Johnson, C. A.: IPCC, 2001: Climate Change 2001: The Scientific Basis. Contribution of Working Group I to the Third Assessment Report of the Intergovernmental Panel on Climate Change, Cambridge University Press, Cambridge, United Kingdom and New York, NY, USA, 881 pp., 2001.
- Houghton, R. A.: Balancing the global carbon budget, *Annual Review of Earth and Planetary Sciences*, 35, 313-347, 10.1146/annurev.earth.35.031306.140057, 2007.
- IPCC: Climate Change 2007: The Physical Science Basis. Contribution of Working Group I to the Fourth Assessment Report of the Intergovernmental Panel on Climate Change [Solomon, S., D. Qin, M. Manning, Z. Chen, M. Marquis, K.B. Averyt, M. Tignor and H.L. Miller (eds.)], IPCC, Cambridge University Press, Cambridge, 996 pp. pp., 2007.
- Jones, P. D., and Moberg, A.: Hemispheric and large-scale surface air temperature variations: An extensive revision and an update to 2001, *Journal of Climate*, 16, 206-223, 2003.

Keeling, C. D.: The concentration and isotopic abundance of carbon dioxide in the atmosphere, *Tellus*, 12, 200-203, 1960.

Keeling, C. D., Chin, J. F. S., and Whorf, T. P.: Increased activity of northern vegetation inferred from atmospheric CO<sub>2</sub> measurements, *Nature*, 382, 146-149, 1996.

Keeling, R. F.: Measuring correlations between atmospheric oxygen and carbon dioxide mole fractions: A preliminary study in urban air, *Journal of Atmospheric Chemistry*, 7, 153-176, 1988.

Keeling, R. F., and Shertz, S. R.: Seasonal and interannual variations in atmospheric oxygen and implications for the global carbon cycle, *Nature*, 358, 723-727, doi:10.1038/358723a358720, 1992.

Keeling, R. F., Stephens, B. B., Najjar, R. G., Doney, S. C., Archer, D., and Heimann, M.: Seasonal variations in the atmospheric O<sub>2</sub>/N<sub>2</sub> ratio in relation to the kinetics of air-sea gas exchange, *Global Biogeochemical Cycles*, 12, 141-163, 1998.

Keeling, R. F., and García, H. E.: The change in oceanic O<sub>2</sub> inventory associated with recent global warming, *Proceedings of the National Academy of Sciences of the United States of America*, 99, 7848-7853, 2002.

Keeling, R. F., and Manning, A. C.: Studies of recent changes in atmospheric O<sub>2</sub> content, in: *Treatise on Geochemistry*, edited by: Turekian, K. K., Elsevier Science, *accepted*, 2012.

Knorr, W.: Is the airborne fraction of anthropogenic CO<sub>2</sub> emissions increasing?, *Geophysical Research Letters*, 36, 10.1029/2009gl040613, 2009.

Kozlova, E. A., Manning, A. C., Kisilyakhov, Y., Seifert, T., and Heimann, M.: Seasonal, synoptic, and diurnal scale variability of biogeochemical trace gases and O<sub>2</sub> from a 300 m tall tower in central Siberia, *Global Biogeochemical Cycles*, 22, 10.1029/2008GB003209, 2008.

Langenfelds, R. L., Francey, R. J., Pak, B. C., Steele, L. P., Lloyd, J., Trudinger, C. M., and Allison, C. E.: Interannual growth rate variations of atmospheric CO<sub>2</sub> and its  $\delta^{13}\text{C}$ , H<sub>2</sub>, CH<sub>4</sub>, and CO between 1992 and 1999 linked to biomass burning, *Global Biogeochemical Cycles*, 16, 2002.

Le Quéré, C., Raupach, M. R., Canadell, J. G., Marland, G., Bopp, L., Ciais, P., Conway, T. J., Doney, S. C., Feely, R. A., Foster, P., Friedlingstein, P., Gurney, K., Houghton, R. A., House, J. I., Huntingford, C., Levy, P. E., Lomas, M. R., Majkut, J., Metzl, N., Ometto, J. P., Peters, G. P., Prentice, I. C., Randerson, J. T., Running, S. W., Sarmiento, J. L., Schuster, U., Sitch, S., Takahashi, T., Viovy, N., van der Werf, G. R., and Woodward, F. I.: Trends in the sources and sinks of carbon dioxide, *Nature Geoscience*, 2, 831-836, 10.1038/ngeo689, 2009.

Machta, L.: Oxygen depletion, *Proceedings of the International Meeting on Stable Isotopes in Tree Ring Research*, 1980, 125-127.

- Manning, A. C., Keeling, R. F., and Severinghaus, J. P.: Precise atmospheric oxygen measurements with a paramagnetic oxygen analyzer, *Global Biogeochemical Cycles*, 13, 1107-1115, 1999.
- Manning, A. C., and Keeling, R. F.: Global oceanic and land biotic carbon sinks from the Scripps atmospheric oxygen flask sampling network, *Tellus-B*, 58B, 95-116, doi:10.1111/j.1600-0889.2006.00175.x, 2006.
- Marland, G., Boden, T. A., and Andres, R. J.: Global, Regional, and National Fossil Fuel CO<sub>2</sub> Emissions. In *Trends: A Compendium of Data on Global Change*, Carbon Dioxide Information Analysis Center, Oak Ridge National Laboratory, U.S. Department of Energy, Oak Ridge, Tenn., U.S.A., 2008.
- Monnin, E., Indermuhle, A., Dallenbach, A., Fluckiger, J., Stauffer, B., Stocker, T. F., Raynaud, D., and Barnola, J. M.: Atmospheric CO<sub>2</sub> concentrations over the last glacial termination, *Science*, 291, 112-114, 10.1126/science.291.5501.112, 2001.
- Peters, G. P., Marland, G., Le Quere, C., Boden, T., Canadell, J. G., and Raupach, M. R.: Rapid growth in CO<sub>2</sub> emissions after the 2008-2009 global financial crisis, *Nature Clim. Change*, 2, 2-4, 10.1038/nclimate1332, 2012.
- Plattner, G. K., Joos, F., and Stocker, T. F.: Revision of the global carbon budget due to changing air-sea oxygen fluxes, *Global Biogeochemical Cycles*, 16, 2002.
- Randerson, J. T., Masiello, C. A., Still, C. J., Rahn, T., Poorter, H., and Field, C. B.: Is carbon within the global terrestrial biosphere becoming more oxidized? Implications for trends in atmospheric O<sub>2</sub>, *Global Change Biology*, 12, 260-271, 2006.
- Raupach, M. R., Canadell, J. G., and Le Quere, C.: Anthropogenic and biophysical contributions to increasing atmospheric CO<sub>2</sub> growth rate and airborne fraction, *Biogeosciences*, 5, 1601-1613, 10.5194/bg-5-1601-2008, 2008.
- Sarmiento, J. L., Murnane, R., and Le Quéré, C.: Air-sea CO<sub>2</sub> transfer and the carbon budget of the North Atlantic, *Philosophical Transactions of the Royal Society of London B*, 348, 211-219, 1995.
- Sarmiento, J. L., and Gruber, N.: Sinks for anthropogenic carbon, *Physics Today*, 55, 30, 2002.
- Sarmiento, J. L., Gloor, M., Gruber, N., Beaulieu, C., Jacobson, A. R., Mikaloff Fletcher, S. E., Pacala, S., and Rodgers, K.: Trends and regional distributions of land and ocean carbon sinks, *Biogeosciences*, 7, 2351-2367, 10.5194/bg-7-2351-2010, 2010.
- Severinghaus, J. P.: *Studies of the terrestrial O<sub>2</sub> and carbon cycles in sand dune gases and in Biosphere 2*, Columbia University, New York, U.S.A., 148 pp., 1995.
- Soden, B. J., Wetherald, R. T., Stenchikov, G. L., and Robock, A.: Global cooling after the eruption of Mount Pinatubo: A test of climate feedback by water vapor, *Science*, 296, 727-730, 10.1126/science.296.5568.727, 2002.

Solomon, S., Qin, D., Manning, M., Chen, Z., Marquis, M., Averyt, K. B., Tignor, M., and Miller, H. L.: IPCC, 2007: Climate Change 2007: The Physical Science Basis. Contribution of Working Group I to the Fourth Assessment Report of the Intergovernmental Panel on Climate Change, Cambridge University Press, Cambridge, United Kingdom and New York, NY, USA, 996 pp., 2007.

Stephens, B. B., Keeling, R. F., Heimann, M., Six, K. D., Murnane, R., and Caldeira, K.: Testing global ocean carbon cycle models using measurements of atmospheric O<sub>2</sub> and CO<sub>2</sub> concentration, *Global Biogeochemical Cycles*, 12, 213-230, 1998.

Stephens, B. B., Keeling, R. F., and Paplawsky, W. J.: Shipboard measurements of atmospheric oxygen using a vacuum-ultraviolet absorption technique, *Tellus Series B-Chemical and Physical Meteorology*, 55, 857-878, 2003.

Stephens, B. B., Bakwin, P. S., Tans, P. P., Teclaw, R. M., and Baumann, D. D.: Application of a differential fuel-cell analyzer for measuring atmospheric oxygen variations, *Journal of Atmospheric and Oceanic Technology*, 24, 82-94, doi:10.1175/JTECH1959.1171, 2007a.

Stephens, B. B., Gurney, K. R., Tans, P. P., Sweeney, C., Peters, W., Bruhwiler, L., Ciais, P., Ramonet, M., Bousquet, P., Nakazawa, T., Aoki, S., Machida, T., Inoue, G., Vinnichenko, N., Lloyd, J., Jordan, A., Heimann, M., Shibistova, O., Langenfelds, R. L., Steele, L. P., Francey, R. J., and Denning, A. S.: Weak northern and strong tropical land carbon uptake from vertical profiles of atmospheric CO<sub>2</sub>, *Science*, 316, 1732-1735, 10.1126/science.1137004, 2007b.

Sturm, P., Leuenberger, M., and Schmidt, M.: Atmospheric O<sub>2</sub>, CO<sub>2</sub>, and d<sup>13</sup>C observations from the remote sites Jungfraujoch, Switzerland, and Puy de Dôme, France, *Geophysical Research Letters*, 32, L17811, 2005.

Tans, P. P., Fung, I. Y., and Takahashi, T.: Observational constraints on the global atmospheric CO<sub>2</sub> budget, *Science*, 247, 1431-1438, 1990.

Thompson, R. L., Manning, A. C., Lowe, D. C., and Weatherburn, D. C.: A ship-based methodology for high precision atmospheric oxygen measurements and its application in the Southern Ocean region, *Tellus Series B-Chemical and Physical Meteorology*, 59, 643-653, doi:10.1111/j.1600-0889.2007.00292.x, 10.1111/j.1600-0889.2007.00292.x, 2007.

Tohjima, Y.: Method for measuring changes in the atmospheric O<sub>2</sub>/N<sub>2</sub> ratio by a gas chromatograph equipped with a thermal conductivity detector, *Journal of Geophysical Research-Atmospheres*, 105, 14575-14584, 2000.

Tohjima, Y., Machida, T., Watai, T., Akama, I., Amari, T., and Moriwaki, Y.: Preparation of gravimetric standards for measurements of atmospheric oxygen and reevaluation of atmospheric oxygen concentration, *Journal of Geophysical Research D: Atmospheres*, 110, 1-11, 2005a.

Tohjima, Y., Mukai, H., Machida, T., Nojiri, Y., and Gloor, M.: First measurements of the latitudinal atmospheric O<sub>2</sub> and CO<sub>2</sub> distributions across the western Pacific, *Geophysical Research Letters*, 32, 1-4, 2005b.

Tyndall, J.: Action of an intermittent beam of radiant heat upon gaseous matter, *Science* (New York, N.Y.), 2, 110-114, 10.1126/science.os-2.38.110-a, 1881.

Watson, A. J., Schuster, U., Bakker, D. C. E., Bates, N. R., Corbiere, A., Gonzalez-Davila, M., Friedrich, T., Hauck, J., Heinze, C., Johannessen, T., Kortzinger, A., Metzl, N., Olafsson, J., Olsen, A., Oschlies, A., Padin, X. A., Pfeil, B., Santana-Casiano, J. M., Steinhoff, T., Telszewski, M., Rios, A. F., Wallace, D. W. R., and Wanninkhof, R.: Tracking the Variable North Atlantic Sink for Atmospheric CO<sub>2</sub>, *Science*, 326, 1391-1393, 10.1126/science.1177394, 2009.

Wofsy, S. C.: HIAPER Pole-to-Pole Observations (HIPPO): fine-grained, global-scale measurements of climatically important atmospheric gases and aerosols, *Philosophical Transactions of the Royal Society A: Mathematical, Physical and Engineering Sciences*, 369, 2073-2086, 10.1098/rsta.2010.0313, 2011.

## **CHAPTER 2 - METHODS**

## 2.1 Introduction to chapter

In this chapter I outline the instrumentation and analytical methodology used to collect the data presented in this thesis. I describe the set up and operation of the system used to continuously measure CO<sub>2</sub> and O<sub>2</sub> concentrations in air to very high precision and accuracy. I consider the equipment used in all stages of sample collection and gas handling before discussing the two analysers used. Finally I describe the bespoke software used to automate the data collection process and also describe the calibration routines used to ensure the quality of the data.

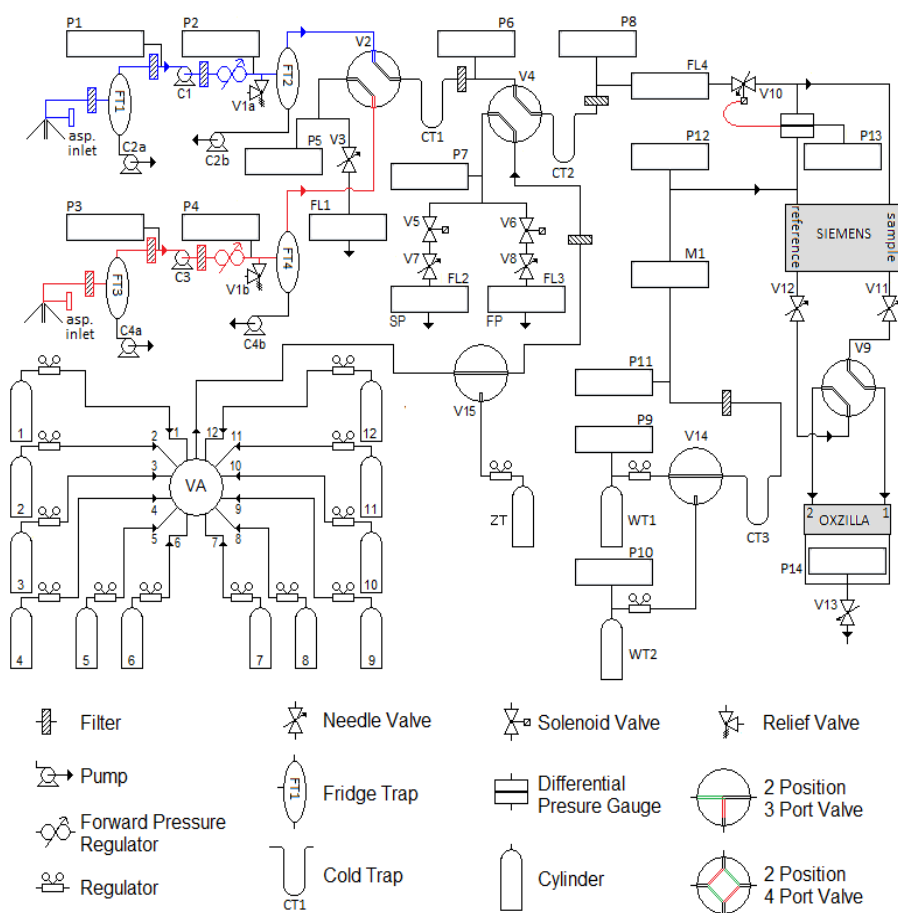


Figure 2.1. Gas handling schematic of the Weybourne O<sub>2</sub> and CO<sub>2</sub> system. 'VA' indicates a 12-port multi-position VICI Valco valve with micro-electric actuator. Pumps C2 and C4 each have two pump heads attached to a single pump drive, hence the 'a' and 'b' labels. 'P1', etc denotes pressure transducers; 'FL1' denotes flowmeter; 'M1' denotes mass flow controller. Solenoid 2-position valves are drawn in their default (de-energised) state; whereas in the legend, both possible positions are shown, in different colours. 'SP' and 'FP' indicate Slow Purge and Fast Purge, respectively, with respect to flushing cylinder regulators and tubing. 'ZT' is the Zero Tank and 'WT1/2' are the Working Tanks The cylinders numbered 1-12 show the maximum capacity of the Valco valve, these would normally comprise of calibration standards, Target Tanks, intercomparison cylinders or sample cylinders.

## 2.2 Air inlets

Figure 2.1 shows a schematic of the full gas handling system of the Weybourne atmospheric CO<sub>2</sub> and O<sub>2</sub> measurement system. Outside, ambient air is sampled from aspirated inlets located on a tower 10 m above ground level (a.g.l.). An aspirated inlet (Blaine et al., 2006), shown in figure 2.2, uses an electric blower to draw outside air into a small chamber that contains the opening of the sample line, shielding it from solar radiation and rapid temperature fluctuations associated with solar heating or night time radiative cooling. This serves to mitigate potential thermal fractionation issues at the air inlet that could otherwise have a pronounced effect on O<sub>2</sub> measurements (Manning, 2001). From the inlet, air is drawn through ¼” outside diameter (OD) Synflex 1300 tubing by a diaphragm pump (C1 and C3 in figure 2.1; KNF Neuberger Inc., model N05-ATI) located inside the building. Particulate filters are used to stop the ingress of any foreign bodies into the system. These were placed just after the aspirated inlet, at the top of the tower, where a 20 µm Swagelok TF Series filter is used, and inside the building immediately before fridge traps FT1 and FT2, where a 2 µm Swagelok FW Series filter is used. Also immediately before these fridge traps is a nylon Swagelok union which serves to protect the system from lightning strikes. This is needed since the Synflex tubing includes a conductive internal aluminium layer.



Figure 2.2. Photos of one of the aspirated air inlets fixed to the Weybourne tower.

Duplicate lines are used from the aspirated inlets to just after the first pneumatically-actuated 4-way valve (V2 in figure 2.1). V2 is used to select air from one line to go through the analysis system while the other purges through V3 at a matched flow rate of 100 mL/min. This means that the aspirated inlets, sampling

pumps (C1 and C3), and first stage of sample drying are all duplicated. The aspirated inlets themselves are at the same height but on different sides of the tower, with less than 2 m separating them. This duplication is a quality assurance procedure for the data; if switching between the two lines reveals a difference in the concentration of air being sampled then a problem with this part of the system on at least one of the lines may be inferred.

### 2.3 Drying

A two stage system is used at WAO to progressively dry the sampled air stream. The first stage consists of a refrigerator (Dometic, model DS 300 H) containing small glass traps filled with glass beads (4 mm OD). I use a medical grade refrigerator as it does not have an automated periodic defrost cycle, that would elevate the temperature for a short period of time. The primary purpose of the glass beads is to provide a greater surface area for the condensation of water vapour from the air stream. Air enters the fridge trap at the base of the trap and passes up through the glass beads before exiting at the top; this orientation is chosen to improve the flow characteristics of the air stream as it must work against the effect of gravity, and there is less likelihood of 'channelling'. The refrigerator temperature is maintained at 1 – 2°C so that the bulk of the moisture in the air can be removed as liquid water that drains to the base of the trap under gravity, and then is removed by the action of a peristaltic pump at a flow rate of 0.2 mL/min (C2 and C4 in figure 2.1, Cole Parmer Masterflex, model KH-07542-01). The sample air passes through two fridge traps per inlet line (FT1, 2, 3 and 4). At the first pass, the line pressure is below atmospheric pressure since it is upstream of the diaphragm pump (C1; C3). At the second pass downstream of the diaphragm pump, the pressure is typically in the range of 1750 – 1850 mbar absolute. A trap was placed upstream of the pump to avoid, as much as possible, water condensing inside the diaphragm pump itself, whereas the second trap after the pump is more efficient at condensing water vapour from the sample air stream owing to the elevated pressure. Particular care must be taken so that no leaks are introduced at these traps. A leak at positive pressure, in the second trap, could lead to fractionation of different gases owing to their preferential diffusion through a leak orifice depending on their molecular size (Langenfolds et al., 2005; Keeling et

al., 1998). Under vacuum, as experienced in the first trap upstream of the pump, room air may leak into the sample air stream, contaminating the sample. During the first two years or so of the WAO O<sub>2</sub> and CO<sub>2</sub> record, we experienced occasional problems with leaking fridge traps. These problems were eliminated via a redesign of the traps themselves, employing 'ball and socket' style glass connectors (GPE Scientific Ltd., size 18/7 spherical joints), where the ball includes a Viton o-ring and the ball and socket are held together with a pinch clamp. These redesigned glass fridge traps can be seen in figure 2.3.



Figure 2.3. Photo of the four glass fridge traps at WAO inside the refrigerator. The stainless steel tubing carries sample air into the base of the fridge traps and it passes up through the glass beads inside the traps and exits through the top of the traps. The yellow tubing connects to peristaltic pump heads that draw off condensed water from the base of the traps. A perforated glass disc just above the sample air inlet prevents the glass beads from blocking the peristaltic drain. In addition, the ball and socket at the sample air inlet have been fused to the trap body at a slight angle, to prevent condensed water accumulating in the inlet tubing instead of the trap itself.

Whilst the fridge traps reduce the dew point of the sample air to 1 – 2°C and remove the bulk of the moisture from the air, it is necessary to achieve a much lower and consistent dew point to ensure the accuracy and precision of the measurements. Such very low dew points are achieved with the second, cryogenic drying stage. Sample air is passed through a further two traps (CT1 and 2 in figure 2.1) immersed in an ethanol bath of a cryogenic chiller (FTS Systems, model VT490) at a constant temperature of -90°C. These so called ‘cold traps’ are electro-polished stainless steel and are filled with 4 mm OD glass beads. The purpose of the beads in these cold traps, as opposed to the fridge traps where the purpose is to provide additional surface area for condensation, is to reduce the volume of the traps. As described in Manning (2001), within the ethanol bath, an O<sub>2</sub> concentration gradient will form, since, relative to N<sub>2</sub>, O<sub>2</sub> molecules will accumulate in colder regions. Whenever there is a brief interruption to the air stream flow, for example caused by a valve switching up- or downstream, the O<sub>2</sub> concentration gradient in the cold trap will be disturbed, and will require time to re-equilibrate. This results in a transient ‘spike’ in O<sub>2</sub> concentration as recorded by the O<sub>2</sub> analyser, which will need to be discarded by the data processing routines. The time for re-equilibration of the concentration gradient in the cold trap, and thus the time for the transient O<sub>2</sub> spike to dissipate, is directly proportional to the volume of the cold trap (Manning, 2001). Thus, employing glass beads in the cold traps reduces the time for re-equilibration, and the amount of data that need to be discarded, by more than a factor of two.

The first cold trap (CT1) removes the bulk of the remaining water in the sample air stream and needs to be much larger than the second trap so that it does not block with ice too rapidly. This trap has an internal volume of 110 mL (49 mL when filled with glass beads) and, owing to eventual ice blockage, needs to be changed every 5 – 6 weeks under normal operation. Changing the trap involves diverting the air stream so that no wet air reaches the analysers, and removing and thoroughly drying the trap and glass beads with a heat gun. The second pass of sample air through the chiller is via a much smaller trap (CT2), containing 3 mm OD glass beads, with internal volume 16 mL (6 mL when filled with glass beads). The purpose of this second trap is two-fold: first, cryogenic cold trap drying efficiency

depends more on the number of times air at room temperature enters the trap, rather than on the residence time of the air inside the trap. This is because any water in the air stream that does not form ice and attach itself to the walls of the trap as it enters, will instead flow through and out of the trap as ice crystals. Thus, allowing these ice crystals to evaporate after exiting the trap, then passing the air through a second trap, results in more water being removed from the air stream via ice forming and attaching to the entrance walls of the second trap. The second purpose of CT2 is to ensure that all air streams reaching the analysers have the same dew point, thus, not only sample air, but also all calibration standards are passed through this cold trap prior to analysis. The cryogenic chiller with all three traps in place is shown in photographs in figure 2.4.

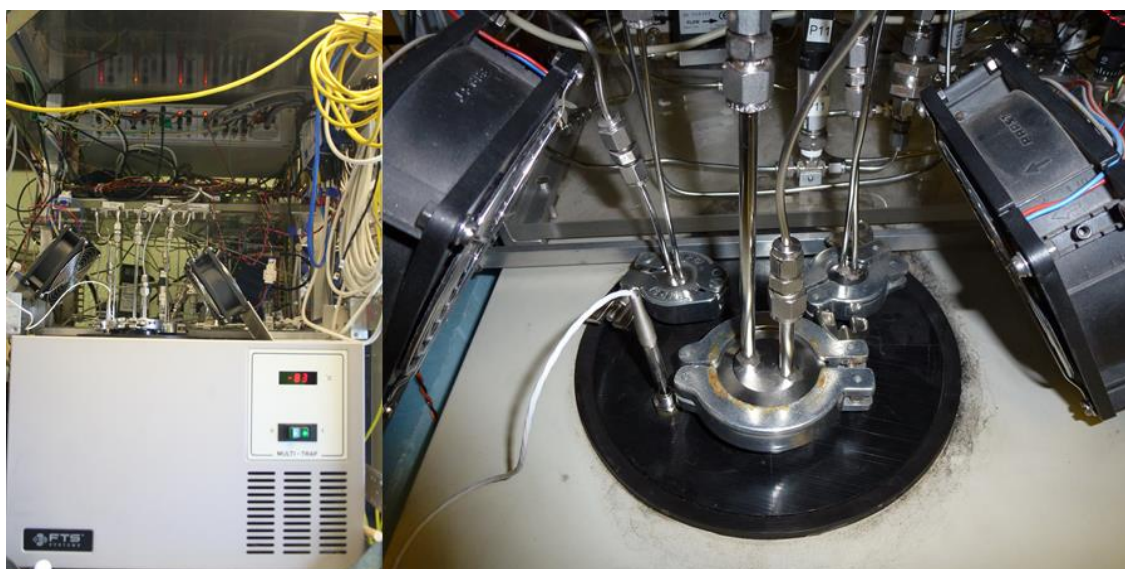


Figure 2.4. Photographs of a front on view of the chiller unit (left) and close up of the top of the chiller (right). The right hand photo shows the larger cold trap at the front (CT1) with the two smaller cold traps behind (CT2 and CT3). All traps can be easily removed from the system for cleaning via Swagelok 'quick connectors' (stainless steel with Viton o-rings, type QC4; not visible in photos). The other object visible entering the lid of the chiller is a temperature probe. The two small, black angled fans that can be seen on the right and left edges of the right hand photo are an essential addition to the system, preventing condensation forming on the lid that would otherwise create a puddle and seep inside the chiller, potentially damaging the electrical circuitry.

A third cold trap in the chiller (CT3 in figure 2.1), identical to CT2, is used to ensure that 'Working Tank' (WT; defined below) air is also at the same dew point as sample and calibration standard air when it reaches the analysers. The two smaller traps have a much longer lifetime than CT1; ambient air has already been

thoroughly dried by the previous traps, and WT and calibration standard cylinders are filled with already dried air. Thus, these smaller traps only need to be cleaned out once a year to avoid ice blockage.

## 2.4 Gas handling

In order to achieve the very high precision and accuracy targets required for O<sub>2</sub> measurement it is necessary to pay careful attention to detail with the gas handling when designing, building and running an analysis system. Many of the special requirements for O<sub>2</sub> also help to maintain or improve accuracy and precision for CO<sub>2</sub> measurement. The need for dedicated aspirated air inlets has been covered in section 2.2. Flow rates and pressures in the system must be carefully controlled, and, in particular, it is crucial that both flow rate and pressure in the sample air stream are matched very closely to those in the WT air stream.

When designing the system, the sample and reference air stream pathways were designed to be as close to identical as possible, particularly in the portion of the system from the small cold traps (CT2 and CT3) onwards. This means that careful attention was given to matching components, tubing lengths and dead volumes in both air stream pathways.

Pressure and flow control can usually be considered together; if air streams passing through two identical lengths of tubing have the same pressure drop across them, then their flow rates will also be the same. Very fine control of the pressure on both sample and reference sides of the system is achieved by using a differential pressure gauge (MKS Instruments, Baratron 223B; P13 in figure 2.1) and an electronic controller (MKS Instruments, 250E) that feeds back to a solenoid valve (MKS Instruments, 248A; V10 in figure 2.1). This system is capable of maintaining zero differential pressure between the two air streams, with a precision of better than  $\pm 0.1$  mbar. The system flow rate is established on the reference (WT) side of the system, to 100 mL/min using a mass flow controller (MFC; M1 in figure 2.1, MKS model 1179, 200 sccm range). The pressure on the sample side of the system is then matched using the MKS equipment described above, and because I use identical components and tubing lengths on the two sides as described above, this helps to ensure that the flow rate of both reference and

sample sides are also matched. As a diagnostic check, the flow rate on the sample side is measured with a mass flow meter (FL4, figure 2.1). The pressure on the reference side after the MFC is measured at P12 (figure 2.1) and the pressure on the sample side can be inferred from the P12 reading together with the read out of the differential pressure provided by the MKS Baratron and shown at P13 (figure 2.1). Metering valves (V11 and V12, figure 2.1, Brooks Instrument, model 8504) placed after the Siemens analyser, but before a solenoid 4-way valve (V9, Numatics, TM Series, figure 2.1) allow fine control of the restriction on each side to ensure that the matched pressures do result in matched flows. These two Brooks valves can effectively correct for any potential difference in the flow restriction on either side caused by small differences in volume or the slightly different components used on each line.

Both the CO<sub>2</sub> and O<sub>2</sub> analyser have reference and sample cells. The CO<sub>2</sub> analyser is utilised in typical fashion in that the reference cell is supplied by an air stream of constant composition from a high pressure cylinder (which I call 'Working Tank', WT). In the case of the O<sub>2</sub> analyser, owing to a more variable baseline signal, it is necessary to rapidly (once every 60 seconds) alternate which cell is the reference cell and which is the sample cell (Stephens et al., 2007). This is achieved with a 4-way solenoid valve (V9 in figure 2.1; Numatics TM Series). Finally, a needle valve (V13, figure 2.1, Swagelok SS Series) is placed just after the combined sample and reference air streams exit the O<sub>2</sub> analyser. This is used to adjust the restriction in both sample and reference lines in order to fine tune the magnitude of the pressure drop across the MFC in the reference line and the MKS solenoid valve (V10, figure 2.1) in the sample line. There is a minimum pressure drop required in order for each of these components to accurately control flow.

## 2.5 Analysers

For CO<sub>2</sub> measurement, I use a commercially available non-dispersive infra red (NDIR) analyser from Siemens Corp., model Ultramat 6E. This analyser is similar to the Li-Cor™ analysers more commonly used by the CO<sub>2</sub> measurement community, but where the Siemens Ultramat has been shown to be capable of higher precision, most likely owing to its larger sensor cell (88 mL compared to 9 mL in the Li-Cor™

analysers) (Kozlova and Manning, 2009). The Siemens analyser has a sample and reference measurement cell, each with a volume of 88 mL. The difference between the infrared (IR) absorption of the sample and WT reference air is measured and converted to a CO<sub>2</sub> mole fraction based on the regular calibration procedures carried out that establish the analyser's response function, as described in section 2.7. Operating in such a differential mode improves accuracy and precision in comparison to absolute techniques and also helps to eliminate interference and uncertainty caused by analyser baseline response. NDIR measurements of CO<sub>2</sub> mole fraction are very dependent on the ambient temperature. The effects of fluctuations in temperature are mitigated somewhat by operating in differential mode, but in order to reduce temperature fluctuations further, all of the equipment is housed in an air conditioned room and the Siemens analyser is further insulated with 2" thick foam to increase its thermal mass. So-called 'Zero Tank' (ZT) calibration analyses (section 2.7) further mitigate the problem of analyser baseline response drift due to temperature fluctuations.

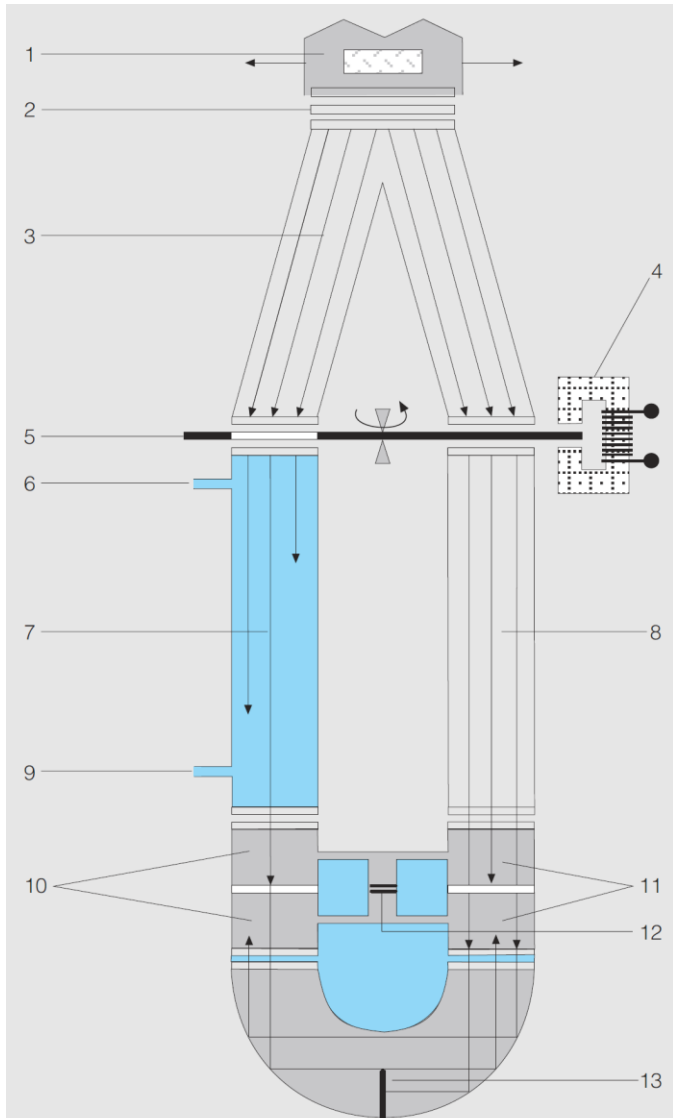


Figure 2.5. Schematic of the Siemens Ultramat 6E CO<sub>2</sub> analyser, taken from the Siemens user manual. (1) indicates the IR source; (2) is an optical filter; (3) is a beam splitter to split the IR beam into both sample and reference cells; (4) is an eddy current drive; (5) is a chopper, to rapidly alternate the beam between sample and reference cells; (6) and (9) show the sample air inlet and outlet ports (for my version of this analyser, the reference cell also has analogous inlet and outlet ports, not shown in the figure); (7) and (8) are the sample and reference cells, respectively; (10) and (11) are the sample and reference detector cells, respectively; and (12) is a capillary tube with microflow sensor connecting the two detector cells; (13) is an optical coupler.

Most NDIR analysers report CO<sub>2</sub> concentration via solid state IR detectors that measure changes in the light intensity of the IR beam after it has passed through the sample (and reference) cell. Changes in IR intensity can be inversely correlated with the CO<sub>2</sub> concentration in the sample cell, owing to IR absorption by the CO<sub>2</sub> molecules. A somewhat different detection principle is used by the Siemens Ultramat analyser, however, taking advantage of the fact that a different amount of

energy will be transmitted through the sample and reference cells (when they have different CO<sub>2</sub> mole fractions). Two sealed detector cells containing pure CO<sub>2</sub> are located behind the sample and reference cells (see figure 2.5), and are connected to each other by a capillary tube with a microflow sensor. The CO<sub>2</sub> in the detector cells absorbs all of the IR radiation that passes through the sample and reference cells. There are two detector cells for each of the sample and reference side; the detector is designed as a double-layer detector. The centre of the absorption band is preferentially absorbed by the upper detector layer and the edges of the absorption bands are absorbed equally in the upper and lower cells. This arrangement ensures a narrow band of spectral sensitivity. The difference in the transmitted IR due to the difference in CO<sub>2</sub> mole fraction in the sample and reference cells causes the two detector cells to increase in temperature differentially. The temperature difference between the two detector cells results in a pressure difference that in turn causes a very small flow between the two detector cells through the capillary tubing connecting them. This flow is measured by the microflow sensor, and is proportional to the difference in CO<sub>2</sub> mole fraction between the sample and reference cells (Manning and Crotwell, 2012).

O<sub>2</sub> measurements are performed using an Oxzilla II (Sable Systems Inc.) analyser that employs fuel cell technology to measure O<sub>2</sub> concentration. The fuel cells contain a weakly acidic electrolyte solution isolated from the air stream by a semi-permeable membrane. Air diffuses across the membrane, and within the fuel cell the following electrochemical reaction takes place:



The lead atoms are supplied by the anode, the protons from the electrolytic solution and a gold cathode completes the cell. The resultant change in potential difference across the cell is measured and this is proportional to the rate at which O<sub>2</sub> diffuses across the membrane and therefore also to the partial pressure of O<sub>2</sub> in the air stream. Samples are always measured as a difference from the WT air being measured concurrently in the other cell. The sample and WT air streams are swapped to the alternate cell, via 4-way valve, V9, every 60 seconds, with the first 30 seconds of measurement after each valve switch being discarded, shown conceptually in figure 2.6.

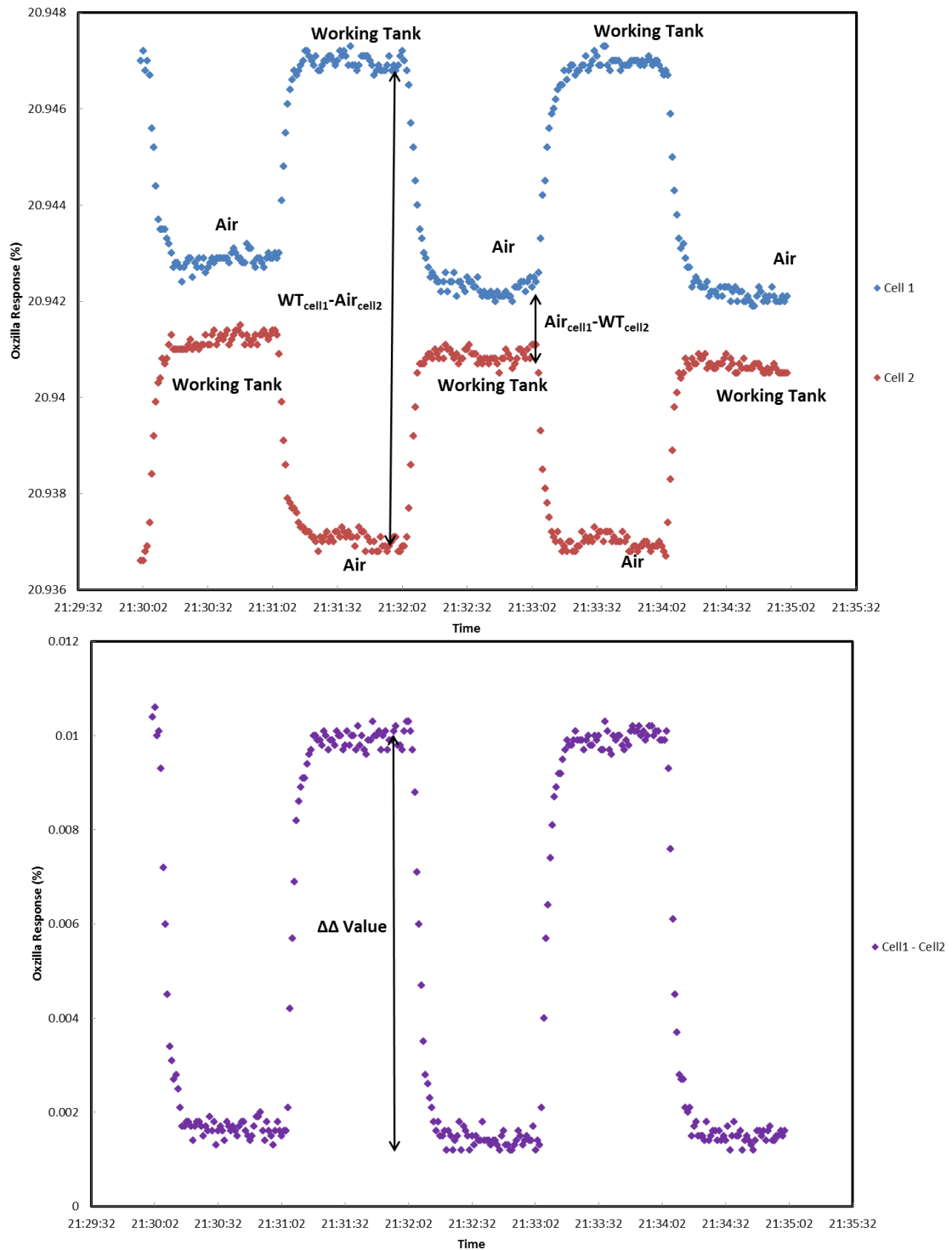


Figure 2.6. The ' $\Delta\Delta$ ' value used to mitigate baseline drift in the two fuel cells and to improve the sensitivity of  $O_2$  measurements. The top plot shows 5 minutes of raw data from both cells of the Oxzilla analyser. Each cell alternates between sampling either ambient air or Working Tank (WT), alternating every minute. The bottom plot shows the result of cell 1 minus cell 2 for the same example data. A  $\Delta\Delta$  value is calculated from the difference of the cell differences. In other words, as  $(WT_{cell1} - Air_{cell2}) - (Air_{cell1} - WT_{cell2})$ . As well as cancelling out most drift in fuel cell baseline response,  $\Delta\Delta$  values are approximately twice as sensitive to variations in  $O_2$  concentration than an individual fuel cell and so sensitivity to small variations in ambient air is increased.

The switching eliminates most of the drift that the individual fuel cells' responses may experience on timescales longer than the switching interval, 60 seconds. This valve switching also has the beneficial advantage of doubling the sensitivity of the measurement. Instead of simply subtracting a reference signal from a sample signal, three consecutive (sample - WT) jog differences are calculated (see bottom panel of figure 2.6) and the difference between these jog differences is calculated, referred to as a ' $\Delta\Delta$ ' value, and indicated with the black arrow shown in the bottom panel of figure 2.6.

Some changes are made to the off the shelf Oxzilla II unit to make it suitable for high precision measurement. All internal plastic tubing is removed and replaced with 1/8" OD stainless steel tubing; the outlets of the two cells are combined into a single outlet, in an effort to minimise pressure differences in the two cells and the Oxzilla's internal pressure sensor is replumbed so that it measures the outlet line pressure, rather than ambient pressure. The fuel cells' responses are also temperature dependent so active temperature control is used to maintain a constant 32°C inside the Oxzilla.

## 2.6 Data acquisition and software

The need for extreme care to be taken with the gas handling to ensure the precision of the O<sub>2</sub> measurements makes it necessary to record a relatively large range of diagnostics, both to monitor the performance of the analytical system in real time and to help with quality assurance of the data in post data processing. The system is also designed to run in automated unattended fashion, to minimise the need for maintenance and routine human intervention, which has obvious advantages for instrumentation at a field site. These two factors led to the need for a very sophisticated bespoke software and data acquisition package. Bespoke software was designed and refined over a number of years in collaboration with software engineer, Alex Etchells at UEA/ENV, as well as with the assistance of UEA/ENV electronics technicians. The software can control almost all aspects of the running of the system, from switching individual valves to processing the analyser signals in order to provide a calibrated response. The software also provides real time displays of the status of the system so that a user can log into

the field station computer remotely to check on the status of the system. The software is also able to make automated decisions on the quality of the data collected, and, for example, if a calibration run is deemed unsatisfactory, the system will automatically decide to continue to process ambient air measurements with the previous 'good' calibration results.

A number of diagnostic tools have been included in the design of the system. These include pressure transducers (Wika, model A-10) covering a range of pressures depending on their location within the system and flow meters (FL1, 2, 3 in figure 2.1; McMillan flow meter, model 113; FL4, McMillan mass flow meter, model 50). It is important to mention that although these diagnostic sensors are of great assistance to ensuring the quality of the data and troubleshooting when problems occur, it is also important not to install too many sensors, since each extra sensor introduces extra dead volume to the system, and extra connections and therefore more potential sites for leaks to occur. Locations of sensors were carefully chosen to provide the maximum degree of information about the state of the system from the smallest number of sensors. In addition, where possible, sensors were located in 'purging' pathways rather than in the line for sample analysis.

Data from all diagnostic sensors are recorded along with the analysers' raw data every 30 seconds in a diagnostic data file. This diagnostic file is called the 'DIG' file, with a new file created by the software on a daily basis. All the DIG data files can be accessed remotely and I have written an IDL routine to plot graphs of all the diagnostic data parameters. This IDL routine is run on a daily basis to update the plots so that all the diagnostics for the previous day can be seen along with the raw analyser signals. This information is spread across four pages, an example of which can be seen in figure 2.7, and allows quick identification of any problems as they are developing or before too much data are compromised. My IDL routine also has the flexibility of producing these diagnostic plots on hourly, daily, weekly, monthly and yearly time intervals, allowing a wide variety of features or trends in diagnostic parameters to be examined.

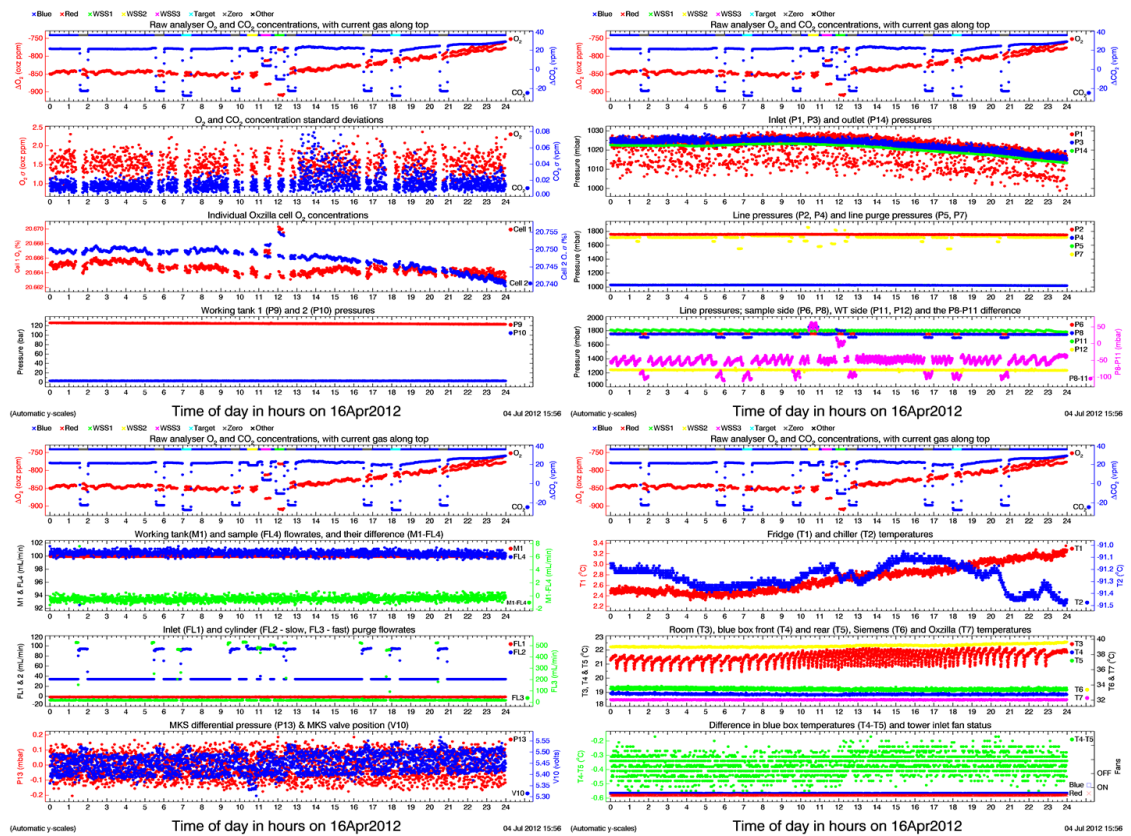


Figure 2.7. Example daily ‘DIG’ diagnostic plots. The diagnostic data are plotted over four pages and data for all sensors (collected every 30 seconds) are plotted. The top panel of each of the four pages shows the raw analyser signals, since one often wants to examine for possible correlations or influences on the analyser signal from diagnostic parameters. The top panels also have a colour coded bar along the top to indicate what the system is analysing at that point in time (generally ambient air or a calibration cylinder). Hourly, weekly, monthly and annual DIG plots are also produced to examine features in more detail, or to examine trends over longer periods. The daily plots shown here are often most useful in rapidly identifying potential problems with the system from the previous day. The labels for the diagnostic parameters shown in the plots correspond to the sensor labels in the gas handling diagram in figure 2.1, and to those in the software screenshot below in figure 2.8.

Data collection is mediated by USB (universal serial bus) data acquisition modules (Minilab, model 1008 and Labjack, model U12) and also by a NI DAQ card (National Instruments Inc.) connected to the system computer via a serial connection. The bespoke software, written in C#, interprets these signals to provide both a real time display and also to record data in a number of CSV (comma separated values) files. The front page of the user interface of the C# software has an overall gas handling schematic of the system as well as showing the status of key variables and is presented in figure 2.8.

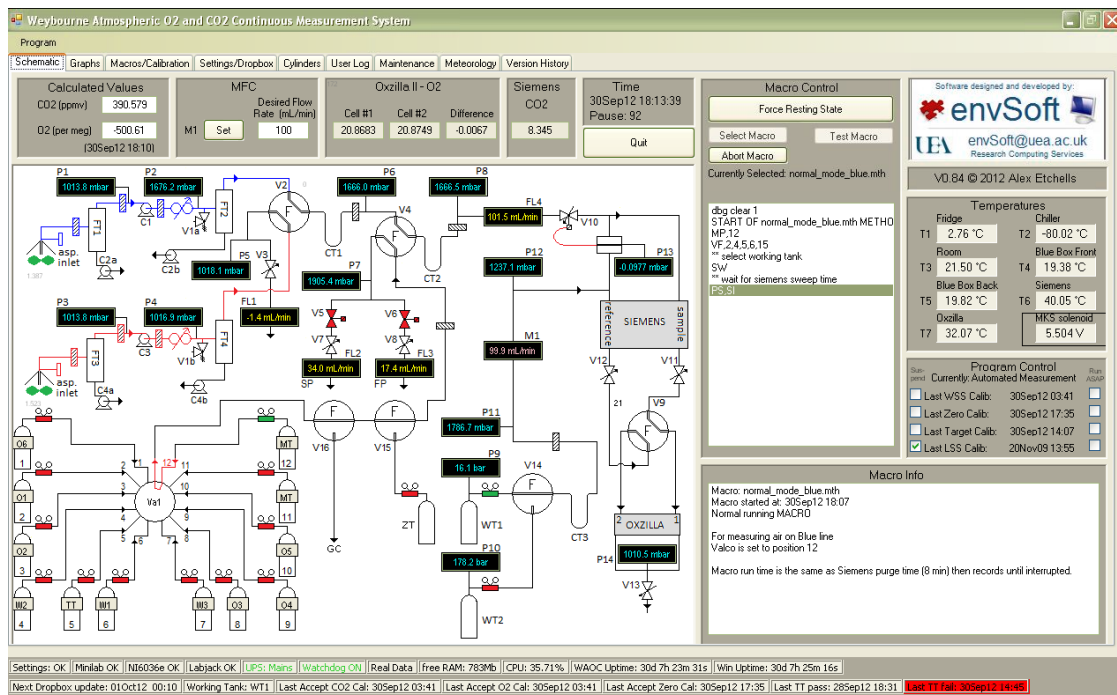


Figure 2.8. The front page of the user interface for the software that controls the Weybourne CO<sub>2</sub> and O<sub>2</sub> system. The main display is an overall gas handling schematic of the system. This schematic presents real time displays of many of the system diagnostics such as pressures and flow rates. The solenoid valves shown on the schematic can be controlled by ‘clicking’ on them with a computer mouse; calibration cylinders can also be manually analysed on the system via clicking on the appropriate cylinder. Raw analyser data are displayed in real time above the gas handling schematic along with calculated concentration values based on the most recent calibration analysis parameters. Temperatures are displayed in a box on the right of the screen. The ‘macro control box’ provides information on the macro that is currently running (macros are small, user-written programs that control a sequence of settings for the system and are explained in section 2.7). The two rows at the bottom of the display give an overview of the computer and data acquisition status as well as recent calibration activity. The text boxes are colour co-ordinated to rapidly inform the user of any problems that may have occurred.

In addition to the overall gas handling schematic of the system, there are a number of additional tabs which serve different functions; presenting additional information, allowing the entry of various settings and parameters to control the system and allowing the user to keep a log of events related to the operation of the system. Three of the most important tabs are presented in figures 2.9, 2.10 and 2.11.

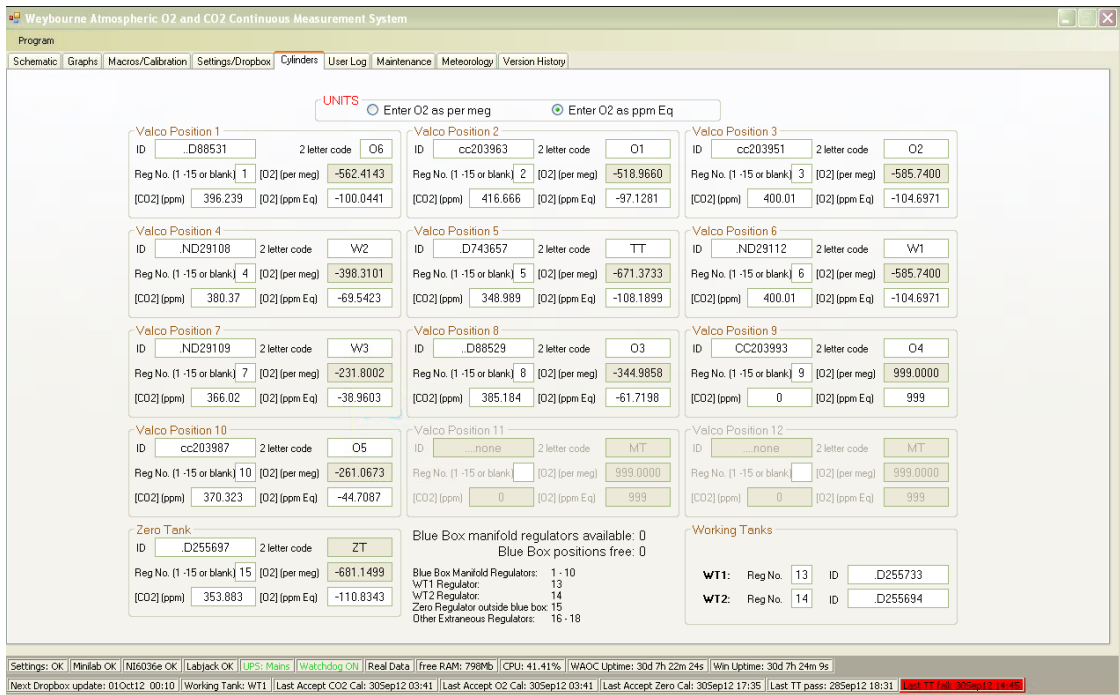


Figure 2.9. The 'Cylinders' tab. In this tab all information identifying cylinders connected to the multi-position Valco valve, as well as the Working Tanks, is presented. The cylinder identification numbers, and CO<sub>2</sub> and O<sub>2</sub> concentrations are entered by the user for all calibration cylinders, and each cylinder is assigned a regulator number and a Valco valve number. The Valco valve number is understood by the user-created macros that call certain cylinders for calibration runs. A two letter code is also assigned to identify each cylinder's purpose (this code is also entered into data files).

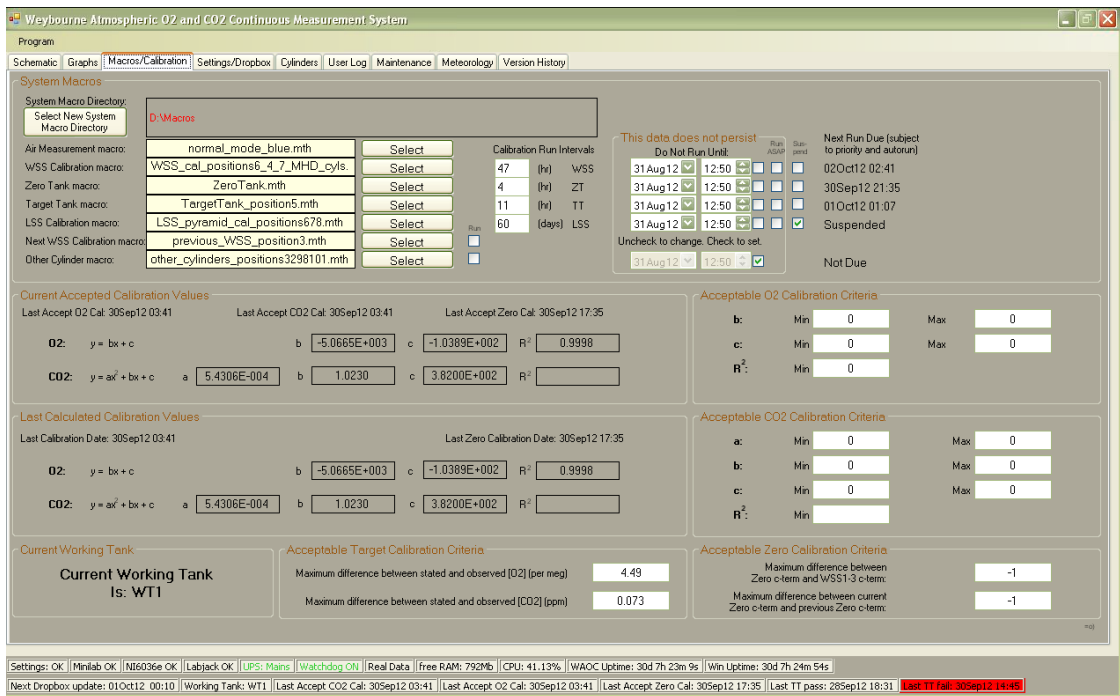


Figure 2.10. The 'Macros/Calibration' tab. Macros are small, simple, user-written programs that control a sequence of settings for the system and are explained in section 2.7. In this tab the user can assign a certain macro text file to be run at a

definable interval for each of the types of calibration or cylinder analysis runs that can be performed. Macros can also be suspended, run 'asap' or delayed until a defined date and time. This tab also displays the most recent equations for the CO<sub>2</sub> and O<sub>2</sub> calibration parameters and allows the user to set acceptability limits for the calibration parameters and Target Tank analyses. If a calibration or Target Tank run falls outside of these limits then it will be flagged in the data files.

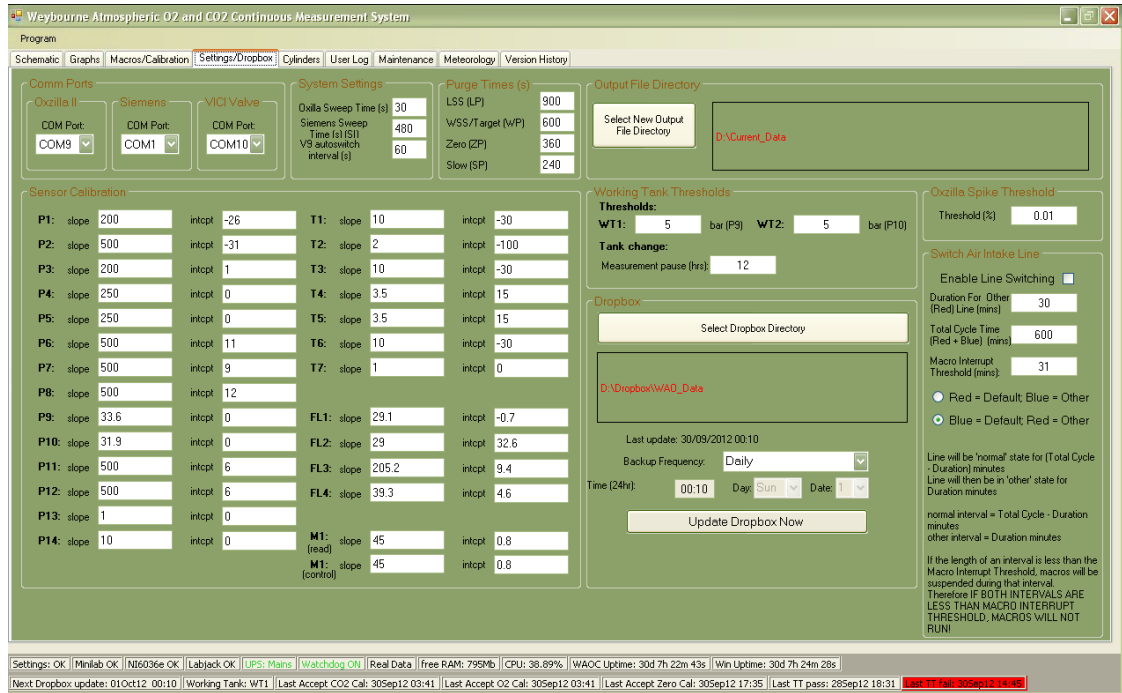


Figure 2.11. The 'Settings/Dropbox' tab. This tab allows a number of system settings to be entered. The user can assign communication ports for the analysers and Valco valve. The user can enter time settings for important parameters such as sweep-out times for the system and analysers, and the interval at which sample air and WT air are switched between the Oxzilla fuel cells. Linear calibration curves for each of the diagnostic sensors are defined separately and entered in this tab. The user can also change the threshold pressure at which the Working Tank will automatically be swapped out of the system. 'Spikes' of less than one second duration are sometimes observed in the response of Oxzilla cells; these can be removed by the software and the sensitivity to the spikes can be set in this tab. Also on this tab, one can define the location of the output data files and the time at which data files are backed up to the 'Dropbox' and made accessible remotely. Finally, alternate switching between the two air sampling lines installed on the tower can be set up at a defined interval from this tab. This can be an important diagnostic tool, since any concentration differences observed between the two line would indicate a problem in one or both lines.

## 2.7 Calibration

The necessity for highly precise measurements has been emphasised throughout this thesis and perhaps the most important factor in maintaining high accuracy and

precision is the need for regular analyses of well characterised high pressure cylinders to calibrate the response of the analysers.

The response of the Siemens analyser is non linear to CO<sub>2</sub> mole fraction and so I adopt a quadratic calibration curve of the form:  $y = ax^2 + bx + c$ . To define the parameters of the calibration curve (a, b and c) a minimum of three calibration standards are needed. For the Oxzilla, the fuel cells' response is highly linear (of the form:  $y = mx + c$ ) and so a minimum of two calibration standards are needed to determine the slope and intercept of the calibration curve. These are the minimum number of calibration standards needed; in order to calculate the R<sup>2</sup>, goodness of fit parameter for the calibration curves, at least one more calibration standard than the minimum is required.

At Weybourne routine calibrations are performed with a suite of three high pressure cylinders called WSSes (Working Secondary Standards), but a fourth cylinder will be added to this suite in the near future to improve the calibration curves generated and allow calculation of R<sup>2</sup> values for CO<sub>2</sub>. WSS calibrations are run every 47 hours; this time is chosen not to be a multiple of 24 hours to prevent possible aliasing of calibration results. The WSSes are cylinders filled with dried air to between 140 and 200 bar that have been analysed against primary calibration standards filled at international CCLs (Central Calibration Laboratories) in order to characterise the cylinders and establish their concentrations on the international WMO-defined scales (e.g. the NOAA (National Oceanic and Atmospheric Administration) X2007 scale for CO<sub>2</sub> and the SIO (Scripps Institution of Oceanography) S2 scale for O<sub>2</sub>). Using these cylinders defined on the central scales at WAO helps to ensure compatibility with other measurements worldwide (Manning and Crotwell, 2012). The concentrations of O<sub>2</sub> and CO<sub>2</sub> in the cylinders are chosen to bracket the range of concentrations that is expected to be observed at WAO; this ensures that the best fit of the calibration curves is over the range of concentrations to be measured and helps assure the quality of the data.

A fourth calibration cylinder, called the Zero Tank (ZT) is run much more frequently than the three point WSS calibrations and is used to correct for baseline drift in the CO<sub>2</sub> calibration curve (as opposed to drift in the span (also called

‘sensitivity’) or non-linearity, which are captured by the full WSS calibration). Baseline drift is typically much more variable (Manning and Crotwell, 2012) than span or non-linearity drift, and is usually caused by external factors such as ambient temperature variability. The ZT is run immediately after the three point calibration to establish an initial baseline response and CO<sub>2</sub> concentration value in the cylinder. It is subsequently run every 3-4 hours to redefine the baseline analyser response; any change from the initial baseline response is assumed to be owing to analyser drift and the magnitude of this change is applied as a correction to the c-term of the calibration curve for CO<sub>2</sub> (the c-term or intercept is most susceptible to any drift in detector response).

There can be a misconception that this cylinder has a zero concentration of CO<sub>2</sub>, and historically this approach has sometimes been used, for example running a pure N<sub>2</sub> cylinder to directly measure the intercept of the calibration curve. Instead the ZT should contain an ambient concentration of CO<sub>2</sub> that lies within the range of concentrations found within the WSSes. Since this is the range that the calibration fit is best for, measurements made in this range will have the lowest uncertainty from calibration factors. The name ‘Zero Tank’ is retained as the measurements of the tank are still used to correct the intercept, the analyser response at zero CO<sub>2</sub> concentration. It is worth noting here that whilst the O<sub>2</sub> concentration of the ZT is measured it is not a calibration cylinder for O<sub>2</sub> and no corrections or changes are applied to the O<sub>2</sub> calibration curve based on the results of this cylinder. If the ZT is kept according to best practice for O<sub>2</sub> measurements (i.e. stored horizontally in a thermally insulated environment) then the results of ZT runs can be used diagnostically in a manner similar to those for the Target Tank (TT).

### 2.7.1 Theory behind Zero Tank corrections to the C-term of the CO<sub>2</sub> calibration equation

CO<sub>2</sub> is considered to have a quadratic relationship between measurement and concentration in the form of the following equation:

$$y = Ax^2 + Bx + C \tag{2.2}$$

The intercept value (C) in the CO<sub>2</sub> calibration equation is known to drift over time and this value is corrected based on periodic automatic running of the ZT.

The initial intercept value (C<sub>0</sub>) is set by measuring 3 calibration standards (WSSes) on the analyser. Immediately following this the first ZT run is performed and this sets the initial concentration value for CO<sub>2</sub> in the ZT (M<sub>0</sub>), this is necessarily calculated using the calibration parameters that have just been defined including C<sub>0</sub> and it is assumed that no drift in the analyser response has occurred between the end of the calibration run and the start of the ZT run.

$$\text{After calibration: } y = Ax^2 + Bx + C_0 \quad (2.3)$$

$$\text{After initial ZT run: } [CO_2] = M_0 \quad (2.4)$$

The ZT is then run at fixed intervals after the calibration (typically set at 3-5 hours) and the concentration measured is compared to the initial concentration (M<sub>0</sub>). The difference between concentrations is used to adjust the C-term of the calibration coefficients and account for any drift in detector response. Subsequent ZT concentrations will be denoted as M<sub>1,2,...n</sub> so M<sub>1</sub> is the first run after the initial run and so on.

The first ZT run after the initial run gives a concentration value, M<sub>1</sub>, calculated from the calibration equation using C<sub>0</sub>. The difference between M<sub>1</sub> and the initial concentration, M<sub>0</sub>, is then used to adjust C<sub>0</sub> to C<sub>1</sub> so that if C<sub>1</sub> were used then the ZT CO<sub>2</sub> concentration would be the same as initial, i.e., M<sub>1</sub>=M<sub>0</sub>. This accounts for any drift in the C-term of the analyser's response since the initial ZT run:

$$C_1 = C_0 + (M_0 - M_1) \quad (2.5)$$

On the next ZT run M<sub>2</sub> is calculated, it is important to note here though that the value of M<sub>2</sub> is calculated using the adjusted value of the constant, C<sub>1</sub>. Since the value of C<sub>1</sub> accounted for any analyser drift between initial and first runs, if there has been no further drift between the first and this second run then one would expect M<sub>2</sub> to equal the initial concentration, M<sub>0</sub>. If there has been some drift in the C-term then one must again correct for this drift and to do this must reference back

to the initially defined concentration, not the previous concentration, and apply this correction to the currently used C-term, therefore:

$$C_2 = C_1 + (M_0 - M_2) \quad (2.6)$$

This can seem counter intuitive as one is correcting for drift since the last ZT run and so it seems that one should be comparing the current concentration value to the previous one (i.e. the difference between  $M_n$  and  $M_{n-1}$ ). However these concentrations are calculated using different C-terms ( $C_{n-1}$  and  $C_{n-2}$  respectively) and the C-term used to calculate the current value has already taken into account all drift observed between the initial ZT run and the previous ZT run, so any difference between the current ZT value,  $M_n$ , and the initial value,  $M_0$ , is due to analyser drift since the last ZT run. The equation for the C-term correction may therefore be generalised as follows:

$$C_n = C_{n-1} + (M_0 - M_n) \quad (2.7)$$

It is also worth noting at this point that in our \*ZERO.csv data file we record '(current-base)CO<sub>2</sub>' in one column and '(current-previous)C-term' in the next column and these are always equal but of opposite sign. This can be seen by rearranging equation 2.7:

$$C_n - C_{n-1} = M_0 - M_n \quad (2.8)$$

$$M_n - M_0 = C_{n-1} - C_n \quad (2.9)$$

To illustrate the zero correction in a simplified sense, the following numerical example is included using equation 2.10 as the starting point for the calibration curve:

$$y = x^2 + x + 10 \quad (2.10)$$

The initial run of the ZT immediately following the calibration shows it's concentration to be 100 units:

$$M_0 = 100 \quad (2.11)$$

4 hours later the first run of the ZT after the initial run gives a concentration of 101 units:

$$M_1 = 101 \quad (2.12)$$

The analyser's response has drifted so the ZT value is now 1 unit higher than it was initially. This drift is assumed to be entirely in the most sensitive C-term and so the C-term is adjusted accordingly:

$$C_1 = C_0 + (M_0 - M_1) = 10 + 100 - 101 = 9 \quad (2.13)$$

Subsequent ZT runs would each be treated referring back to the original value for 100 as we are only correcting for drift since the last ZT run. So, if we were to run the ZT again immediately (assuming no drift while we run it) then we would get a concentration value of 100 units, equal to the initial run. In practice we don't do this, instead the second ZT run will occur 4 hours later, and now we get a concentration value of 103 units:

$$M_2 = 103 \quad (2.14)$$

This time the analyser's response has drifted so the ZT value is now 3 units higher than it would have been if we'd run it immediately after the last adjustment, and 3 units higher than initially. The C-term must be adjusted again:

$$C_2 = C_1 + (M_0 - M_2) = 9 + 100 - 103 = 6 \quad (2.15)$$

This process is repeated until the next full calibration is run.

This consideration of the corrections to the CO<sub>2</sub> calibration equation based on ZT runs does highlight the fact that this methodology is based on taking a snap-shot of the drift in the system and then applying this correction to subsequent data points. In order to minimise data inaccuracies based on analyser drift ZT should be run as often as possible. Also assuming that drift is not random but continuous with time then the most accurate data will be immediately after a calibration or ZT run and accuracy will reduce with time from this point until the next calibration or ZT run.

## 2.7.2 Target Tank role and results

The TT should not be described as a calibration cylinder as it plays no role in calibrating the system. Instead it is a cylinder that is well characterised with known concentrations of CO<sub>2</sub> and O<sub>2</sub> that is run as a standard to check the performance of the system. At WAO the TT was run every 8-9 hours so you can check the performance of the system at various stages of the 47 hour WSS calibration cycle. Values can be entered in the settings tab for the maximum allowable deviation from the defined values of the TT. If the results of a TT run fall outside these limits for either CO<sub>2</sub> or O<sub>2</sub> then the relevant species is flagged. If there is no explanation for the anomalous TT results, for example a spike in detector response or a bad diagnostic during the run, then there is a question over the validity of the calibration for this period and the air data for the relevant species must be discarded or recalibrated manually from a subsequent calibration, if possible.

The results of all the TT runs for the entire duration of the WAO record are shown in figure 2.12. The results from the current and 3 previous TTs (January 2009 – April 2012) are shown in figure 2.13. The plots show the differences from the declared values of both CO<sub>2</sub> and O<sub>2</sub> (plotted as the measured minus declared), with different cylinders plotted in different colours to clearly show when a cylinder change has taken place.

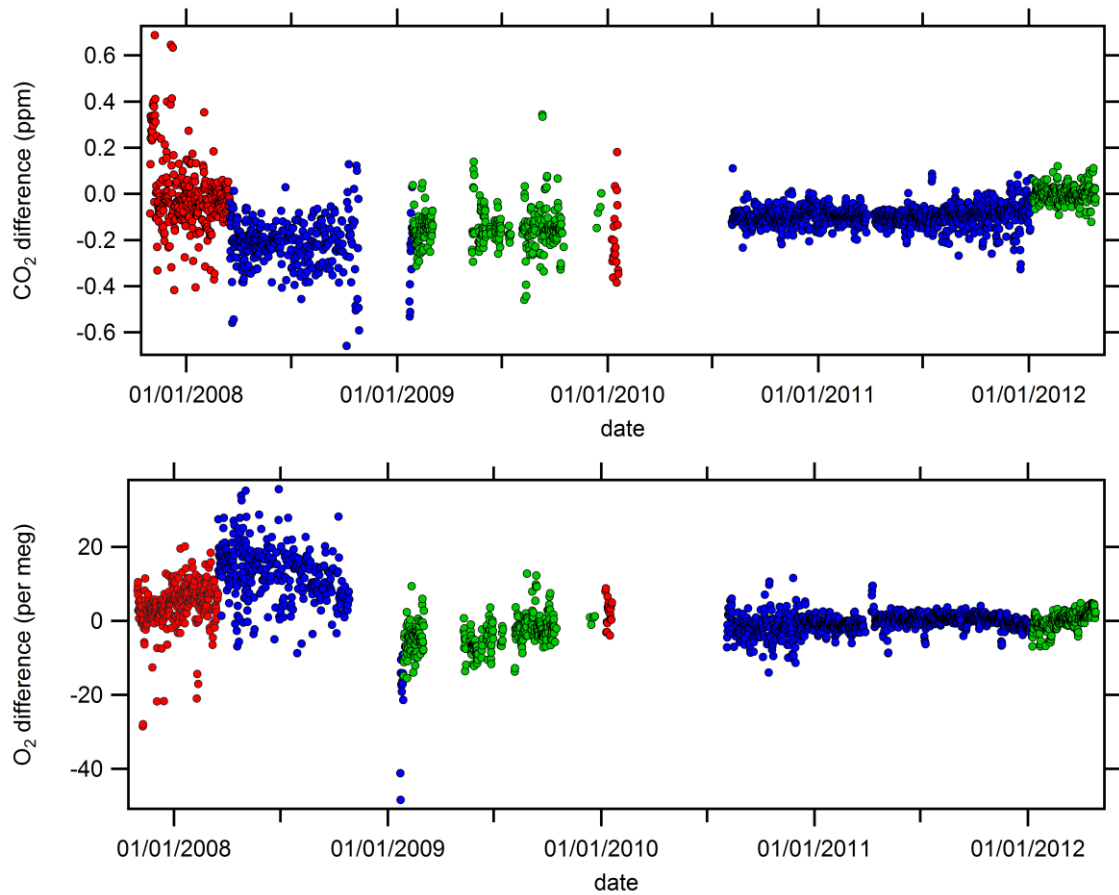


Figure 2.12. Target Tank (TT) runs at Weybourne Atmospheric Observatory (WAO) for the entire data record covering the period October 2007 to April 2012. Data were filtered to remove TT runs during periods of bad data, for example when Working Tank flow was lost. Different TTs are shown in different colours and concentration differences are plotted as the measured minus declared TT value.

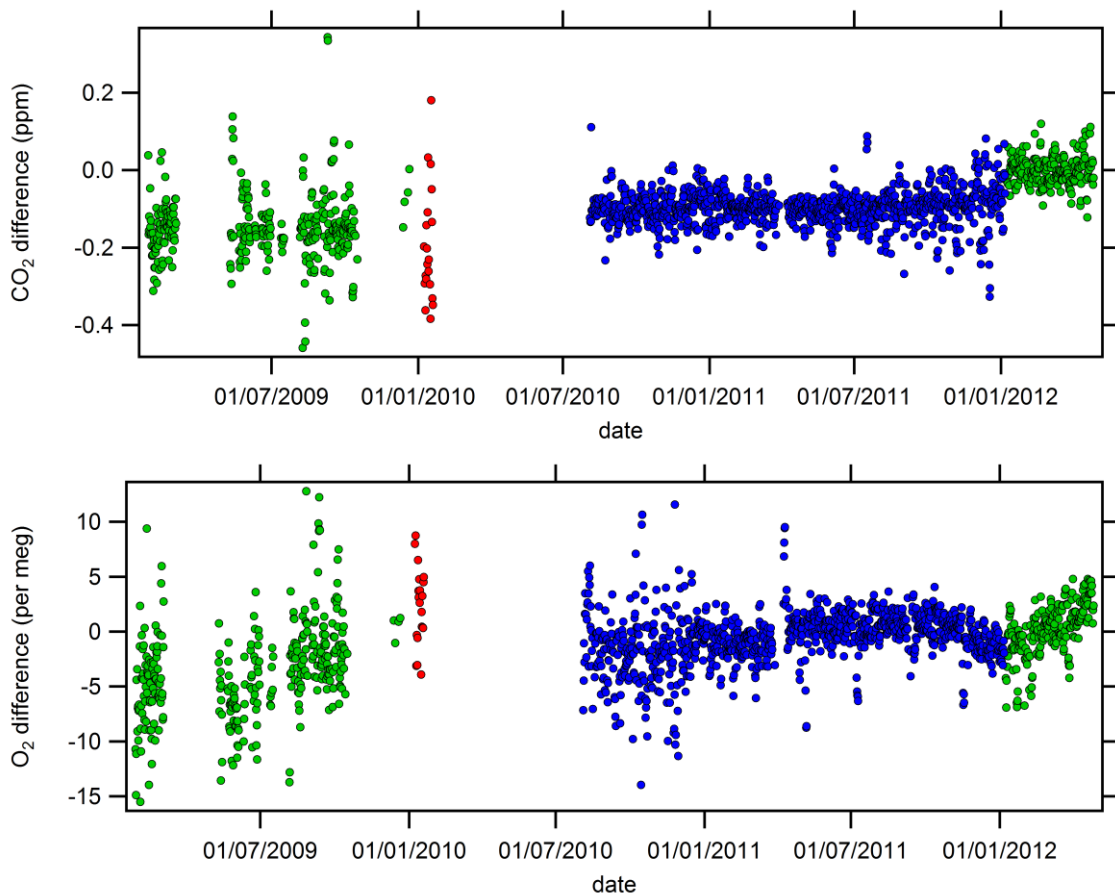


Figure 2.13. Target Tank (TT) runs at Weybourne Atmospheric Observatory (WAO) for the 4 most recent TTs covering the period January 2009 to April 2012. Data were filtered to remove TT runs during periods of bad data, for example when Working Tank flow was lost. Different TTs are shown in different colours and concentration differences are plotted as the measured minus declared TT value.

Figure 2.13 shows that there was a marked improvement in precision for both CO<sub>2</sub> and O<sub>2</sub> after 2008 and a further, more dramatic improvement in the precision of both species after the series of equipment upgrades during late 2009 and early 2010. O<sub>2</sub> precision shows another improvement at the beginning of January 2011, this was when both Oxzilla fuel cells were replaced as the old fuel cells were discovered to exhibit sudden jumps in their response. Due to the variability shown in the early measurements, pre 2009, it was decided that the curve fits presented for this data record in the forthcoming chapters would be based on air data collected after 2009. An investigation has begun into the early period of data to look for any calibration issues that may have influenced the data in an effort to improve the quality of the data for the early part of the record. The investigation will not be in time for inclusion in this thesis.

Each TT measurement is the average of six 2-minute averages for both CO<sub>2</sub> and O<sub>2</sub> after a suitable period of flushing to allow measurement cell concentrations to equilibrate. For the most recent 2 TTs the average standard deviation within a TT run (n=1229) was 0.0068 ppm for CO<sub>2</sub> and 2.8 per meg for O<sub>2</sub>. The total standard deviation of all 1229 TT runs was 0.057 ppm for CO<sub>2</sub> and 2.5 per meg for O<sub>2</sub>. Taking the standard deviation of pairs of consecutive TT runs and then averaging the standard deviation of the pairs (n=1228) gave a value of 0.022 ppm for CO<sub>2</sub> and 1.1 per meg for O<sub>2</sub>. These values show that for this most recent period of data the precision for both CO<sub>2</sub> and O<sub>2</sub> is very good. The precision for CO<sub>2</sub> is within the WMO repeatability goal of  $\pm 0.05$  ppm. However it has been demonstrated that repeatabilities an order of magnitude higher can be achieved with NDIR CO<sub>2</sub> analysers and so this remains an area that we are looking to improve in the future at WAO. The repeatability achieved in the recent record for O<sub>2</sub> is also within the WMO goal of  $\pm 5$  per meg and for a field station we are very pleased with this result that compares favourably to other laboratories around the world.

An estimate of precision was also obtained from sampled air data in order to better represent the performance of the system during ambient air measurement rather than cylinder measurement. Using data from ambient air measurements gives a more conservative estimate of the performance of the full analytical system, rather than measuring a high pressure cylinder, which does not pass through the air inlets, sample pump, and full drying system. I chose a one hour period of data when ambient concentrations of CO<sub>2</sub> and O<sub>2</sub> were very stable. The standard deviation of all two minute data points during this hour was then taken (n=30) and gave a precision of 2.0 per meg for O<sub>2</sub> and 0.03 ppm for CO<sub>2</sub>. This is thought to be a good estimation of the actual precision of measurements during ambient air sampling under normal operation. A period of 1 hour was chosen as hourly averages of data are often used for further data processing. In order to get an estimate of the precision over shorter timescales this hour was split into six 10-minute periods and the standard deviation of each taken. These standard deviations were then averaged to give a 10-minute precision estimate of 0.02 ppm for CO<sub>2</sub> and 2.0 per meg for O<sub>2</sub>. The data used to provide these stable air estimations of precision is shown below in figure 2.14.

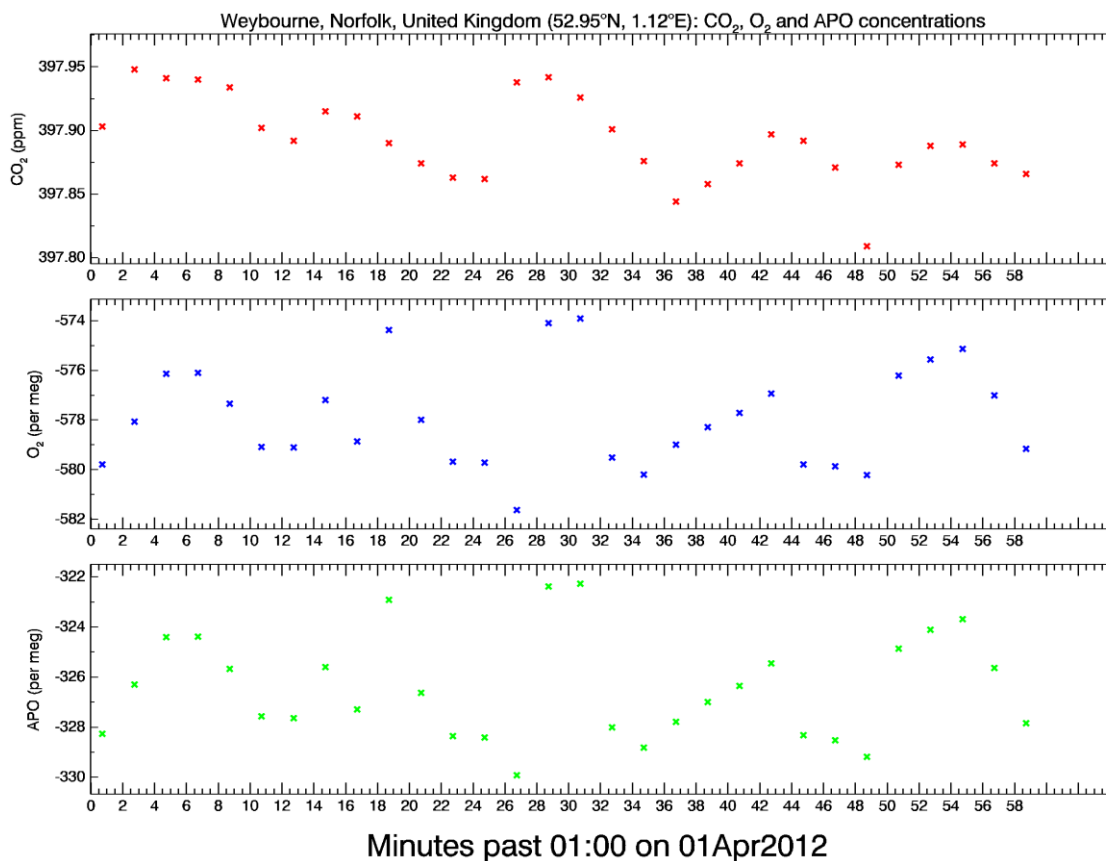


Figure 2.14. CO<sub>2</sub>, O<sub>2</sub> and APO data from Weybourne Atmospheric Observatory covering the one hour period, 01:00 – 02:00 on 1<sup>st</sup> April 2012. These data were used to estimate the precision of the system during measurement of ambient air as concentrations of O<sub>2</sub> and CO<sub>2</sub> were particularly stable.

### 2.7.3 Hierarchy and macro control of calibration

Whenever a cylinder is run at WAO it is run as a sample and measured against the WT reference gas, analogous to during air measurements. A calibration run is triggered at a defined interval entered as a setting in the software. There is also an hierarchy to the importance of the individual calibration runs so that if two calibrations are called at the same time the software knows which one takes preference. The hierarchy, in order of decreasing importance is: WSS, ZT, Other, TT. The sequence of events initiated when a calibration is called is defined by the user in a file called a Macro, this file is written in a very simple programming language that is understood by the software. At the start of each calibration run the relevant cylinder is chosen by the Valco valve (VA, figure 2.1), or in the case of the ZT by V15 (figure 2.1). Gas from this cylinder then travels through stainless steel tubing, through V4 and V6 is opened so the cylinder can ‘fast purge’ at an elevated

flow rate of 500 mL/min for 10 minutes for a WSS, TT, or next WSS calibration or 6 minutes for a ZT calibration. This is to flush the tubing of any remnants from a previous calibration run and also to flush the regulator for each cylinder. At the end of this interval, V6 is closed and V5 is simultaneously opened, the needle valve V8 is set so that a flow rate of 100 mL/min is achieved through V6 and the cylinder is now allowed to 'slow purge' for 4 minutes. This step equalises the purging flow rate with the flow rate that is set through the analysers to avoid a sudden spike in flow and pressure when V4 is switched and flow is directed towards the sample side of the analyser. At the end of the slow purge period V4 is switched so that the calibration gas now flows to the analysers and ambient air is now directed to V6, which remains open, and is purged. Now the macros ensure that there is an interval, set to 8 minutes, called the Siemens sweep out which allows the new calibration gas to fully replace, sweep out, any ambient air that remains in the 88 mL sample cell volume of the Siemens analyser. This step avoids any mixing of calibration and ambient air that would influence the concentration values observed, after this interval is completed recording is turned on and data are saved to the relevant data file for the calibration being run. Data are then recorded for 12 minutes for WSS, TT or next WSS runs, or for 10 minutes for ZT runs, before the macro is finalised and the system can then call the next calibration macro, if due, or return to measuring ambient air (after another Siemens sweep out period with ambient air is observed).

#### 2.7.4 Stability of WT concentrations

The stability in the concentrations of the WT can be informed as a secondary result of the WSS calibrations. Since all measurements are taken against the reference of the WT this means that the intercept of the calibration curves for both CO<sub>2</sub> and O<sub>2</sub> do not tell you the analyser response to a zero concentration of each species but instead tell you the WT concentration at the point of calibration. Since a 50 L WT is consumed in approximately 8 weeks it is possible to build up a lot of data on cylinder stability in a relatively short time compared to those for calibration cylinders. It has been shown O<sub>2</sub> concentrations in cylinders drop as the cylinder becomes depleted (Manning, 2001). The effect is most probably caused by preferential desorption of N<sub>2</sub> relative to O<sub>2</sub> from the cylinder walls as the cylinder

pressure falls. At WAO WT cylinders are run until the pressure remaining is around 5 bar and so we would expect to see some depletion effects. The residuals of CO<sub>2</sub> and O<sub>2</sub> for all WT concentrations for the duration of the entire WAO record are plotted in figure 2.15.

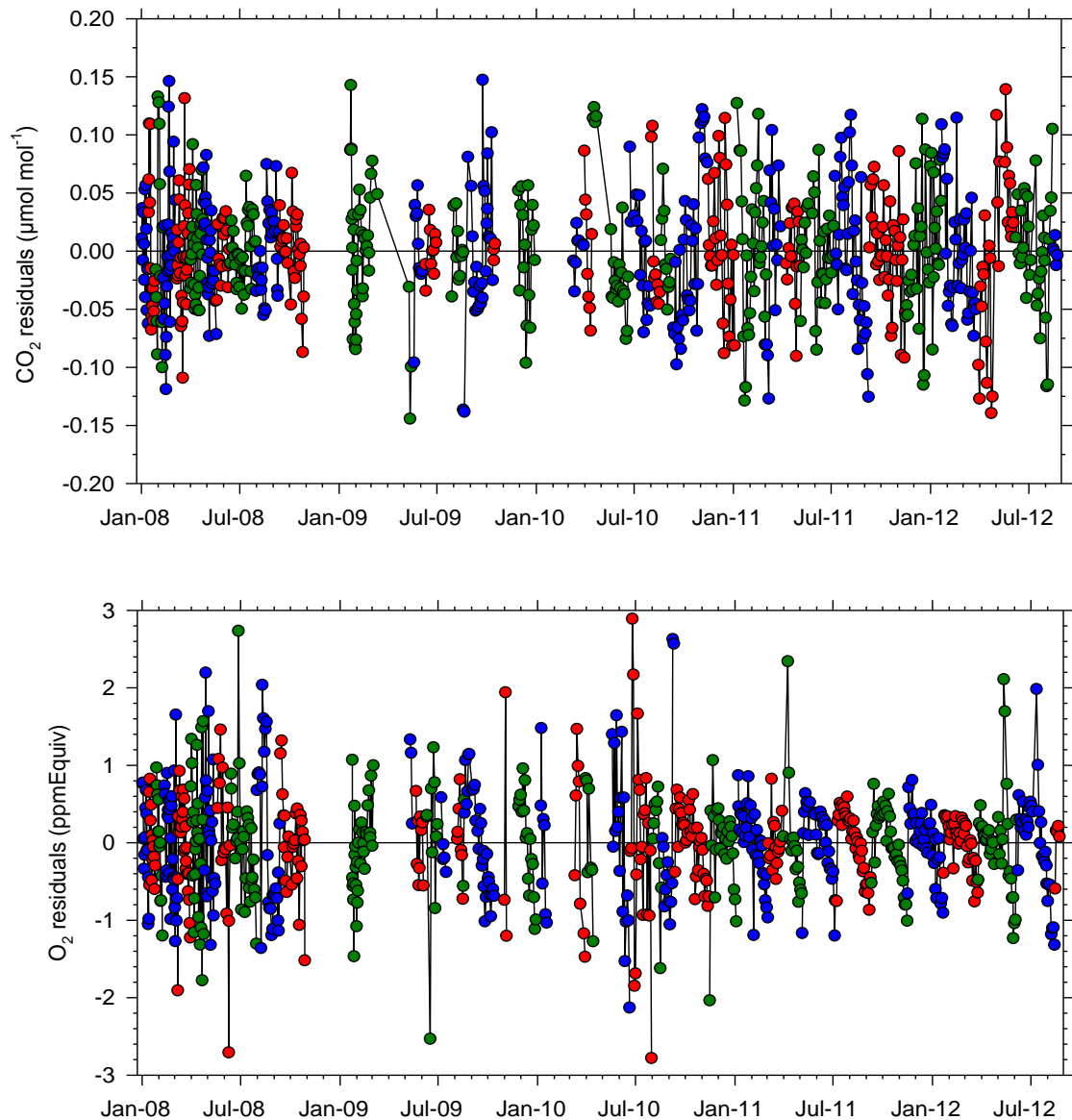


Figure 2.15. Shows variability in Working Tank (WT) CO<sub>2</sub> and O<sub>2</sub> mole fraction as recalculated after each routine calibration which occurs once every 47 hours in normal operation. Colours indicate when one WT cylinder is depleted (to ~5 bar) and exchanged for a different, full cylinder; 'zero' is the average mole fraction for each WT, typically between 385-395 ppm for CO<sub>2</sub> and -110 and -80 ppmEquivalent for O<sub>2</sub>. The 'ppmEquivalent' unit used here is the O<sub>2</sub> concentration to which the Oxzilla O<sub>2</sub> analyser responds. A change of 1 ppmEquivalent in O<sub>2</sub> is equal to a change of 6.04 per meg in O<sub>2</sub>/N<sub>2</sub> ratio, if all other species are held constant.

The data in figure 2.15 demonstrate that CO<sub>2</sub> mole fraction in high pressure cylinders appears not to drift when the cylinders are orientated horizontally, to pressures as low as 5 bar, in contrast to O<sub>2</sub> in which decreasing mole fraction is observed. This O<sub>2</sub> depletion is shown more clearly in Figure 2.16, which zooms in on the last two years of the record shown in Figure 2.15. The O<sub>2</sub> depletions experienced at WAO were generally less than 2 ppmEquiv, in line with Manning (2001) and less than reported by Kozlova and Manning (2009). No consistent depletion effect was noted in CO<sub>2</sub> concentrations. The O<sub>2</sub> depletion is insightful in terms of possible implications to the stability of O<sub>2</sub> in primary and secondary calibration standards, but is not a problem, however, in WTs, since part of my calibration methodology is to allow WT concentrations to be redefined after every WSS calibration, and then to use this redefinition until the subsequent WSS calibration.

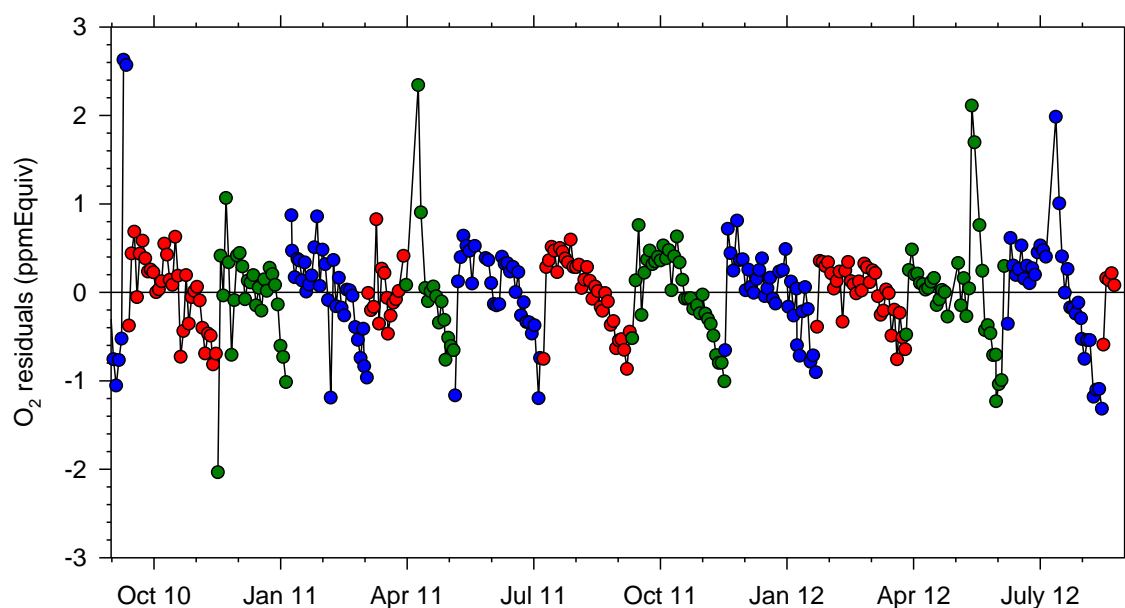


Figure 2.16. Same as the bottom panel of figure 2.14, except showing only from September 2010 to August 2012, to highlight the decreasing O<sub>2</sub> mole fraction observed as WT cylinders are depleted.

## 2.8 Intercomparison activities

WAO is actively involved in the global carbon cycle community. For long-term records to be useful on a global scale it is essential to ensure compatibility of results so that a measured concentration of 390 ppm CO<sub>2</sub> at WAO is compatible to a measured concentration of 390 ppm CO<sub>2</sub> at any other station or laboratory. One

way to keep track of compatibility is to participate in round robin schemes whereby samples from a central laboratory are sent round to all participating laboratories and stations where blind analysis is undertaken. The results of the analysis from all the individual labs are then compared to check that the labs analysis are comparable and to look for any offsets in scale that might exist. When this exercise is repeated a number of times it can also provide information on the stability of your own laboratory's calibration scale over time.

WAO routinely participates in the Cucumber and GOLLUM (Global Oxygen Laboratories Link Ultra-precise Measurements) intercomparison programs. Both of these programs consist of loops linking laboratories together and suites of 3 high pressure cylinders are circulated between the laboratories all over the world (the Cucumber program was started as part of CarboEurope but has recently expanded to include laboratories in USA, Canada, Japan and Australia). The Cucumber program compares many greenhouse gas and related compounds but WAO currently only participates with measurements of CO<sub>2</sub> and O<sub>2</sub>. WAO also participates in both CO<sub>2</sub> and O<sub>2</sub> measurements in the GOLLUM program. In general two sets of cylinders are circulated in opposite directions around the loop and results are reported online. Any laboratory may check their historical performance at any time but results are also reviewed every two years at the WMO CO<sub>2</sub> experts / greenhouse gas measurement techniques meeting.

The WAO results from the Cucumber program are shown in figure 2.17 along with the results for the other laboratories within the Inter-1 loop that WAO is a part of. The GOLLUM results are similarly shown in figure 2.18.

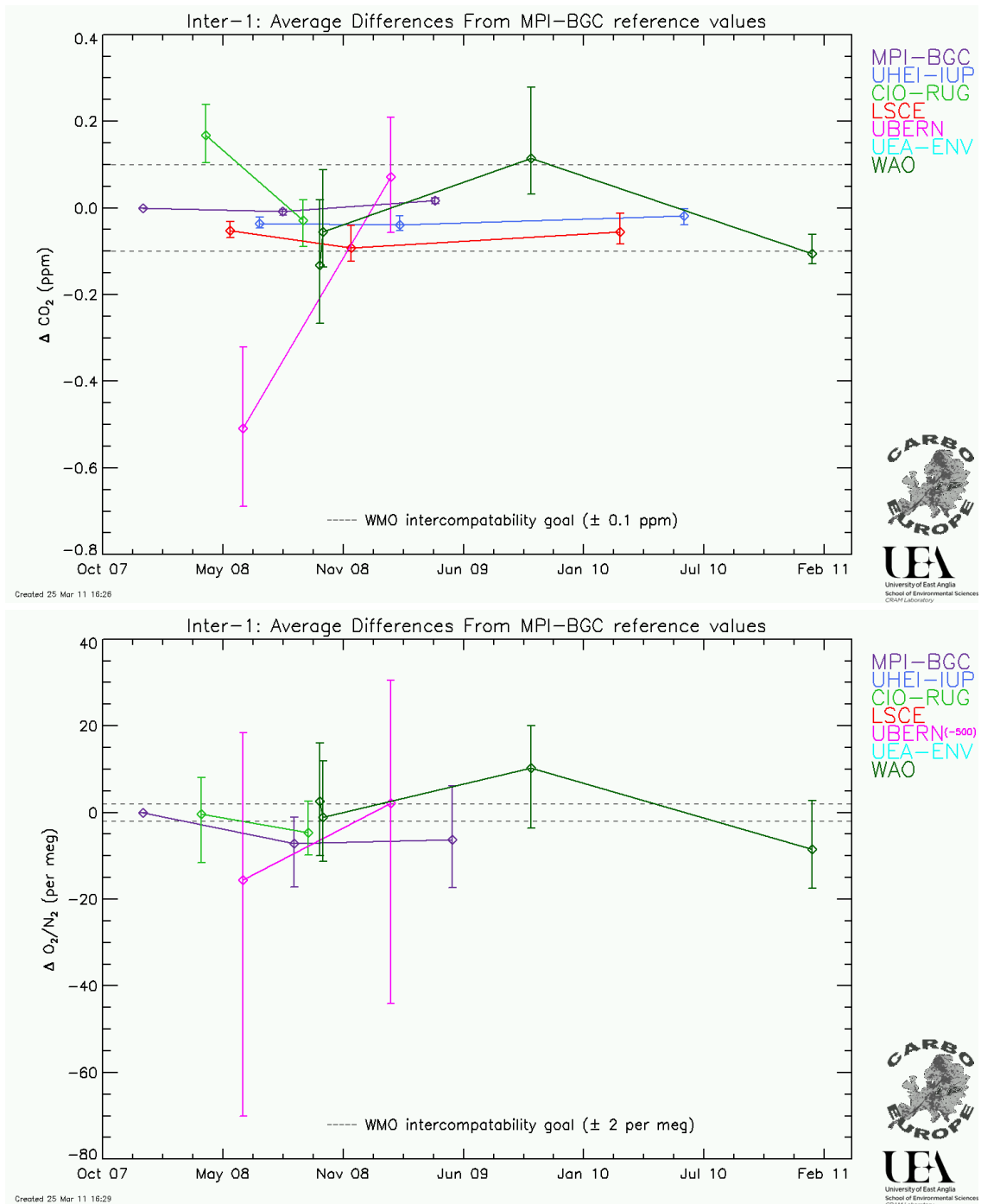


Figure 2.17. Results of Cucumber intercomparison cylinders run at Weybourne Atmospheric Observatory (WAO) for CO<sub>2</sub> (top) and O<sub>2</sub> (bottom), in dark green on both plots. The other laboratories that analyse the same cylinders from the loop that WAO participates in (Inter-1) are also shown and the dashed lines represent the WMO compatibility goal.

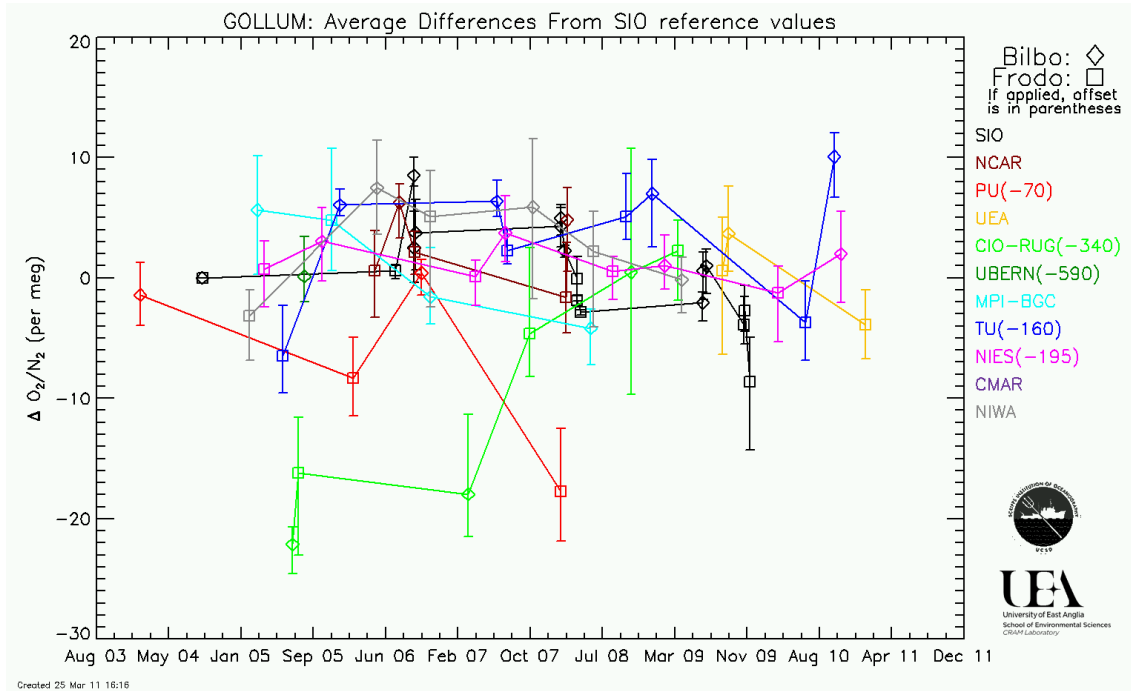
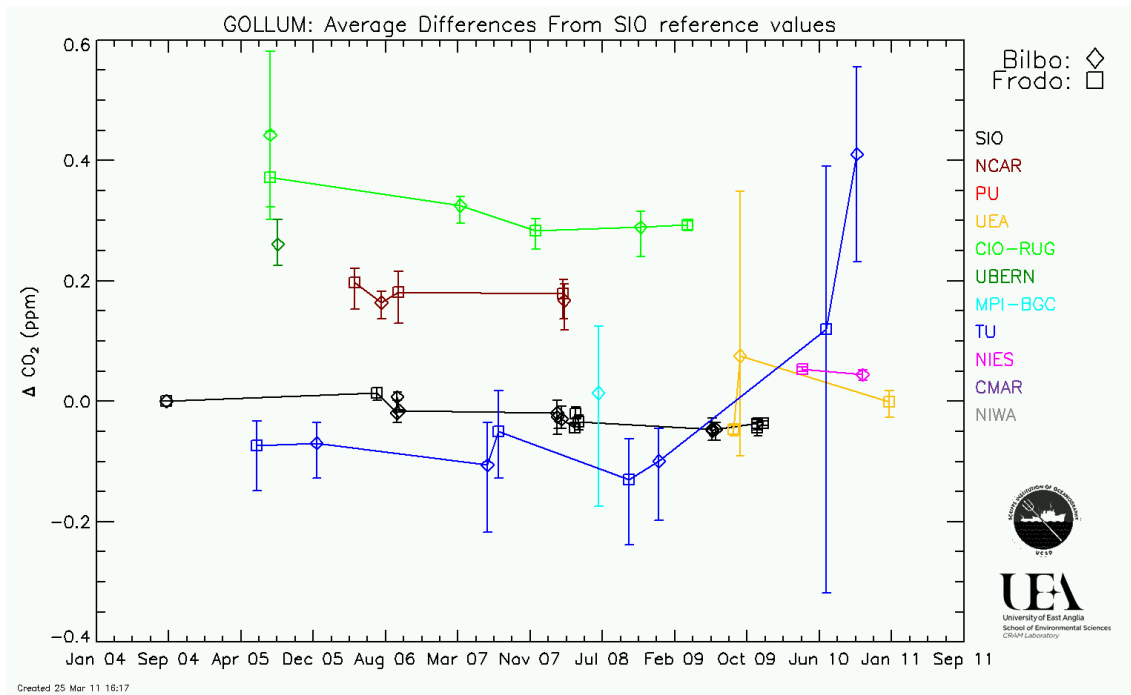


Figure 2.18. Results of GOLLUM intercomparison cylinders run at Weybourne Atmospheric Observatory (WAO) for  $\text{CO}_2$  (top) and  $\text{O}_2$  (bottom), in yellow and labelled UEA on both plots. The other laboratories' results from the GOLLUM loop are also shown.

These results show that the compatibility at WAO is in line with other established stations within the carbon cycle community. WAO is extremely close to routinely achieving the WMO compatibility goal for  $\text{CO}_2$  measurements of  $\pm 0.1$  ppm for these types of analysis. For  $\text{O}_2$  there is some way to go in order to achieve the WMO compatibility goal of  $\pm 2$  per meg, this goal is an aspirational one with the current

state of O<sub>2</sub> measurements as none of the laboratories currently measuring O<sub>2</sub> worldwide can achieve this. The compatibility of O<sub>2</sub> measurements made at WAO is in line with results from other laboratories.

## 2.9 References

Blaine, T. W., Keeling, R. F., and Paplawsky, W. J.: An improved inlet for precisely measuring the atmospheric Ar/N<sub>2</sub> ratio, *Atmospheric Chemistry and Physics*, 6, 1181-1184, 2006.

Keeling, R. F., Stephens, B. B., Najjar, R. G., Doney, S. C., Archer, D., and Heimann, M.: Seasonal variations in the atmospheric O<sub>2</sub>/N<sub>2</sub> ratio in relation to the kinetics of air-sea gas exchange, *Global Biogeochemical Cycles*, 12, 141-163, 1998.

Kozlova, E. A., and Manning, A. C.: Methodology and calibration for continuous measurements of biogeochemical trace gas and O<sub>2</sub> concentrations from a 300-m tall tower in central Siberia, *Atmospheric Measurement Techniques*, 2, 205-220, 10.5194/amt-2-205-2009, 2009.

Langenfelds, R. L., van der Schoot, M. V., Francey, R. J., Steele, L. P., Schmidt, M., and Mukai, H.: Modification of air standard composition by diffusive and surface processes, *Journal of Geophysical Research D: Atmospheres*, 110, D13307, 2005.

Manning, A. C.: Temporal variability of atmospheric oxygen from both continuous measurements and a flask sampling network: Tools for studying the global carbon cycle, Scripps Institution of Oceanography, University of California, San Diego, La Jolla, California, U.S.A., 202 pp., 2001.

Manning, A. C., and Croswell, A. M.: Minimising uncertainty and error in atmospheric measurement of CO<sub>2</sub>: Part I. Analysers, calibration and gas handling, *Atmos. Meas. Tech. Discuss.*, *submitted*, 2012.

Stephens, B. B., Bakwin, P. S., Tans, P. P., Teclaw, R. M., and Baumann, D. D.: Application of a differential fuel-cell analyzer for measuring atmospheric oxygen variations, *Journal of Atmospheric and Oceanic Technology*, 24, 82-94, doi:10.1175/JTECH1959.1171, 2007.

## **CHAPTER 3 – THE WEYBOURNE CO<sub>2</sub>, O<sub>2</sub> AND APO RECORDS**

### 3.1 Site description

The Weybourne Atmospheric Observatory is a field station located on the north Norfolk coast in the United Kingdom. It was established in 1992 by the University of East Anglia (UEA) and is used for long-term studies and discrete short-term field campaigns by UEA and a number of other institutions. The precise location is 52.95°N, 1.12°E, situated just outside Weybourne village (population ~500), surrounded by agricultural fields and with the North Sea to the north. This part of Norfolk is predominately agricultural and consists of small villages and coastal towns. The main centre of population in Norfolk, Norwich, is 26 miles south-southeast, with an urban population of about 200,000, just under a quarter of Norfolk's total population.

Air is sampled from aspirated air inlets on a 10 m a.g.l. tower (~20 m a.s.l.) located approximately 50 m from the North Sea coast. The analysis system is housed in an air conditioned concrete building converted from its initial use as a military building and subsequent use as a cow shed. The building, tower and geographic location are shown in Figure 3.1. Continuous measurements of atmospheric O<sub>2</sub> and CO<sub>2</sub> have been made at the station since late 2007 and continue to the present day. Other species routinely measured at WAO include H<sub>2</sub>, CO, O<sub>3</sub>, NO, NO<sub>2</sub> and SO<sub>2</sub>.



Figure 3.1. Google Earth satellite image and map showing the location of the Weybourne Atmospheric Observatory (WAO) in Norfolk, with respect to the rest of the UK, and a photograph, looking north, showing the WAO with the inlet tower and North Sea beyond.

## 3.2 Data analysis methods specific to this chapter

### 3.2.1 Hpspline curve fitting

When studying atmospheric time series it is often useful to fit a smooth curve through the observations in order to subsequently decompose the features of the observed data and attribute the variations to different factors operating on different timescales (Theodosiou, 2011). This process is called time series decomposition. In my thesis, the curve fitting program used is called 'Hpspline'.

Hpspline was first written by the Atmospheric Oxygen Research Group based at the Scripps Institution of Oceanography, San Diego, USA and is a development of the 'Stationfit' program used by the Carbon Dioxide Research Group at the same institution. Version 5 of Hpspline is run in FORTRAN. The computational procedure consists of fitting data to a harmonic function, an  $n^{\text{th}}$  order polynomial equation and a cubic spline (Reinsch, 1967). First the data are fit linearly to the following expression (Keeling et al., 1989):

$$S = \sum_{k=1}^m [\alpha_k \sin(2\pi kt) + b_k \cos(2\pi kt)] \quad (3.1)$$

Where  $S$  is the seasonal variation as represented by a harmonic function,  $m$  is the number of harmonics,  $t$  is the time in years,  $2\pi k$  is the angular frequency, and  $\alpha_k$  and  $b_k$  are constants. The fits on my data were carried out using two harmonics; four harmonics are often used but for the WAO data presented, four harmonic fits appeared to exaggerate small variations in the data and introduced features that were not observed in the raw data. The inter-annual variation, or long-term trend, was set to be linear (in other words a first order polynomial) since the WAO records being fitted were only about 4.5 years in length and thus inter-annual variation in this trend can not be well quantified. This linear trend is represented by the symbol,  $E(t)$  and, in my fits, it is therefore a linear function of time:

$$E(t) = a_0 + a_1 t \quad (3.2)$$

The data are fitted non-linearly to the function  $S + E$  using the initial estimates of the harmonic coefficients from the first fit. The influence of the long-term trend is

removed by subtracting the function E from the data. The complete fit is obtained via a converging iteration of fitting and subtracting the S and spline (R) components (Bacastow et al., 1985) to the data, where S is allowed to vary linearly by a gain factor,  $\gamma$ , until the time series data can be represented as (Keeling et al., 1989):

$$P = E + (1 + \gamma t)S + R \quad (3.3)$$

Where P is equivalent to the sum of the seasonally adjusted concentration and the seasonal variation. In my application, The spline, R, is bypassed and I have not used a gain factor, since over such a short time period (~4.5 years) any variability in the amplitude of the seasonal cycle is likely caused by inter-annual variations rather than owing to a long-term trend in seasonal patterns.

### 3.2.2 Modelled results.

In order to compare my data to that expected for the region based on model predictions of APO fluxes, a number of model simulations were performed by Corinne Le Quéré and Clare Enright. The model used is similar to that reported in Le Quéré et al. (2010) but I focussed on the region local to WAO rather than inferring global implications. Three geographical areas were examined covering an increasingly wide area: the North Sea only (2°W to 8°E and 53°N to 60°N); the wider area, including parts of the Atlantic Ocean (30°W to 10°E and 45°N to 65°N); the circumpolar region at latitudes greater than 45°N. These three geographical areas are shown in figure 3.2 below.

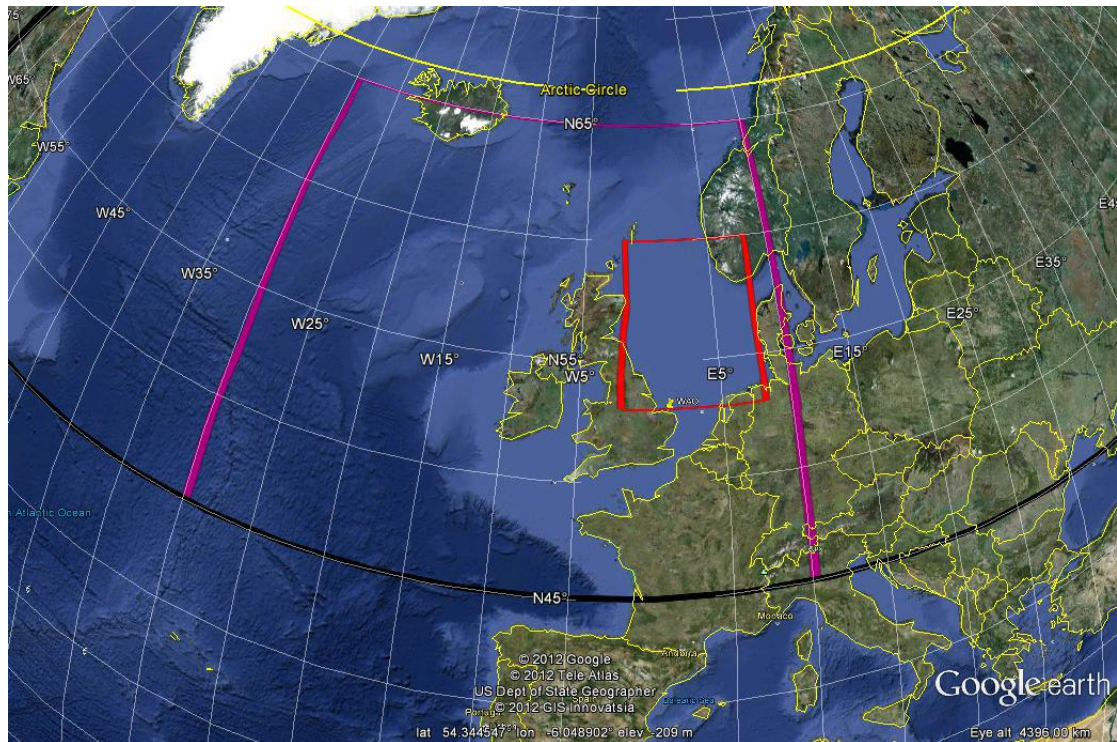


Figure 3.2. The 3 regions used in the model runs. The red box represents the North Sea region (2°W to 8°E and 53°N to 60°N); the purple box represents the wider area, including parts of the Atlantic Ocean (30°W to 10°E and 45°N to 65°N); the final region is everything at latitudes greater than 45°N, that is the region above the black line.

For each of these regions an Ocean General Circulation Model (OGCM) (Madec and Imbard, 1996) was used with horizontal resolution of  $1.5^\circ \times 2^\circ$ , 30 vertical levels, explicit vertical diffusion and parameterised eddy mixing (Le Quéré et al., 2007). The OGCM is coupled to a marine biogeochemistry model (Buitenhuis et al., 2006) with no nutrient restoring. It is then forced by increasing atmospheric  $\text{CO}_2$  concentrations (Keeling et al., 2005) and daily winds and precipitation from the National Center for Environmental Prediction (NCEP) reanalysis (Kalnay et al., 1996). Additional runs were carried out with forcing from satellite wind data developed at the NASA Jet Propulsion laboratory (JPL) (Atlas et al., 2011; Atlas et al., 1996) and finally with forcing from data from the European Centre for Medium-Range Weather Forecasts (ECMWF).

### 3.3 Complete data records

The datasets for atmospheric  $\text{O}_2$  and  $\text{CO}_2$  concentration collected at WAO are presented in figure 3.3, along with the record for Atmospheric Potential Oxygen

(APO), calculated from the O<sub>2</sub> and CO<sub>2</sub> data as discussed in chapter 1. Data points for outside air were collected every 2 minutes, whenever the system is not running a calibration or other high pressure cylinder measurement.

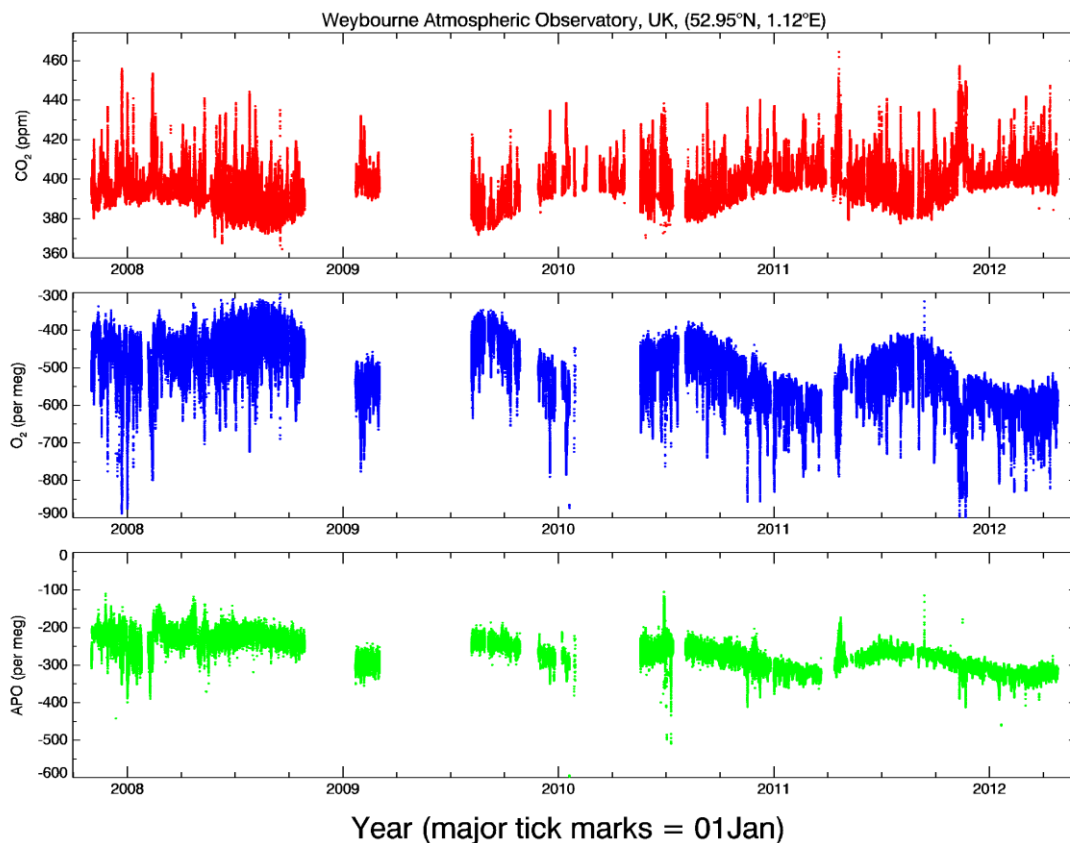


Figure 3.3. CO<sub>2</sub> (red), O<sub>2</sub> (blue) and APO (green) datasets from WAO for the period 1<sup>st</sup> October 2007 to 30<sup>th</sup> April 2012. The major tick marks on the x-axis represent the 1<sup>st</sup> January of the year indicated. Each data point represents a 2 minute period of ambient air data collected by the analysers. The y-axes have been chosen so that variations in all species are visually comparable on a molar basis.

There are three relatively large gaps in the data record. First, from 27<sup>th</sup> October 2008 to 21<sup>st</sup> January 2009, owing to a shortage of calibration standards, calibrated data could not be collected. Second, from 3<sup>rd</sup> March 2009 to 5<sup>th</sup> August 2009, major upgrades were carried out to the system including changing some of the system components, removing extraneous pressure gauges to reduce dead volume, and the implementation of a new and more reliable bespoke software program to control the system, written in C# rather than Visual Basic. There are a number of smaller gaps after this period as smaller maintenance or troubleshooting tasks were carried out related to these upgrades. Finally there is a large gap in O<sub>2</sub> and APO from the 31<sup>st</sup> January 2010 to 19<sup>th</sup> May 2010, initially caused by an unknown

problem with the Oxzilla analyser that could not be solved after a lot of troubleshooting including updating the Oxzilla firmware and replacing the fuel cells. Eventually the Oxzilla analyser itself had to be replaced. Toward the end of this period there was also a shortage of calibration standards, necessitating an entire system shutdown from the 22<sup>nd</sup> April to the 19<sup>th</sup> May 2010.

The 2 minute data consist of over half a million data points for each species. In order to reduce this number and make the datasets more manageable, it was necessary to average the data over different time periods. Thus, all of the 2 minute data points for a given hour were averaged to produce a single value. The same procedure was also used to provide daily, weekly and monthly averages. The hourly averaged datasets are presented in figure 3.4 and the daily averaged datasets are presented in figure 3.5.

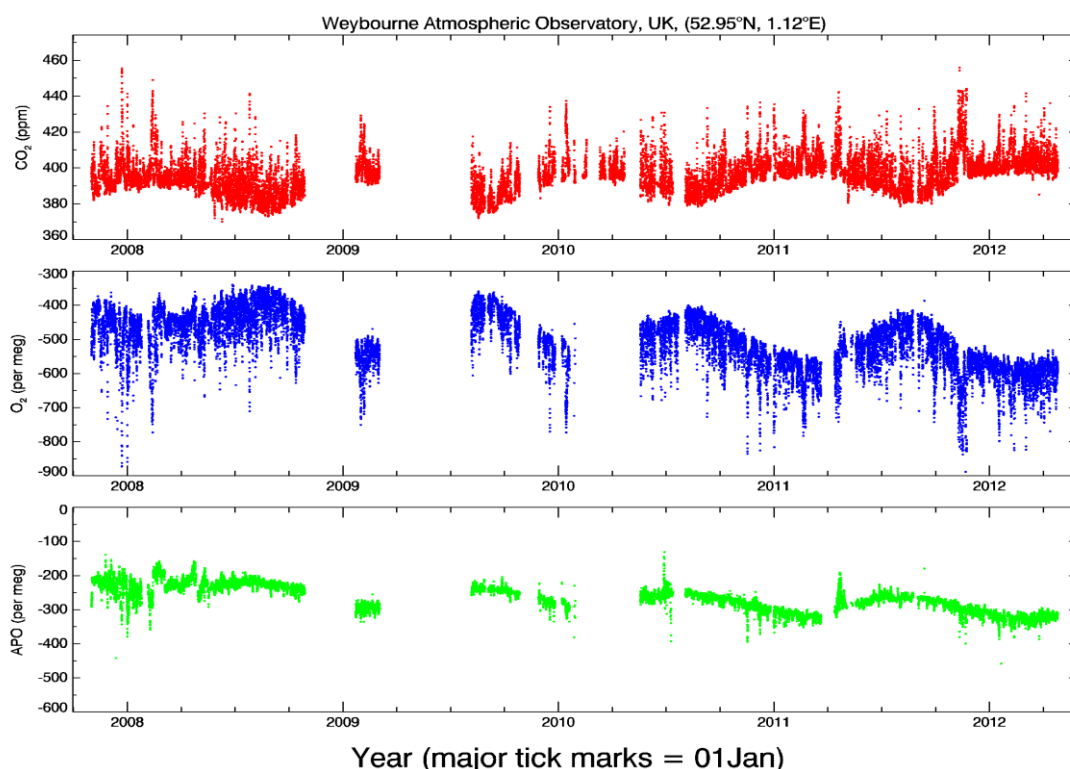


Figure 3.4. CO<sub>2</sub> (red), O<sub>2</sub> (blue) and APO (green) datasets from WAO for the period 1<sup>st</sup> October 2007 to 30<sup>th</sup> April 2012. The major tick marks on the x-axis represent the 1<sup>st</sup> January of the year indicated. Each data point represents the mean of all 2 minute data points over a 1 hour time period. As in Figure 3.3, y-axis ranges have been chosen so that variations are visually comparable on a molar basis for CO<sub>2</sub>, O<sub>2</sub> and APO.

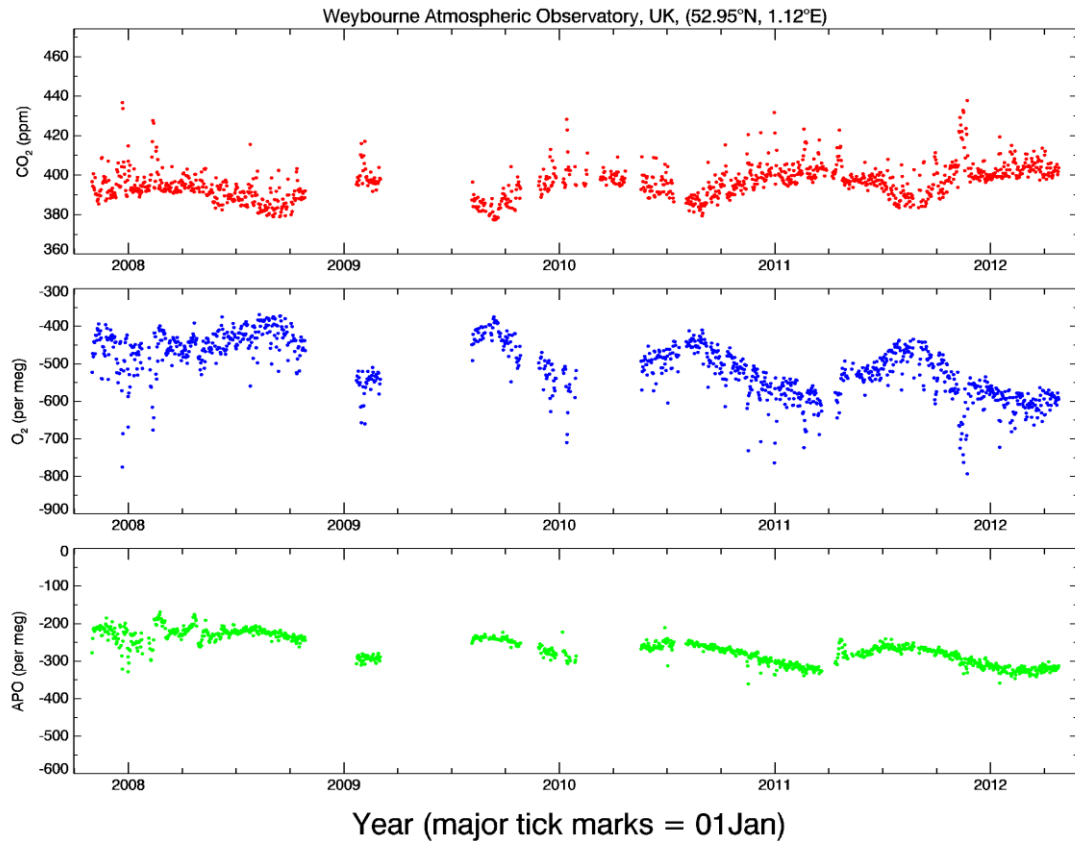


Figure 3.5. CO<sub>2</sub> (red), O<sub>2</sub> (blue) and APO (green) datasets from WAO for the period 1<sup>st</sup> October 2007 to 30<sup>th</sup> April 2012. The major tick marks on the x-axis represent the 1<sup>st</sup> January of the year indicated. Each data point represents the mean of all 2 minute data points over a calendar day. As in Figure 3.3, y-axis ranges have been chosen so that variations are visually comparable on a molar basis for all three species.

From these plots of the 4.5 year data sets I can make a number of qualitative observations before examining them in more detail, and in a more quantitative manner in the following sections.

CO<sub>2</sub> shows the expected seasonality with the highest values for a given twelve month period occurring during the months of January, February and March. This corresponds to late winter in the northern hemisphere when deciduous trees have dropped their leaves and respiration is dominant over photosynthesis, leading to a net build-up of CO<sub>2</sub> in the atmosphere. The opposite is true for the CO<sub>2</sub> minima, which are observed in the months of July August and September, mid to late summer in the northern hemisphere. During this time photosynthesis is dominant over respiration and so this period is relatively CO<sub>2</sub> depleted in the atmosphere. This is not the only contributing factor to the observed seasonality. The

temperature cycle throughout the year has a role to play in the relative rates of photosynthesis and respiration in addition to the availability of light and the amount of vegetation already discussed. Respiration is strongly temperature dependent and increases with temperature, photosynthesis is more complicated and slows at extremely high and low temperatures but has an optimum temperature depending on the plant type. In general the increase in rate of photosynthesis due to temperature increases in the late summer months are not as great as the increases in respiration but this effect is outweighed by the increase in respiration due to longer day length and increased vegetation.

For  $O_2$ , the opposite seasonality exhibited by  $CO_2$  is broadly expected owing to the interdependence of the two species in the processes of photosynthesis and respiration (in terrestrial biota). This is indeed observed at WAO, where the maxima for  $O_2$  are observed in July and August and the minima over the months of December to March. A further influence on the seasonality observed in atmospheric  $O_2$  comes from the temperature dependent solubility of  $O_2$ .  $O_2$  is less soluble in warmer waters and so as the ocean warms up in late summer, lagging slightly behind atmospheric temperatures,  $O_2$  outgasses from the oceans and increases the atmospheric concentration. This effect is smaller than that due to increased photosynthesis but is in phase and so enhances the seasonal cycle.

It is also important to consider the effect that the seasonal cycle in atmospheric boundary layer (ABL) height has on the concentrations of species in the atmosphere, particularly for a sight such as Weybourne which is sampling from within the ABL. The ABL varies with temperature and turbulence above the surface of the Earth and so tends to be higher, or thicker, in the warmer summer time than it is in winter. This has the effect of diluting the apparent concentration of species within the boundary layer at a given time when it is high, or thick, during the warmer months and increasing the apparent concentrations of species in the cooler months when the boundary layer is thinner. For  $CO_2$  this is in phase with the observed seasonality caused by photosynthesis rates and so it reinforces the seasonal cycle for  $CO_2$ , for  $O_2$  the opposite is true, the boundary layer effect on the seasonal cycle is out of phase and so this serves to reduce the apparent amplitude

of the seasonal cycle. The seasonal rectifier effect is important to consider but is less pronounced than the diurnal rectifier effect that is a key driver of diurnal cycles and is discussed in chapter 4.

In the APO signal,  $O_2$  appears to have the greater influence since the APO seasonality follows a similar pattern as  $O_2$ , reaching maxima in July to September and minima in February/March. The APO signal is conservative with respect to the terrestrial biosphere and so the seasonality observed is mainly due to seasonal oceanic processes such as outgassing in the warmer summer months. This also explains why the variations in APO over the course of a year are much smaller than for  $O_2$  or  $CO_2$  as can be seen in the plots due to their comparable y-axis ranges. The amplitude of the seasonal variation is much smaller for APO than for  $O_2$  or  $CO_2$  and this will be explored quantitatively later in this chapter. It is important to remember that the factor used to calculate APO removes natural terrestrial processes but does not remove the influence from combustion processes such as fossil fuel burning. In general, the combustion processes consume more molecules of  $O_2$  for each molecule of  $CO_2$  produced and so when fossil fuel burning is highest, this is seen as a reduction in APO. For this reason, any seasonality in fossil fuel burning will be reflected accordingly in the APO seasonal cycle.

Over the course of more than four years of measurements we can also see that the long-term trend in  $CO_2$  is increasing concentrations, whereas  $O_2$  and APO exhibit decreasing long-term trends. This is expected from the ongoing burning of fossil fuels, whereby  $CO_2$  is produced and  $O_2$  is consumed. I will look at the magnitude of these long-term changes observed at WAO in the following sections.

Aside from these longer timescale, general observations, it can also be seen, especially from figure 3.3 above, that there is a lot of shorter timescale variation in the species measured at WAO. These shorter term variations may be attributed to a number of different causes and will be explored in detail in chapter 4.

### 3.4 Curve fitting details and results

The curve fitting program, Hpspline, was run for CO<sub>2</sub>, O<sub>2</sub> and APO as described earlier in this chapter. The resulting curve fits for the three species along with the hourly averaged data are shown in figure 3.6. When calculating the curve fits, they were fitted to data from 2009 to 2012 only. The earlier portion of the data record, from October 2007 to October 2008, has a number of problems associated with it that compromise the accuracy of these data. These problems include calibration issues, for example, owing to a scarcity of calibration standards available, standards had to be sourced from different external laboratories and there is a question over the compatibility of the calibration scales of these different standards. There were also logistical and analytical ‘teething’ problems in setting up these new measurements at the WAO. It is hoped that the majority of these data will be recoverable by careful reanalysis of the old calibration cylinders. But unfortunately, this work could not be completed within the time frame of my thesis, owing to external factors beyond my control such as availability of calibration standard reanalysis at the Scripps Institution of Oceanography.

I did calculate curve fits for the entire 2007 – 2012 data records, and found significant differences compared to those shown in figure 3.6, whereby the curve fit did not fit the later part of the record well. In particular, the seasonal cycle amplitude appeared to be artificially too large, most likely owing to the ‘noisier’ appearance of the 2007 – 2008 data. Using the fit for 2009 – 2012 data, however, and extrapolating back to the early period as shown in figure 3.6, appears to visually fit all data quite well, providing further confidence in this methodology I have chosen. Figure 3.6 shows the curve fits together with hourly averaged data, fits were performed on the 2-minute and daily averages with very similar results.

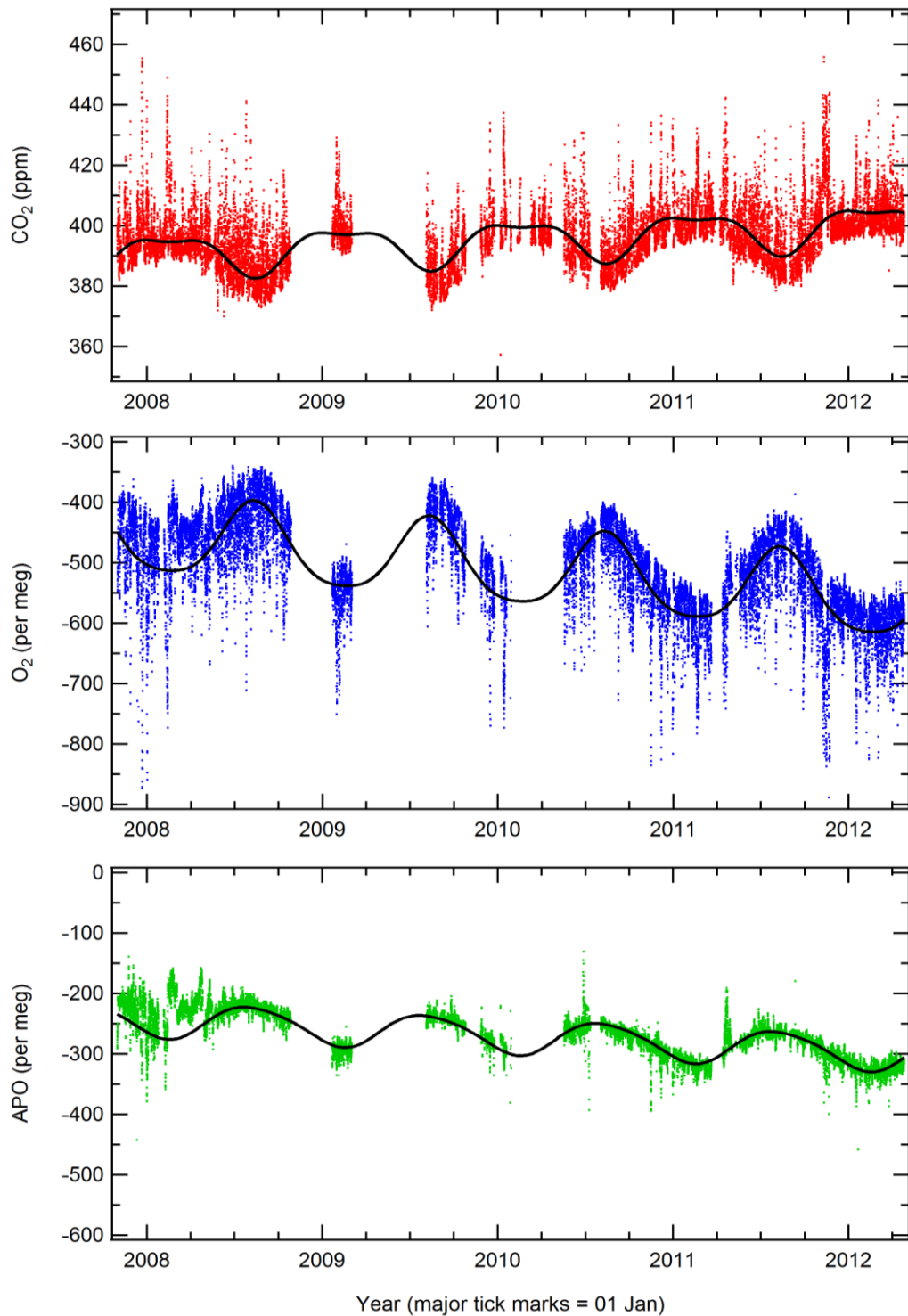


Figure 3.6. Curve fits from Hpspline for CO<sub>2</sub> (red), O<sub>2</sub> (blue) and APO (green). Each curve fit incorporates two harmonics to represent the seasonal cycle and a linear growth rate. Each fit is based on hourly averaged data from 2009 to 2012 only and extrapolated backwards to cover the entire record. Calibration scale issues and other problems with the early portion of data in 2007 and 2008 impacted erroneously upon the curve fits when the fits were applied over the entire data records. The y-axis ranges chosen are visually comparable on a molar basis.

The curve fit for CO<sub>2</sub> shows a broad winter period of elevated concentrations with a double maximum feature. This double feature may not be robust from the relatively short period of measurements used for the curve fit, it is likely this is just a broad and quite flat maximum. In summer the minimum is relatively short. O<sub>2</sub> shows a broad winter minimum and short summer maximum, as may be expected owing to the interconnection of O<sub>2</sub> and CO<sub>2</sub> in the processes of terrestrial photosynthesis and respiration. The O<sub>2</sub> winter minimum is not as broad as the corresponding maximum observed in CO<sub>2</sub> and lags behind it, reaching a minimum after the CO<sub>2</sub> maximum. The cause of this is that the oceanic processes which are contributing to the minimum observed in O<sub>2</sub> do not occur as quickly as the terrestrial die back and increased respiration that is responsible for the maximum in the CO<sub>2</sub> signal. APO shows a smaller seasonal amplitude and has a more even distribution or symmetry between maxima and minima.

The most striking observation from the curve fits is that the data collected at Weybourne are often not a representation of background concentrations but are influenced by other factors. The background signal would be expected to generally follow the lower values of CO<sub>2</sub> concentration, with the opposite true for O<sub>2</sub> and APO; that is, background signals would follow the higher concentrations. For the curve fits shown in figure 3.6, they pass through the data approximately in the middle range of values, showing that polluted air is often observed at Weybourne and that this has influenced the curve fits. A sophisticated data selection methodology would be required to attempt to extract background signals from these data records. Manning et al. (2011) describe such a sophisticated baseline data selection methodology, applied to Mace Head, Ireland atmospheric data, and employing the UK Met Office Lagrangian NAME model operating in backwards mode. In future, it is anticipated to develop similar methodologies for our Weybourne data sets.

I do see the expected natural seasonality in all species and so despite the presence of significant periods of polluted air, it is still possible to examine in more detail the longer-term features such as the seasonality and annual growth rates.

### 3.4.1 Long-term trends

As mentioned above, because of the brevity of the records, my curve fits forced fixed, linear long-term trends, shown quantitatively in table 3.1. As the records are extended into the future, observations such as year on year changes in growth rate will be possible. Table 3.1 shows the calculated linear trends for each species and for each averaging period of the data points.

Data averaging period	Long-term trend of CO <sub>2</sub> (ppm yr <sup>-1</sup> )	Long-term trend of O <sub>2</sub> (per meg yr <sup>-1</sup> )	Long-term trend of APO (per meg yr <sup>-1</sup> )
2 minutes	2.43 ± 0.01	-25.4 ± 0.1	-13.4 ± 0.1
Hourly	2.41 ± 0.07	-25.3 ± 0.4	-13.4 ± 0.1
Daily	2.55 ± 0.26	-26.3 ± 1.7	-13.5 ± 0.5
Weekly	2.62 ± 0.43	-26.7 ± 2.7	-13.5 ± 0.8
Monthly	2.34 ± 0.54	-23.9 ± 3.6	-12.3 ± 1.4

Table 3.1. Summary of long-term trends for CO<sub>2</sub>, O<sub>2</sub> and APO from WAO. The trends are calculated from the curve fitting results using Hpspline with a linear trend prescribed. Fits were computed on data sets for each species averaged over different time frames using data collected between January 2009 and April 2012.

The resulting trends for the different data averaging periods all agree well with one another. The results using the monthly averaged data points all show growth rates of slightly smaller magnitude. Due to gaps in the data record in 2009 and 2010, these curve fits were calculated with just 32 points and with a large gap in the first half of 2009 (see figure 3.5). Thus, any slightly anomalous monthly value would have a relatively large influence on the overall fit and this may help explain the slight difference seen for these monthly-averaged fits.

The long term trend results from Weybourne can be compared to those published for other stations at similar latitudes. The results are compared to: the Polish tall tower at Białystok (53.22°N, 23.02°E) in the period 2005 - 2008 (Popa et al., 2010); Lutjewad station (53.4°N, 6.35°E) in the Netherlands between 2000 - 2009 (van der Laan-Luijkx et al., 2010); Mace Head (53.33°N, 9.9°E), on the west coast of

Ireland between 1998 - 2009 (van der Laan-Luijkx et al., 2010); the F3 oil platform (54.85°N, 4.73°E) in the North Sea between 2006 - 2009 (van der Laan-Luijkx et al., 2010); Ochsenkopf (50.03°N, 11.8°E) between 2006 - 2008 (Thompson et al., 2009); the Shetland Islands (60.28°N, 1.28°W) between 2004 - 2008 (Kozlova et al., 2008). The positions of these stations are shown in figure 3.7 below and the results from the stations are summarised in table 3.2.

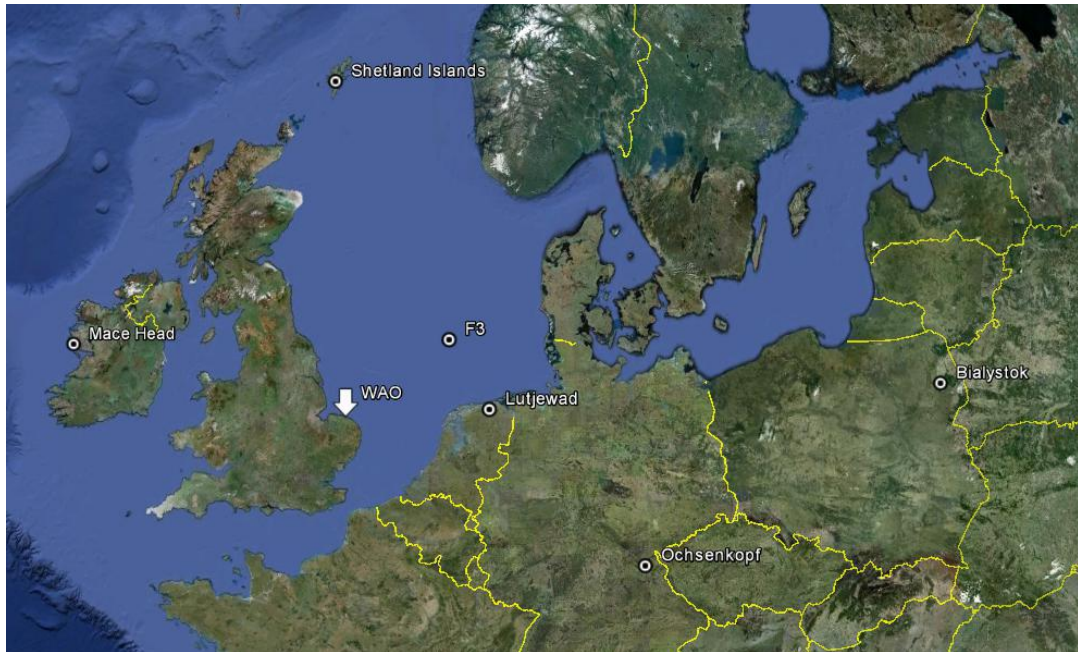


Figure 3.7. Map showing the positions of the atmospheric observation stations used in the comparison with WAO results in table 3.3. At 1020 m a.s.l. Ochsenkopf is the only station that samples from above the A.B.L. for a significant portion of time.

Station	Mace Head	Shetland Islands	WAO	F3 Oil Platform	Lutjewad	Ochsenkopf	Bialystok
Location	53.33°N 9.9°E	60.28°N 1.28°W	52.95°N 1.12°E	54.85°N 4.73°E	53.4°N 6.35°E	50.03°N 11.8°E	53.22°N 23.02°E
Period	1998 - 2009	2004 - 2008	2009 - 2012	2006 - 2009	2000 - 2009	2006 - 2008	2005 - 2008
CO <sub>2</sub> long term trend / ppm	1.90 ± 0.04	2.2	2.41 ± 0.07	2.11 ± 0.04	1.97 ± 0.07	1.60 ± 0.47	2.02 ± 0.46
O <sub>2</sub> long term trend / per meg	-18.5 ± 0.7	-19	-25.3 ± 0.4	-27 ± 0.6	-21.0 ± 0.9	-16.3 ± 3.1	-23.2 ± 2.5
APO long term trend / per meg	-8.4 ± 0.7	-7.2	-13.4 ± 0.1	-13 ± 0.5	-10.6 ± 0.7	-9.7 ± 1.5	NA

Table 3.2. Summary table comparing the long-term trends for CO<sub>2</sub>, O<sub>2</sub> and APO from WAO with other European atmospheric observatories at similar latitudes. Curve fits to hourly averaged values for the WAO data were used.

Atmospheric CO<sub>2</sub> concentration at WAO was observed to grow by 2.41 ppm yr<sup>-1</sup>. Given that fossil fuel emissions continue to rise each year (Peters et al., 2012), this increase is in line with other published observations at similar latitudes. All of these other stations show similar, but slightly lower values for the long-term CO<sub>2</sub> trend than I found at WAO. This is not unexpected as the WAO data is more recent than the other stations. In contrast to the WAO data, the data records of the other stations all include at least some of the period of the 2008 – 2009 global economic crisis when fossil fuel emissions were lower. A rebound in emissions in 2010 (Peters et al., 2012) followed this and these are captured by the WAO data. The decline of the global economy began in December 2007 with a sharp downward turn in September 2008 and the recession continued throughout 2009, by 2010 some major economies were starting to recover; the economic crisis lasted for the entireties of the years 2008 and 2009.

Atmospheric O<sub>2</sub> was observed to decrease by 25.3 per meg yr<sup>-1</sup>, again in line with observations at other European stations in table 3.3. With the exception of the F3 oil platform, the atmospheric O<sub>2</sub> decrease at WAO is larger than that of these other

stations. This can also be expected based on the WAO trend being calculated over a more recent period and the global changes in fossil fuel emissions. There have been some difficulties establishing the atmospheric O<sub>2</sub> calibration scale at the F3 oil platform, which may explain the slightly larger decreasing trend observed at this station.

APO showed an annual decrease at WAO of 13.4 - 13.5 per meg, also in line with other observations presented in table 3.3.

An attempt was made to study changes in the annual growth rate for each species over the period 2009 – 2012. As mentioned in the opening paragraph of this section, it is difficult to study interannual variability with such a short data record and this is why the long-term trend was set as linear for the purposes of the curve fits. Nevertheless, I believe it may be insightful to provide a preliminary examination of annual growth rates at this stage. These annual growth rates are calculated from consecutive averages of the data over a 12 month period subtracted from each other. The 12 month averages are calculated every 6 months so, for example, the point plotted in figure 3.8 for 2009.75 is calculated by subtracting the annual average centred on 2010.0 from that centred on 2009.5. Since the annual average centred on 2010.0 incorporates data from 2009.5 to 2010.5, and the average centred on 2009.5 incorporates data from 2009.0 to 2010.0, there is an overlap in the period between 2009.5 and 2010.0. Therefore the growth rate value centred on 2009.75 effectively gives you half the value of subtracting the six month average of 2010.0-2010.5 from the six month average of 2009.0-2009.5. Smoothed plots of how the annual growth rate has changed at WAO are shown in figures 3.8, 3.9 and 3.10 for CO<sub>2</sub>, O<sub>2</sub> and APO, respectively.

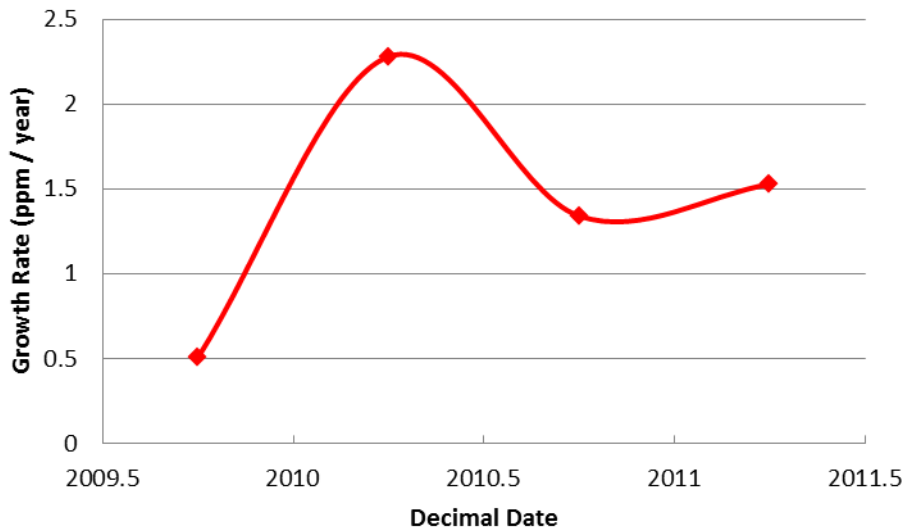


Figure 3.8. CO<sub>2</sub> annual growth rates calculated from annual averages determined every six months. For example, the growth rate of 0.5 ppm / year in 2009.75 is calculated by subtracting the annual average centred on 2010.0 from that centred on 2009.5.

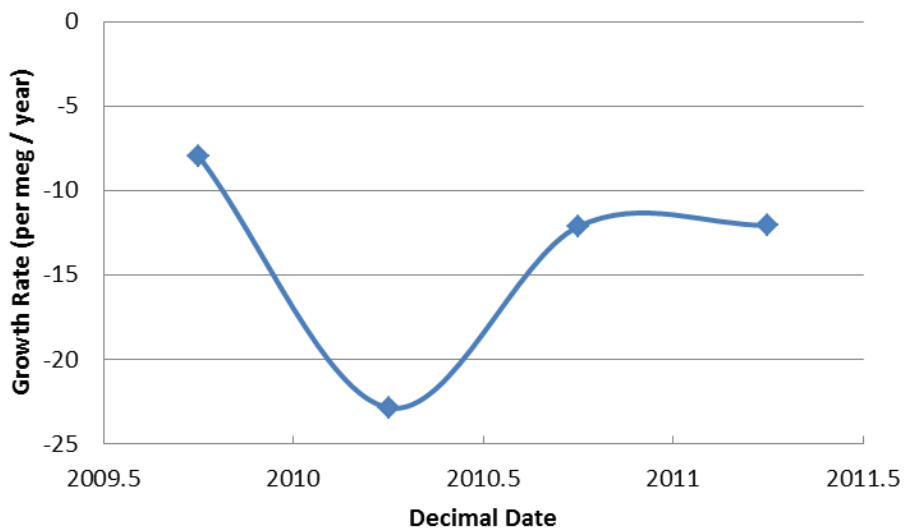


Figure 3.9. O<sub>2</sub> annual growth rates calculated from annual averages determined every six months, calculated similarly as in Figure 3.7 above.

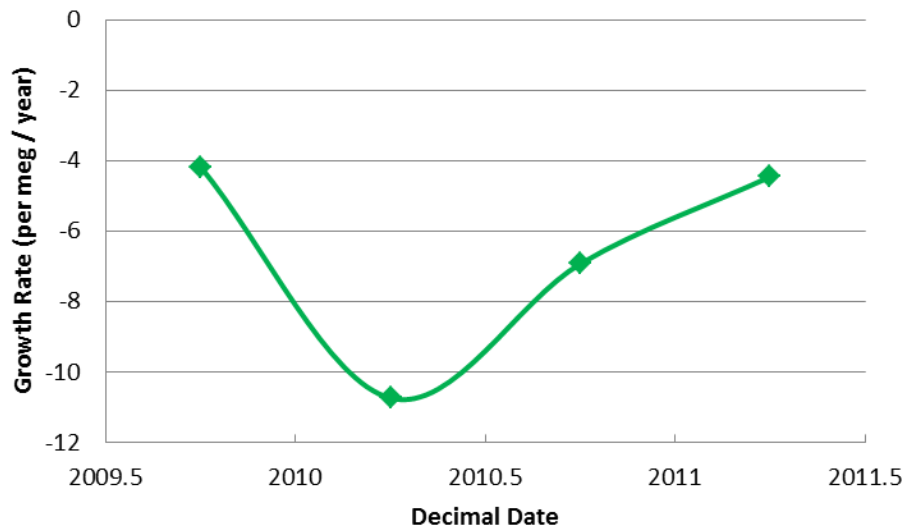


Figure 3.10. APO annual growth rates calculated from annual averages determined every six months, calculated similarly as in Figure 3.7 above.

From figures 3.8, 3.9 and 3.10, it appears that the highest magnitude growth rates for all species were centred on 2010.25 (that is, effectively, half of 2010.5-2011 minus 2009.5-2010). It has been argued that the world gross domestic product (GDP) is a key driver in contemporary increases in anthropogenic CO<sub>2</sub> emissions and fossil fuel burning (Raupach et al., 2007). It has been clearly documented that the global financial crisis of 2008 – 2009 had a measurable effect on global CO<sub>2</sub> emissions and this has been used to explain the slow down in the average growth rate in CO<sub>2</sub> emissions from 3.7% per year for the period 2000 – 2007 to 2.0% per year for the period from 2007 – 2009 (Le Quéré et al., 2009). Taking a less global view, I can tentatively compare the pattern seen in the growth rates observed at WAO with the figures for the UK CO<sub>2</sub> emissions for the same period, presented in figure 3.11.

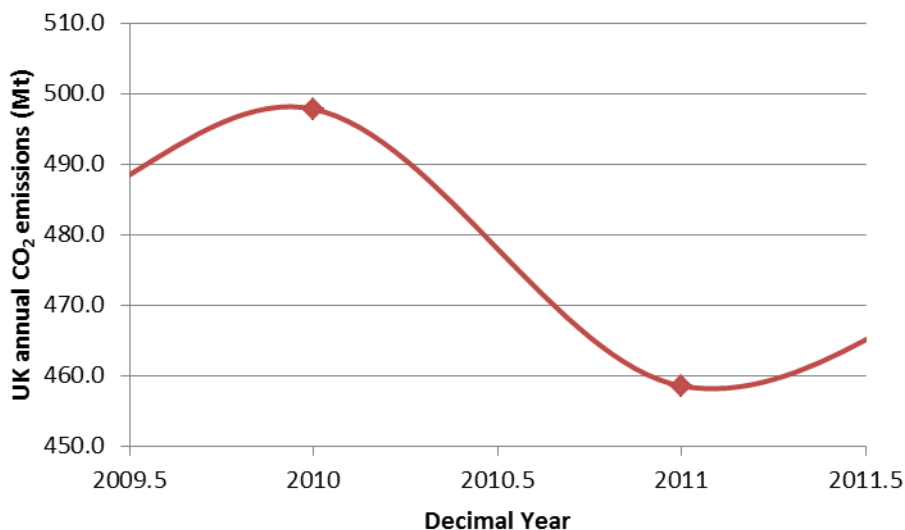


Figure 3.11. Plot of UK annual CO<sub>2</sub> emissions from fossil fuel burning. The data for the years 2007 to 2012 were plotted and a smoothed curve fitted. The time period shown is chosen to match that shown in figures 3.8 – 3.10 above. Data were taken from the UK Department of Energy and Climate Change.

While it is extremely hard to draw firm comparisons from such a short time period with so few data points, it can be seen that for the period in question the CO<sub>2</sub> measurements made at Weybourne broadly follow the trends seen in UK CO<sub>2</sub> emissions from fossil fuel burning. The limited temporal range of data is not the only reason to treat comparisons with some caution. Figure 3.11 only shows UK CO<sub>2</sub> emissions from fossil fuel burning and the air sampled at Weybourne has influences from a number of different regions, including significant contributions from continental Europe, as will be explored in chapter 4. Also fossil fuel emissions are not the only driver of inter annual variability in CO<sub>2</sub>, O<sub>2</sub> and APO; terrestrial and oceanic processes must also be considered to understand the picture fully. As the WAO data record extends into the future, and also if data from the early 2007 – 2008 part of the WAO data record can be recovered when the calibration scale issues are resolved then it may be possible to explore this analysis further and draw firm conclusions.

### 3.4.2 Examination of seasonal cycle

The seasonal cycles of CO<sub>2</sub>, O<sub>2</sub> and APO measured at WAO can be examined by studying the detrended curve fits of the data. That is, the components of the curve

fit with the linear long-term trend removed. Seasonal amplitudes were calculated by subtracting the seasonal minimum from the seasonal maximum concentration for each 12 month period of data. 12 month periods of data were taken every 6 months throughout the data record and the resulting seasonal amplitudes are presented in table 3.2, along with averages for the entire data record.

Midpoint of 12 month period	CO <sub>2</sub> seasonal amplitude (ppm)	O <sub>2</sub> seasonal amplitude (per meg)	APO seasonal amplitude (per meg)
2009.5	17.9	155.3	66.2
2010	15.7	145.9	58.9
2010.5	13.5	121.3	52.1
2011	13.6	122.6	57.3
2011.5	13.9	126.1	60.5
<b>Average</b>	<b>14.9 ± 0.8</b>	<b>134.2 ± 7.8</b>	<b>59.0 ± 5.6</b>

Table 3.3. Seasonal amplitudes observed at WAO for CO<sub>2</sub>, O<sub>2</sub> and APO. Seasonal amplitudes were calculated by subtracting the seasonal minimum from the seasonal maximum concentration for a 12 month period of data and this was repeated every 6 months.

The average seasonal amplitudes observed at WAO for the 3 species were then compared to those reported for other European observation stations at similar northern hemisphere latitudes. The results are summarised in table 3.4:

Station	Mace Head	Shetland Islands	WAO	F3 Oil Platform	Lutjewad	Ochsenkopf
Location	53.33°N 9.9°E	60.28°N 1.28°W	52.95°N 1.12°E	54.85°N 4.73°E	53.4°N 6.35°E	50.03°N 11.8°E
Period	1998 - 2009	2004 - 2008	2009 - 2012	2006 - 2009	2000 - 2009	2006 - 2008
CO <sub>2</sub> amplitude / ppm	14.0 ± 0.3	15.4	14.9 ± 0.8	15.2 ± 0.1	12.0 ± 0.6	15.46 ± 1.04
O <sub>2</sub> amplitude / per meg	142 ± 6	163	134.2 ± 7.8	144 ± 2	114 ± 8	134.6 ± 6.8
APO amplitude / per meg	74 ± 6	95	59.0 ± 5.6	111 ± 2	64 ± 6	43.1 ± 3.3

Table 3.4. Summary table comparing the seasonal amplitudes for CO<sub>2</sub>, O<sub>2</sub> and APO observed at Weybourne Atmospheric Observatory with other European atmospheric observatories at similar latitudes.

The average seasonal amplitude in CO<sub>2</sub> observed at WAO of 14.9 ppm is similar to values published for other stations at similar northern hemisphere latitudes. The WAO record used for this analysis begins in 2009 and so only has minimal overlap with some of the records under comparison here. It has been suggested that changes in the terrestrial biosphere of the northern hemisphere are leading to increasing amplitude in the CO<sub>2</sub> seasonal cycle (Piao et al., 2008; Keeling et al., 1996), for this reason some caution must be taken when comparing figures from records covering different periods. However the annual increase is likely to be around 1% of the amplitude and the records being compared here are suitably close together for this not to greatly influence the comparisons made.

Higher seasonal amplitudes are reported for Bialystok (53.22°N, 23.02°E), 25 ppm, (Popa et al., 2010) and another tall tower in Siberia (ZOTTO; 60.8 °N, 89.35 °E), 26.6 ppm, (Kozlova et al., 2008). These two sites are both continental sites and so are expected to show much higher seasonal amplitudes in CO<sub>2</sub> owing to the influence of the surrounding terrestrial biosphere with a much higher summertime uptake of CO<sub>2</sub> with corresponding CO<sub>2</sub> release in winter.

It is worth noting that northern hemisphere amplitudes are much greater than southern hemisphere amplitudes and those found in the mid-latitudes. For

example Cape Grim, Australia has a seasonal amplitude of 1.2 ppm and Mauna Loa, Hawaii has an amplitude of 7 ppm. The reason for these differences is that these latitudes have much less land mass and therefore a far smaller terrestrial biosphere that is responsible for driving almost all of the seasonality in CO<sub>2</sub>.

Seasonal amplitudes for O<sub>2</sub> and APO are generally more variable between stations than for CO<sub>2</sub>. O<sub>2</sub> amplitudes may be influenced by surrounding terrestrial biosphere in a similar manner as for CO<sub>2</sub>. However O<sub>2</sub> and APO can also be influenced relatively rapidly by fluxes into and out of the oceans. The solubility of O<sub>2</sub> varies as a function of ocean temperature and so seasonal variation in temperatures can play a role in observed O<sub>2</sub> and APO seasonal cycles. In contrast, CO<sub>2</sub> exchange between the atmosphere and oceans occurs on a much slower timescale due to the carbonate reactions that CO<sub>2</sub> undergoes when it is dissolved (see Chapter 1). This has the effect of significantly reducing the seasonality as CO<sub>2</sub> exchange is spread out over the year.

The average O<sub>2</sub> seasonal amplitude at WAO is slightly lower than stations that more closely represent oceanic processes and sample mainly marine air sectors such as Mace Head, the F3 oil platform in the North Sea (van der Laan-Luijkx et al., 2010) and the Shetland Islands (Kozlova et al., 2008). This is indicative of the fact that WAO sees more terrestrially influenced and polluted air and it is more similar to Lutjewad and Ochsenkopf (Thompson et al., 2009).

It is worth noting that in general the seasonal amplitude of O<sub>2</sub> at WAO is just greater than twice the amplitude of that of APO at WAO. Since APO reflects oceanic processes this indicates that approximately half the of the O<sub>2</sub> seasonal cycle is due to oceanic processes and approximately half to terrestrial processes, but the slight imbalance suggests that terrestrial processes are slightly dominant. The time periods with most deviation from this approximation of equal terrestrial and oceanic influence are those centred on 2009.5 and 2010. For these periods APO contributes significantly less than half of the O<sub>2</sub> amplitude while the CO<sub>2</sub> amplitude is larger than for other 12 month periods. This suggests that terrestrial processes are the chief driver of interannual variation observed at WAO for O<sub>2</sub> seasonal amplitudes in these periods. This is a good indication of the signals seen at WAO

but is a slight over simplification; APO changes also reflect fossil fuel combustion as well as oceanic processes, and the seasonal rectifier effect should be considered, this serves to decrease apparent concentrations in the summer months when the ABL height is generally higher than in winter. This enhances the apparent seasonality in CO<sub>2</sub> and reduces that for APO.

The picture is very similar for APO. The WAO average compares well to Lutjewad (van der Laan-Luijkx et al., 2010) and to some extent Ochsenkopf (Thompson et al., 2009). Ochsenkopf is somewhat lower reflecting the more continental nature of the station, APO is indicative of oceanic processes so although the seasonality is lower at WAO than for sites that almost exclusively sample marine air it still sees some marine air and so has a higher seasonal amplitude than Ochsenkopf. The marine sampling sites have markedly higher APO seasonal cycles at Mace Head, at the F3 oil platform (van der Laan-Luijkx et al., 2010) and at the Shetland Islands (Kozlova et al., 2008).

While it is hard to draw firm conclusions on the trend of the seasonal cycle for a data set as short as this it is interesting to make some early observations that could be revisited when more data exists. The amplitude of the seasonal cycles, calculated every 6 months, that are presented in table 3.3 are plotted in figure 3.12 with smoothed curves through them.

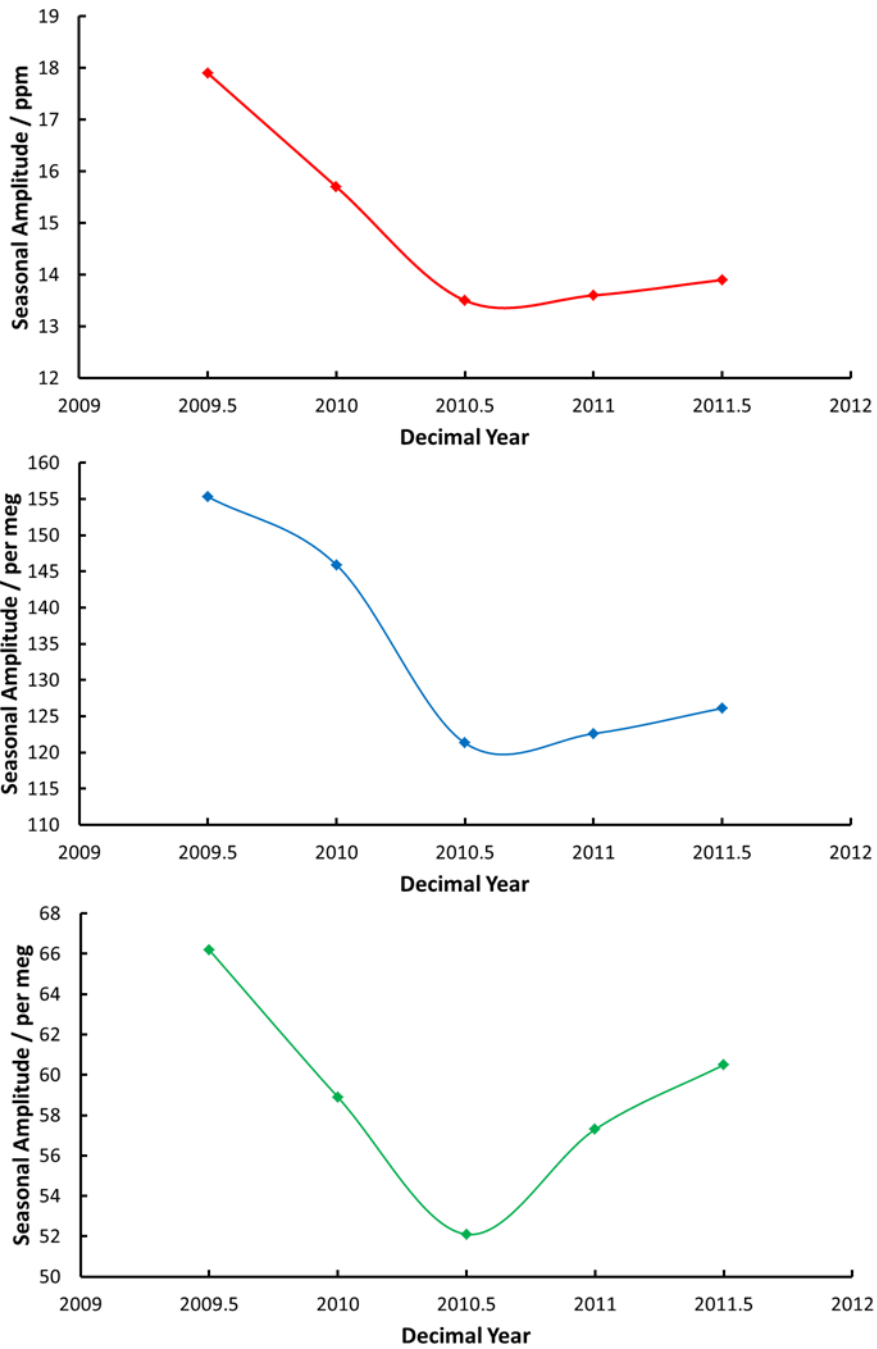


Figure 3.12. Seasonal cycle amplitudes calculated for a 12 month period every 6 months for CO<sub>2</sub> (red), O<sub>2</sub> (blue) and APO (green). Data are taken from table 3.3 and data points are plotted on the date corresponding to the midpoint of the 12 month period.

The plots in figure 3.12 for CO<sub>2</sub> and O<sub>2</sub> are very similar, demonstrating that the stoichiometric interconnectivity between the two species is the dominant process that gives rise to their seasonality. Overall seasonal amplitudes for all three species show a decrease to a minimum for the 12 month period centred on 2010.5 and after this date there is a slower increase. The higher amplitudes could be the result

of the fossil fuel signal observed at WAO. Increased pollution could reinforce natural processes causing increased seasonality and lead to a greater observed seasonal amplitude. Terrestrial processes and pollution influences will be most clearly seen in the CO<sub>2</sub> plot; the O<sub>2</sub> plot incorporates variations in both oceanic and terrestrial processes, with roughly equal magnitudes, and therefore it is not straightforward to attribute O<sub>2</sub> variability to either ocean or terrestrial influences.. It has been suggested that changes in the terrestrial biosphere of the northern hemisphere are leading to an increasing amplitude in the CO<sub>2</sub> seasonal cycle (Piao et al., 2008). It is, however, too early to suggest that the WAO results support the Piao et al. (2008) study, but this should be studied further with a longer data record.

APO shows variations in oceanic processes more clearly as it is conservative with respect to terrestrial processes. From the y-axis scale one can see that variations in APO and oceanic processes are much smaller than for the terrestrial processes that dominate CO<sub>2</sub> and O<sub>2</sub>. However fossil fuel combustion signals are still observed in APO and this could explain why a minimum in the APO seasonal cycle is also observed centred on 2010.5, the same as is seen for CO<sub>2</sub> and O<sub>2</sub>.

Table 3.5 summarises the zero crossing days observed at WAO for the period of study. A zero crossing day is defined as the date at which the detrended curve crosses the x-axis either from positive to negative in the case of down-crossing days or from negative to positive in the case of up-crossing days. For CO<sub>2</sub> the up-crossing day is observed in autumn as CO<sub>2</sub> rises to a winter maximum while the down-crossing day is observed in spring. The opposite is true for O<sub>2</sub> and APO due to the anti-correlation of their seasonal cycles with respect to CO<sub>2</sub>, so the down-crossing day is observed in autumn and the up-crossing day in spring.

Season	CO <sub>2</sub>	O <sub>2</sub>	APO
Autumn	25 <sup>th</sup> Oct	1 <sup>st</sup> Nov	13 <sup>th</sup> Nov
Spring	31 <sup>st</sup> May	21 <sup>st</sup> May	3 <sup>rd</sup> May

Table 3.5. Summary of zero crossing days observed at WAO for CO<sub>2</sub>, O<sub>2</sub> and APO for the curve fit based on data covering the period 2009 – 2012.

These data bear out the visual analysis of the curve fits at the beginning of this chapter. CO<sub>2</sub> has a long period of elevated concentration over winter, in excess of 7 months. O<sub>2</sub> has a winter period of lower concentrations of nearly 7 months. APO has a winter period of lower concentrations of approximately 5.5 months.

### 3.5 Comparison with model-predicted seasonality

The model simulations detailed in section 3.2.2 were performed on the three geographical areas shown in figure 3.2. The three geographical areas examined are: the North Sea only (2°W to 8°E and 53°N to 60°N); a wider area, including parts of the Atlantic Ocean (30°W to 10°E and 45°N to 65°N); the circumpolar region at latitudes greater than 45°N. The models were run for each region three times, each time being forced by the observed rising atmospheric CO<sub>2</sub> concentrations (Keeling et al., 2005) and meteorological data either from the National Center for Environmental Prediction (NCEP) reanalysis (Kalnay et al., 1996) or from the European Centre for Medium-Range Weather Forecasts (ECMWF) or from the NASA Jet Propulsion laboratory (JPL) (Atlas et al., 2011; Atlas et al., 1996).

The results of the model simulations generated CO<sub>2</sub> and O<sub>2</sub> fluxes in mol m<sup>-2</sup> yr<sup>-1</sup> covering the time period from the beginning of 1990 to the end of 2011 for the NCEP and ECMWF forcing, and covering the period from the beginning of 1990 to the end of 2010 for the JPL forcing. APO was calculated from these simulated CO<sub>2</sub> and O<sub>2</sub> fluxes, also in mol m<sup>-2</sup> yr<sup>-1</sup> and it must be noted that this calculation ignores the small influence that N<sub>2</sub> ocean fluxes would have on APO (Stephens et al., 1998). The results of the model runs are plotted in figure 3.13 along with the detrended Hpspline curve fit computed from the hourly averaged APO data from WAO. The models and curve fit were only plotted from 2007 since this is the first year of atmospheric APO measurements from WAO.

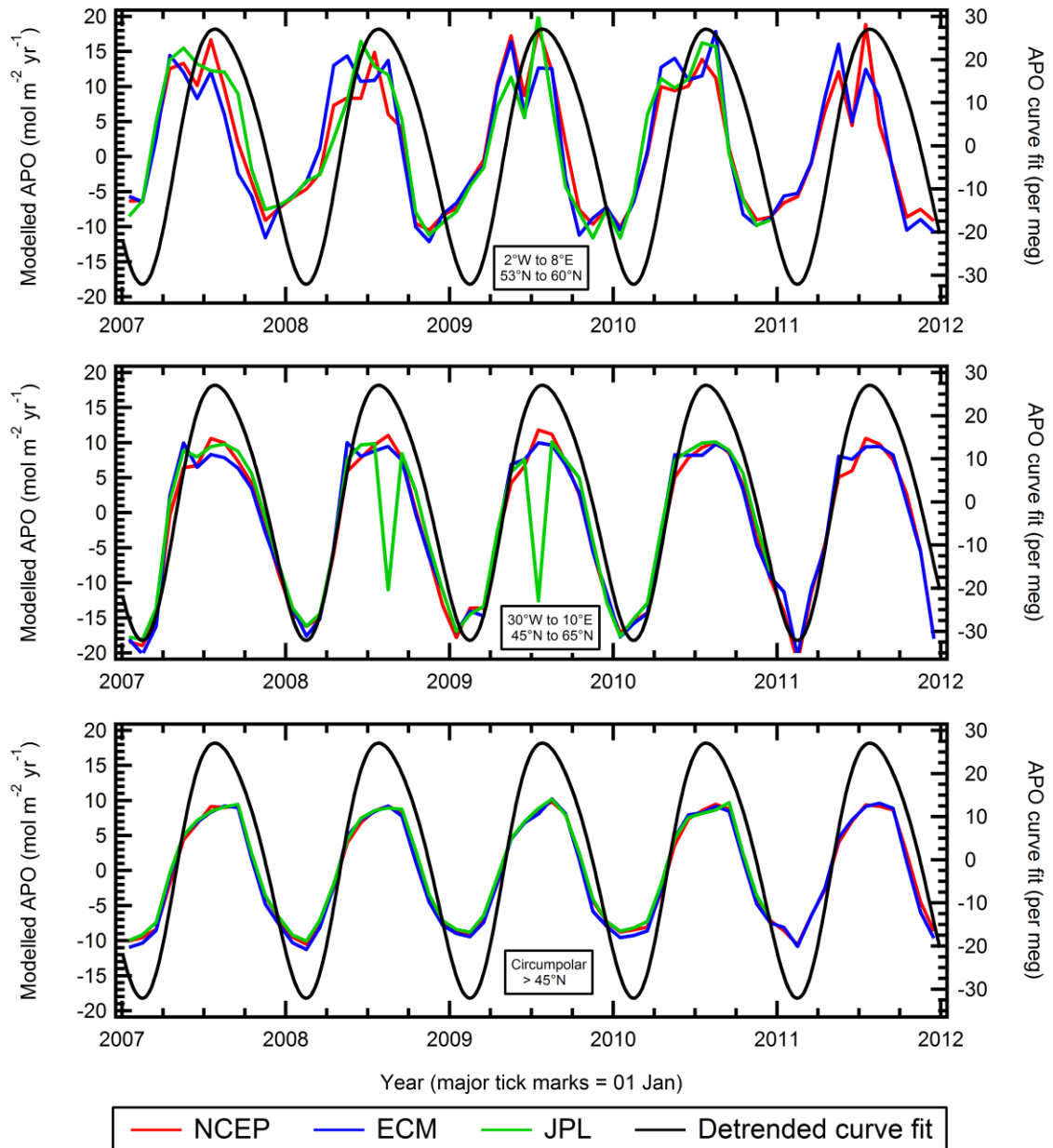


Figure 3.13. Modelled APO results for three different sized regions around WAO plotted along with the detrended Hpspline curve fit of WAO data from 2009 onwards. The three regions modelled, from top to bottom, are; the North Sea only (2°W to 8°E and 53°N to 60°N); a wider area, including parts of the Atlantic Ocean (30°W to 10°E and 45°N to 65°N); and the circumpolar region at latitudes greater than 45°N. The difference between the three model runs is the meteorological data used to force the model; the National Center for Environmental Prediction (NCEP) forcing is shown in red, European Centre for Medium-Range Weather Forecasts (ECMWF) forcing is shown in blue and NASA Jet Propulsion laboratory (JPL) forcing is shown in green. The detrended curve fit is plotted on the right hand axis in different units to the modelled APO and hence amplitudes can not be compared (however y-axis ranges are constant between the three plots). It must also be noted that the APO calculated from the model simulations ignores the small influence from N<sub>2</sub> ocean fluxes.

In general, the three different datasets used to force the model produce similar results. The overall amplitude of the seasonality is very similar between model runs for a given geographic area. For the circumpolar model runs (bottom panel of figure 3.13) all three outputs agree very closely with each other and show smooth seasonal curves with summer maxima and winter minima of similar magnitude.

For the area incorporating some of the North Atlantic Ocean (middle panel of figure 3.13) there is good agreement between model runs with the exception of an anomalous point midway through 2008 and 2009 for the JPL forcing. The model results, particularly from NCEP and ECMWF show a double harmonic in the APO seasonality with some maxima and minima exhibiting a double feature. The seasonal cycles are also slightly asymmetric; the moduli of the winter minima are greater than the moduli of the summer maxima. In addition, the summer maxima exhibit broader peaks than the winter minima.

For the area incorporating only the North Sea (top panel of figure 3.13), there is more variation in the output of the model runs and individual features in the seasonal cycles appear more emphasised as the curves are not as smooth as for the other areas. The seasonal cycles are again asymmetric, but for this area the moduli of the summer maxima are greater than the moduli of the winter minima, in contrast to the North Atlantic area. It is possible that running a global model on such a small area incorporating only the North Sea is an over-extension of the capabilities of the model and so perhaps the results are more variable and less robust.

The results of the model runs are in different units to the detrended curve fit values for the WAO APO observations. As such, the amplitudes of the modelled seasonal cycles can not be compared to the WAO curve fit seasonal amplitude. One can, however, compare features of the modelled seasonal cycles for the different geographic regions to the WAO curve fit. The curve fit results have the long-term trend removed and they show a mostly symmetric seasonality, with the summer maximum of similar magnitude to the winter minimum, which is most similar to the symmetric seasonality exhibited by the circumpolar curve fit. The phasing of the WAO seasonal cycle also appears to be most similar to the model results for the

circumpolar area, although it is also close to the results for the North Atlantic area. The phasing of the results for the North Sea show that it is ahead of the WAO curve fit, with downward and upward zero crossing days in many cases about 2 months earlier than the curve fit. The Hpspline curve fit incorporated only two harmonics and so will not show large deviations from a smooth curve; for this reason, it most closely resembles the smoothest model results, namely the circumpolar region north of 45°N.

Overall, the APO curve fit appears to exhibit the closest match to the model runs for the circumpolar region north of 45°N. This is not surprising, since the curve fit is based on all the data collected at WAO and air masses arriving at WAO are influenced by a variety of regions in the surrounding area. The different contrasting signals observed at WAO are explored in more detail in chapter 4. This preliminary model comparison could be improved by incorporating the influence of ocean N<sub>2</sub> fluxes into the simulated APO calculations. More rigorous filtering of the WAO data used to fit the Hpspline curve could also help to extract individual features in the APO seasonal cycle influenced by different geographical areas. Comparisons between observations and model simulations may also be more beneficial with a longer data record, when interannual variabilities and longer-term trends could also be included in the comparison. Finally, ‘inverting’ the WAO APO observations with an atmospheric transport model could result in quantifying APO fluxes as determined by the concentration measurements, which could then be directly compared to the model simulation flux results.

### 3.6 References

Atlas, R., Hoffman, R. N., Bloom, S. C., Jusem, J. C., and Ardizzone, J.: A multiyear global surface wind velocity dataset using SSM/I wind observations, *Bulletin of the American Meteorological Society*, 77, 869-882, 10.1175/1520-0477(1996)077<0869:amgswv>2.0.co;2, 1996.

Atlas, R., Hoffman, R. N., Ardizzone, J., Leidner, S. M., Jusem, J. C., Smith, D. K., and Gombos, D.: A cross-calibrated multiplatform ocean surface wind velocity product for meteorological and oceanographic applications, *Bulletin of the American Meteorological Society*, 92, 157-+, 10.1175/2010bams2946.1, 2011.

Bacastow, R. B., Keeling, C. D., and Whorf, T. P.: Seasonal amplitude increase in atmospheric CO<sub>2</sub> concentration at Mauna Loa, Hawaii, 1959-1982, *Journal of Geophysical Research-Atmospheres*, 90, 10529-10540, 10.1029/JD090iD06p10529, 1985.

Buitenhuis, E., Le Quere, C., Aumont, O., Beaugrand, G., Bunker, A., Hirst, A., Ikeda, T., O'Brien, T., Piontkovski, S., and Straile, D.: Biogeochemical fluxes through mesozooplankton, *Global Biogeochemical Cycles*, 20, 10.1029/2005gb002511, 2006.

Kalnay, E., Kanamitsu, M., Kistler, R., Collins, W., Deaven, D., Gandin, L., Iredell, M., Saha, S., White, G., Woollen, J., Zhu, Y., Chelliah, M., Ebisuzaki, W., Higgins, W., Janowiak, J., Mo, K. C., Ropelewski, C., Wang, J., Leetmaa, A., Reynolds, R., Jenne, R., and Joseph, D.: The NCEP/NCAR 40-year reanalysis project, *Bulletin of the American Meteorological Society*, 77, 437-471, 10.1175/1520-0477(1996)077<0437:tnyrp>2.0.co;2, 1996.

Keeling, C. D., Carter, A. F., Piper, S. C., Whorf, T. P., Heimann, M., Mook, W. G., and Roeloffzen, H.: A three-dimensional model of atmospheric CO<sub>2</sub> transport based on observed winds: 1. analysis of observational data., *American Geophysical Union, Geophysical Monograph* 55, 72, 1989.

Keeling, C. D., Chin, J. F. S., and Whorf, T. P.: Increased activity of northern vegetation inferred from atmospheric CO<sub>2</sub> measurements, *Nature*, 382, 146-149, 1996.

Keeling, C. D., Piper, S. C., Bacastow, R. B., Wahlen, M., Whorf, T. P., Heimann, M., and Meijer, H. A.: Atmospheric CO<sub>2</sub> and (CO<sub>2</sub>)-C-13 exchange with the terrestrial biosphere and oceans from 1978 to 2000: Observations and carbon cycle implications, in: *Ecological Studies*, edited by: Ehleringer, J. R., Cerling, T. E., and Dearing, M. D., *Ecological Studies : Analysis and Synthesis*, 83-113, 2005.

Kozlova, E. A., Manning, A. C., Kisilyakhov, Y., Seifert, T., and Heimann, M.: Seasonal, synoptic, and diurnal scale variability of biogeochemical trace gases and O<sub>2</sub> from a 300 m tall tower in central Siberia, *Global Biogeochemical Cycles*, 22, 10.1029/2008GB003209, 2008.

Le Quéré, C., Rödenbeck, C., Buitenhuis, E. T., Conway, T. J., Langenfelds, R., Gomez, A., Labuschagne, C., Ramonet, M., Nakazawa, T., Metzl, N., Gillett, N., and Heimann, M.: Saturation of the Southern Ocean CO<sub>2</sub> sink due to recent climate change, *Science*, 316, 1735-1738, doi:1710.1126/science.1136188, 10.1126/science.1136188, 2007.

Le Quéré, C., Raupach, M. R., Canadell, J. G., Marland, G., Bopp, L., Ciais, P., Conway, T. J., Doney, S. C., Feely, R. A., Foster, P., Friedlingstein, P., Gurney, K., Houghton, R. A., House, J. I., Huntingford, C., Levy, P. E., Lomas, M. R., Majkut, J., Metzl, N., Ometto, J. P., Peters, G. P., Prentice, I. C., Randerson, J. T., Running, S. W., Sarmiento, J. L., Schuster, U., Sitch, S., Takahashi, T., Viovy, N., van der Werf, G. R., and Woodward, F.

I.: Trends in the sources and sinks of carbon dioxide, *Nature Geoscience*, 2, 831-836, 10.1038/ngeo689, 2009.

Le Quéré, C., Takahashi, T., Buitenhuis, E. T., Rodenbeck, C., and Sutherland, S. C.: Impact of climate change and variability on the global oceanic sink of CO<sub>2</sub>, *Global Biogeochemical Cycles*, 24, 10.1029/2009gb003599, 2010.

Madec, G., and Imbard, M.: A global ocean mesh to overcome the North Pole singularity, *Climate Dynamics*, 12, 381-388, 10.1007/s003820050115, 1996.

Manning, A. J., O'Doherty, S., Jones, A. R., Simmonds, P. G., and Derwent, R. G.: Estimating UK methane and nitrous oxide emissions from 1990 to 2007 using an inversion modeling approach, *Journal of Geophysical Research-Atmospheres*, 116, 10.1029/2010jd014763, 2011.

Peters, G. P., Marland, G., Le Quere, C., Boden, T., Canadell, J. G., and Raupach, M. R.: Rapid growth in CO<sub>2</sub> emissions after the 2008-2009 global financial crisis, *Nature Clim. Change*, 2, 2-4, 10.1038/nclimate1332, 2012.

Piao, S. L., Ciais, P., Friedlingstein, P., Peylin, P., Reichstein, M., Luysaert, S., Margolis, H., Fang, J. Y., Barr, A., Chen, A. P., Grelle, A., Hollinger, D. Y., Laurila, T., Lindroth, A., Richardson, A. D., and Vesala, T.: Net carbon dioxide losses of northern ecosystems in response to autumn warming, *Nature*, 451, 49-U43, 2008.

Popa, M. E., Gloor, M., Manning, A. C., Jordan, A., Schultz, U., Haensel, F., Seifert, T., and Heimann, M.: Measurements of greenhouse gases and related tracers at Białystok tall tower station in Poland, *Atmospheric Measurement Techniques*, 3, 407-427, 10.5194/amt-3-407-2010, 2010.

Raupach, M. R., Marland, G., Ciais, P., Le Quéré, C., Canadell, J. G., Klepper, G., and Field, C. B.: Global and regional drivers of accelerating CO<sub>2</sub> emissions, *Proceedings of the National Academy of Sciences of the United States of America*, 104, 10288-10293, 2007.

Reinsch, C. H.: Smoothing by spline functions, *Numerische Mathematik*, 10, 177-183, 10.1007/bf02162161, 1967.

Stephens, B. B., Keeling, R. F., Heimann, M., Six, K. D., Murnane, R., and Caldeira, K.: Testing global ocean carbon cycle models using measurements of atmospheric O<sub>2</sub> and CO<sub>2</sub> concentration, *Global Biogeochemical Cycles*, 12, 213-230, 1998.

Theodosiou, M.: Forecasting monthly and quarterly time series using STL decomposition, *International Journal of Forecasting*, 27, 1178-1195, 10.1016/j.ijforecast.2010.11.002, 2011.

Thompson, R. L., Manning, A. C., Gloor, E., Schultz, U., Seifert, T., Hänsel, F., Jordan, A., and Heimann, M.: In-situ measurements of oxygen, carbon monoxide and greenhouse gases from Ochsenkopf tall tower in Germany, *Atmospheric Measurement Techniques*, 2, 573-591, 10.5194/amt-2-573-2009, 2009.

van der Laan-Luijkx, I. T., Karstens, U., Steinbach, J., Gerbig, C., Sirignano, C., Neubert, R. E. M., van der Laan, S., and Meijer, H. A. J.: CO<sub>2</sub>, ΔO<sub>2</sub>/N<sub>2</sub> and APO: observations from the Lütjehad, Mace Head and F3 platform flask sampling network, *Atmos. Chem. Phys.*, 10, 10691-10704, 10.5194/acp-10-10691-2010, 2010.

**CHAPTER 4 – SHORT-TERM AND EVENT ANALYSIS OF THE  
WEYBOURNE RECORDS**

## 4.1 Introduction to chapter

In this chapter the CO<sub>2</sub> and O<sub>2</sub> records from Weybourne Atmospheric Observatory (WAO) are examined in detail with particular attention given to short-term events (of length from hours to a week) and how the meteorology experienced at WAO affects the data collected.

## 4.2 Data analysis methods specific to this chapter

### 4.2.1 Particle dispersion model footprints

Towards the end of this chapter, when examining individual short-term events observed at WAO, I present a number of plots showing the history of air masses that arrive at WAO at different times. These plots are based on calculations using a particle dispersion model and were produced by Zoë Fleming, an NCAS (National Centre for Atmospheric Science) scientist at the University of Leicester, UK. Dispersion models calculate air mass ‘footprints’ based on Lagrangian particle dispersion models that map the chaotic pathways of air parcels as probability distributions. The position of an individual parcel of air following average atmospheric motion through time is plotted for a given time window. Dispersion models are based on how individual particles move independently from one another, and they also attempt to represent air turbulence; they are therefore more accurate models than back trajectory analysis (Stohl et al., 2002). The footprints I show are 2-D probability maps created by backward runs in time from the moment the air arrived at WAO and indicate which regions have influenced that air before its arrival.

The dispersion model used to create these plots is the UK Met Office’s Numerical Atmospheric dispersion Modelling Environment (NAME model) (Ryall and Maryon, 1998; Jones et al., 2007). The NAME model was run in backwards mode, for a 10-day history at 3-hourly intervals. Particles were released from 50 m above sea level to approximate the height at which air is collected at WAO, and all instances when the particles are less than 100 m from the ground, when they could pick up surface influences, are recorded. The horizontal spatial resolution of the

model is  $0.25^\circ \times 0.25^\circ$  (Fleming et al., 2012). The model output footprints represent the likely paths of 30,000 inert tracer particles released in the 3 hour window from the start time labelled on each plot and traced backwards in time. The particles are modelled as a tracer species and have been compared to using CO as a tracer (Zoë Fleming, *personal communication*), they have mass but no reactivity so are moved around by turbulence and affected by deposition but not by chemical reactions. The colour coded plots represent the probability that a particle travelled through a grid cell at less than 100 m from surface level. The scale on each plot is a relative scale in  $\text{g s/m}^3$  and so colours cannot be compared exactly between plots.

### 4.3 Diurnal cycles

In general, there are daily cycles in the concentrations of  $\text{CO}_2$  and  $\text{O}_2$  in the atmosphere. These cycles are caused by diurnal cycling in the land biotic processes of photosynthesis and respiration. Sunlight is essential for photosynthesis to occur and so this only occurs during daylight hours. During daylight hours  $\text{CO}_2$  is consumed and  $\text{O}_2$  is produced leading to a net build up in  $\text{O}_2$  and net reduction in  $\text{CO}_2$ . Respiration occurs throughout the day and night, but it is the dominant process at night when photosynthesis cannot occur. Therefore during night time,  $\text{CO}_2$  accumulates in the atmosphere and  $\text{O}_2$  diminishes. There are smaller diurnal effects related to temperature; within ambient ranges warmer temperatures speed up the processes of both respiration and photosynthesis. This tends to speed up the rates of these processes during the day so they reach a maximum when the day is at its warmest, usually in the early afternoon. These processes are occurring and contributing to the diurnal cycles but at a near ground level site like WAO the rectifier effect, discussed below, often masks the magnitude of fluxes due to photosynthesis during the day.

Temperature cycling will warm and cool the oceans and therefore one might expect some diurnal effect from a changing gas solubility in the oceans. In reality this is not observed on diurnal timescales. The heat capacity of water is high and means that it can buffer the changes in temperature over timescales of hours and so a change in atmospheric concentrations is not observed. This is most clearly

demonstrated by the APO signal. APO is insensitive with respect to the terrestrial processes that dominate the diurnal cycle and so it does not show a diurnal variation. The oceanic processes primarily responsible for variations in APO do not occur quickly enough to be visible on a diurnal timescale. Although some ocean events such as upwelling or ventilation, and phytoplankton blooms can occur very rapidly, and do influence O<sub>2</sub> and CO<sub>2</sub> concentrations in the water column, these changes are not reflected in atmospheric variability on diurnal time scales since air-sea equilibration times are much slower than daily time scales.

A further effect of temperature and irradiation changes during the day is on the height of the atmospheric boundary layer (ABL). This is the height at which turbulent transfers of heat, mass and momentum between the Earth's surface and the atmosphere are insignificant when averaged over a period of an hour (Arya, 1981). For this reason it is sometimes described as the well mixed layer, or just 'mixing height'. During the cooler night time the boundary layer tends to be more stable and also lower than during the day when extra radiation from the sun makes the layer more turbulent, more variable and generally higher. It is important to take the ABL into account, particularly when modelling global circulation (Deardorf, 1972a, b) and considering pollutants released from the Earth's surface (Zilitinkevich and Baklanov, 2002). As the boundary layer height gets lower, the volume of air it represents above the Earth's surface gets less and so it can have the effect of increasing concentrations of species within this layer. This is called the diurnal rectifier effect. When considering diurnal changes in boundary layer height, they will affect both O<sub>2</sub> and CO<sub>2</sub> in the same manner rather than having opposing effects like the terrestrial processes considered earlier.

The height of the tower at WAO, 10 m above ground level (a.g.l.) and 20 m above sea level (a.s.l.), means that we are always sampling from within the well mixed layer. Therefore the role of the changing ABL height is key to the diurnal cycles observed. At night the generally low mixing height means that ground level sources and sinks are visible in the data recorded at WAO and these are due to respiration as there is no light for photosynthesis to occur. During the day, the ABL is much higher and so any fluctuations near the ground due to sources and sinks from both respiration and photosynthesis are quickly diluted over a large air mass.

Figure 4.1 shows one week of data recorded at WAO in early October 2011. For CO<sub>2</sub>, O<sub>2</sub> and APO each point represents 2 minute averages, for the meteorological values of irradiance and temperature each point represents a 10 minute average. This figure is a good example of how diurnal cycles are seen when sampling continuously at a station such as WAO.

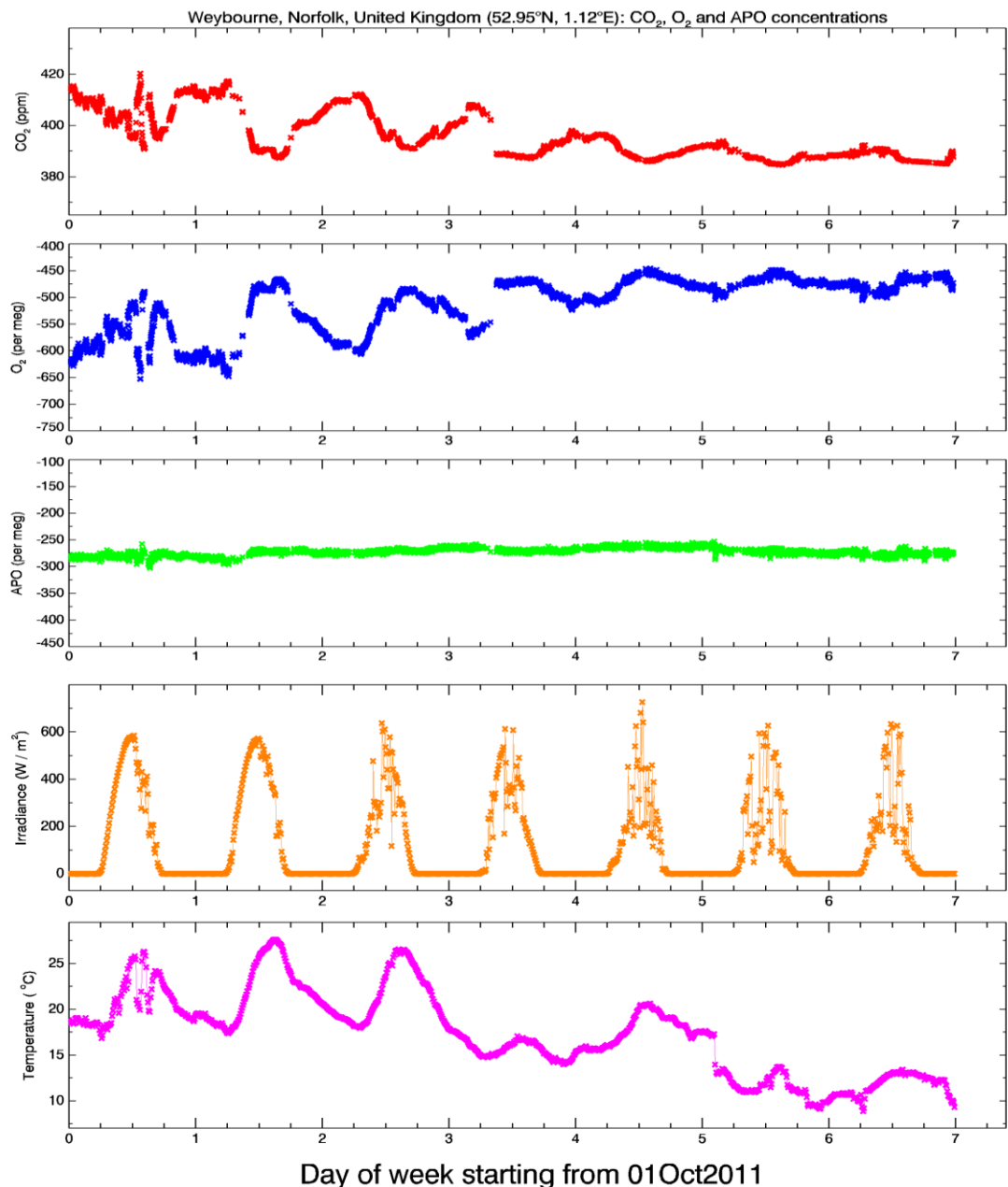


Figure 4.1. One week of data from WAO showing the diurnal cycles seen in CO<sub>2</sub> (red), O<sub>2</sub> (blue) and the absence of a diurnal cycle in APO (green). Y-axis scales were chosen to be visually comparable. Irradiance (orange) and temperature (purple) are also plotted to show how these vary on each day throughout the week and the effect this has on the diurnal cycles observed for CO<sub>2</sub> and O<sub>2</sub>. The concentration data points are 2 minute averages and the meteorological data points are 10-minute averages.

On the first day there is not a clear diurnal cycle as both O<sub>2</sub> and CO<sub>2</sub> fluctuate throughout the day. Most of the variability is cancelled out in the APO signal but some remains and the first day shows more variation in APO than the rest of the week. On this day wind speeds were low at between 1 and 3 ms<sup>-1</sup> and wind direction was changing frequently, the temperature was also quite variable throughout the day. The noisy signal with elevated CO<sub>2</sub>, depleted O<sub>2</sub> and low wind speed most likely indicates that the overriding signal on this day was due to local pollution as the same air mass swirled around and was repeatedly sampled at WAO.

On the following six days from the 2<sup>nd</sup> to 6<sup>th</sup> October a clear diurnal cycle is visible in CO<sub>2</sub> and O<sub>2</sub> while APO remains constant and fluctuates very little. The cycles for O<sub>2</sub> and CO<sub>2</sub> are as would be expected from the influence of the terrestrial biosphere, when taking the diurnal rectifier effect into account. CO<sub>2</sub> is at a minimum during the daylight hours, shown by the irradiance plot. During the day the temperature and convective currents are high and so a high ABL is set up, this effectively dilutes the apparent concentration of CO<sub>2</sub>. Photosynthesis will be the dominating process during these hours but it is very hard to see fluxes due to photosynthesis in the signals due to the high ABL. At night, the temperature drops and so will convective mixing and the ABL drops in altitude, now only respiration can occur and the signal can be seen in the data from WAO as the ABL is low; CO<sub>2</sub> builds up to a maximum. O<sub>2</sub> is anti-correlated due to the stoichiometry of the reactions that describe respiration. On these six days the wind speed had picked up from that seen on the 1<sup>st</sup> October and remains between 5 ms<sup>-1</sup> and 12 ms<sup>-1</sup> for the rest of the week. The local pollution effects seen on the first day are no longer present and the diurnal cycles can now be seen. As the week goes on the diurnal cycles becomes less and less pronounced as the variation between day and night concentrations becomes increasingly less significant. The reason for this can be seen in the meteorological plots in the bottom two panels of figure 4.1. Over the course of the week there is a large drop in daytime temperature from a maximum of over 25°C at the start of the week to around 10°C by the end of the week. The reduction in temperature, and the fact that there is much less difference between day and night time temperatures, suggests that the ABL is not changing as much

between day and night and so the diurnal rectifier effect is less pronounced. Lower temperatures also slow the rate of respiration and so the night time build-up of  $\text{CO}_2$  is less pronounced, also reducing the amplitude of the diurnal cycle. Photosynthesis will also be reduced with less light and lower temperatures but these signals are harder to determine from measurements within the boundary layer.

Solar radiation and temperature are very important to the seasonal cycles seen in  $\text{CO}_2$  and  $\text{O}_2$ . WAO is situated at a latitude of nearly  $53^\circ\text{N}$  and so the weather is seasonal and experiences a relatively large variation in day length throughout the course of a year. This variation is reflected in the diurnal cycles observed at different times of year. Figure 4.2 shows the variation in diurnal cycle for four distinct three month periods throughout the year for  $\text{CO}_2$  and figure 4.3 does similarly for  $\text{O}_2$ . These plots were obtained by binning the data based on the time of day. An average concentration and standard deviation (represented by the error bars) is calculated for each hour. Average irradiance values are also calculated and are plotted on the right hand axis. Within each species the axis are kept constant for the four different times of year to facilitate comparison.

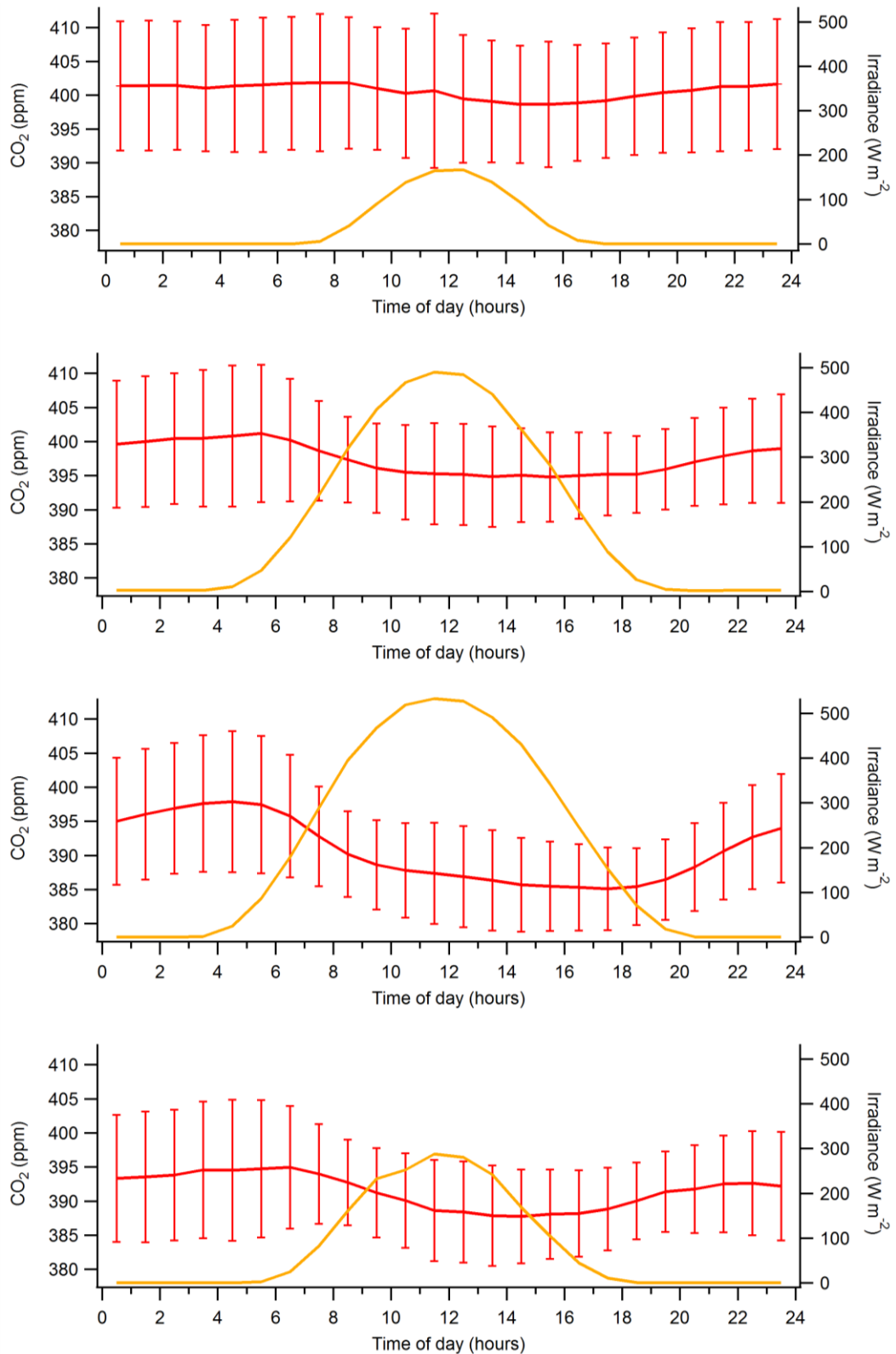


Figure 4.2. Plots of the average diurnal cycle in CO<sub>2</sub> (red, with 1 standard deviation error bars) for different 3 month periods of the year. From top to bottom: Winter (December, January and February); spring (March, April and May); summer (June July and August); autumn (September, October and November). The average diurnal irradiance for these periods is also plotted in orange and refers to the right hand axis.

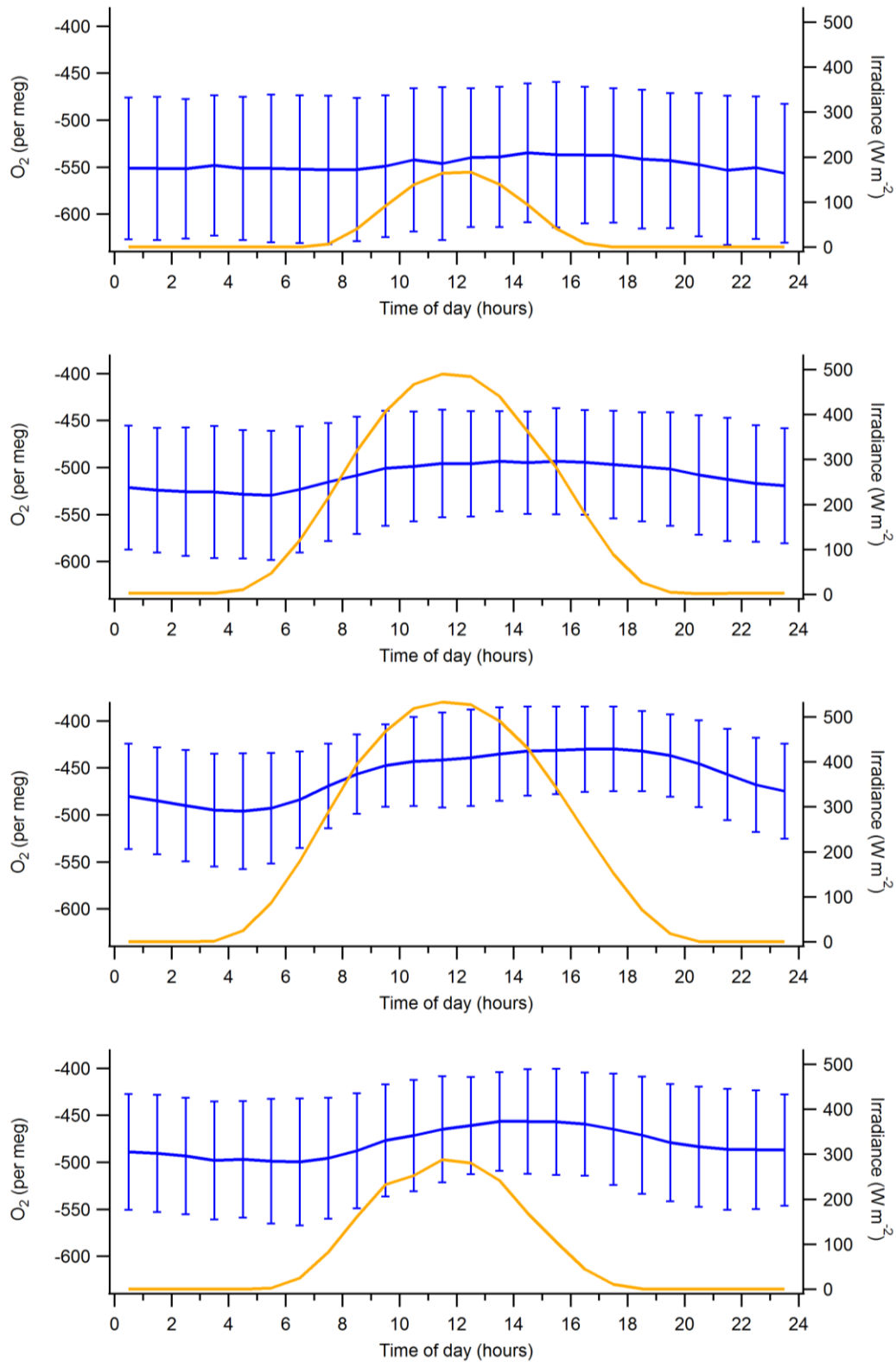


Figure 4.3. Plots of the average diurnal cycle in O<sub>2</sub> (blue, with 1 standard deviation error bars) for different 3 month periods of the year. From top to bottom: Winter (December, January and February); spring (March, April and May); summer (June July and August); autumn (September, October and November). The average diurnal irradiance for these periods is also plotted in orange and refers to the right hand axis.

The CO<sub>2</sub> and O<sub>2</sub> data show an anti-correlated diurnal relationship, from consideration of the diurnal rectifier effect this is mainly due to the observed respiration signals over night. The diurnal cycle is most obvious in the spring and summer plots and almost indiscernible in the winter plot. In winter the relative inactivity of the terrestrial biosphere almost diminishes the diurnal cycle completely. The relative inactivity in winter can also be seen in the timing of the peaks and troughs of the cycle. In summer, when the number of hours of daylight is at the maximum, the maxima and minima in the diurnal cycle for CO<sub>2</sub> and O<sub>2</sub> are around 3 hours later in the day than during winter. The diurnal rectifier effect is strongest during spring and summer. The seasonal rectifier effect means that the diurnal cycling of the ABL height is less pronounced during the colder winter months and so diurnal cycles are less pronounced.

#### 4.4 Meteorological based filtering

Meteorological data are collected at WAO concurrently to atmospheric concentration measurements being recorded. Unfortunately the meteorological data are collected as single measurements at a frequency of every 10 minutes while data points for O<sub>2</sub> and CO<sub>2</sub> are collected as averages every two minutes, it is therefore necessary to match the data points' timestamps in order to assign meteorological data to each concentration data point. Once this is done it is possible to produce a wind rose for WAO. This is shown in the first panel of figure 4.4. The wind rose shows the wind speed and wind direction for each 2-minute data point of the WAO O<sub>2</sub> and CO<sub>2</sub> record. The directions observed are binned into 15° sectors and then wind speeds are grouped into 4 ms<sup>-1</sup> ranges and colour coded. The radius of each band within a sector illustrates the percentage of time this range of speeds was observed during the entire data record. When looking at these data it is important to remember that the wind direction assigned to the data is only the direction at the point in time that it arrives at WAO and does not tell us exactly where the air mass has been previously. The idea of the wind rose has been extended in the three other panels in figure 4.4 so that the concentrations of CO<sub>2</sub>, O<sub>2</sub> and APO are plotted together with the wind direction at the time they were recorded at WAO.

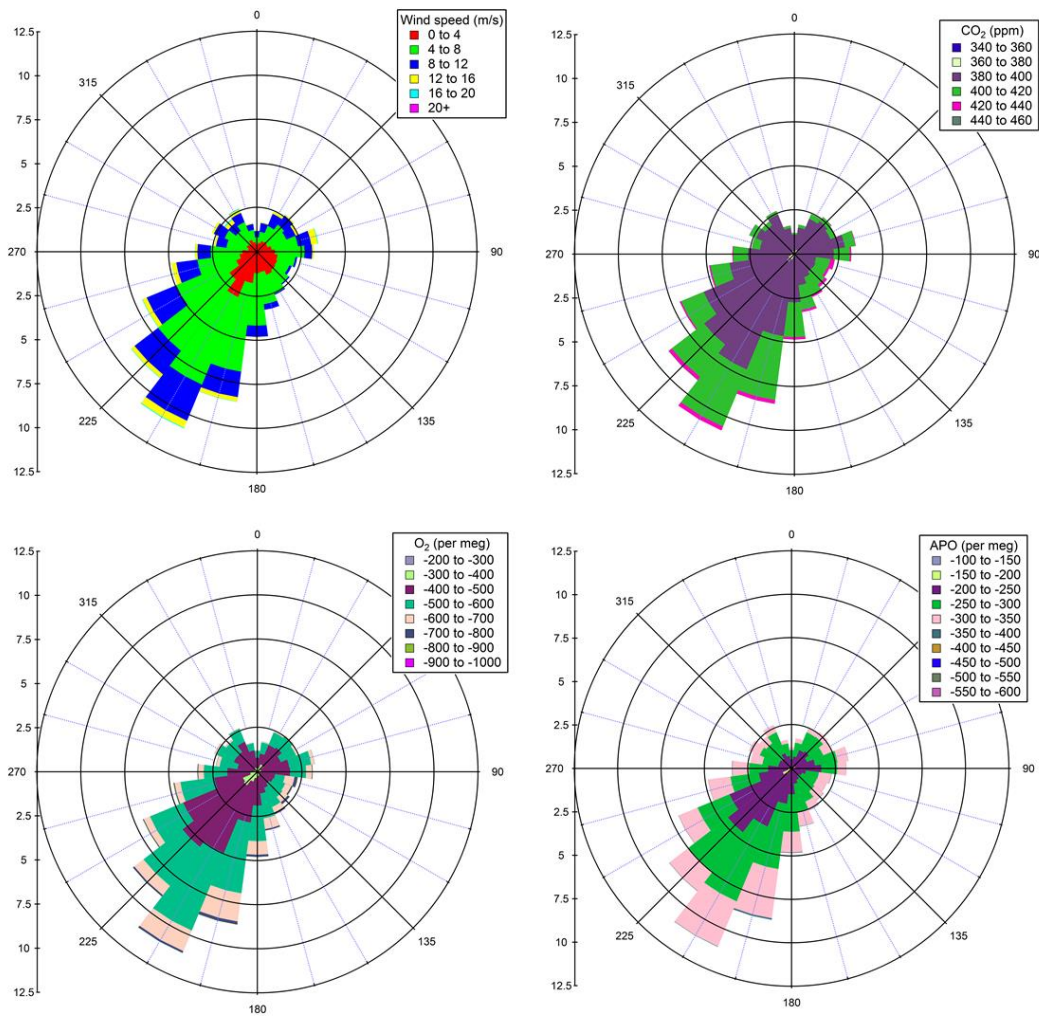


Figure 4.4. Wind rose and concentration roses for the entire dataset from WAO. The directions observed are binned into 15° sectors and wind speeds (top left) CO<sub>2</sub> concentrations (top right), O<sub>2</sub> concentrations (bottom left) or APO concentrations (bottom right) are represented in colour coded bands corresponding to the different ranges shown in the legends. The radius of each band within a sector is proportional to the percentage of time this range of speeds or concentrations is observed with percentage values denoted on the left axis correspond to the concentric rings.

This analysis very readily shows that the dominant wind sector observed at WAO is the south west quadrant. By integrating within the quadrants we find that winds arrive at WAO from the south west quadrant for approximately 49% of the entire data record. Wind arrives from the north west quadrant 16% of the time, from the north east quadrant 17% of the time and from the south east quadrant 18% of the time.

Before looking at the concentrations observed from different wind directions the data are examined to see if there is any seasonality in the wind directions

observed. Data were binned into three month periods, in the same manner as the analysis of the diurnal cycles: Winter (December, January and February); spring (March, April and May); summer (June July and August); autumn (September, October and November). The wind and concentration rose analysis is then performed and the results are shown in figures 4.5 – 4.8.

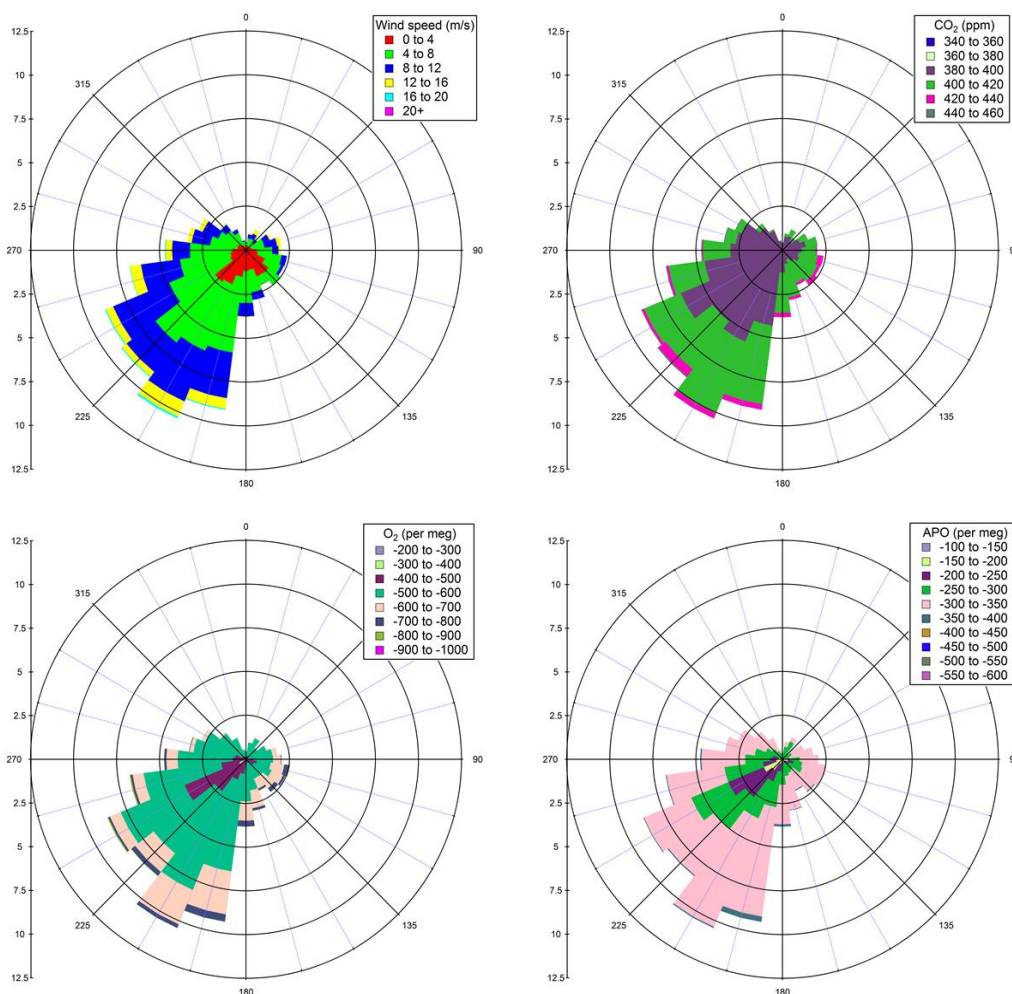


Figure 4.5. Wind rose and concentration roses for all data collected during the winter months of December January and February at WAO. The directions observed are binned into 15° sectors and wind speeds (top left) CO<sub>2</sub> concentrations (top right), O<sub>2</sub> concentrations (bottom left) or APO concentrations (bottom right) are represented in colour coded in bands corresponding to different ranges shown in the legends. The radius of each band within a sector is proportional to the percentage of time this range of speeds or concentrations is observed with percentage values denoted on the left axis correspond to the concentric rings.

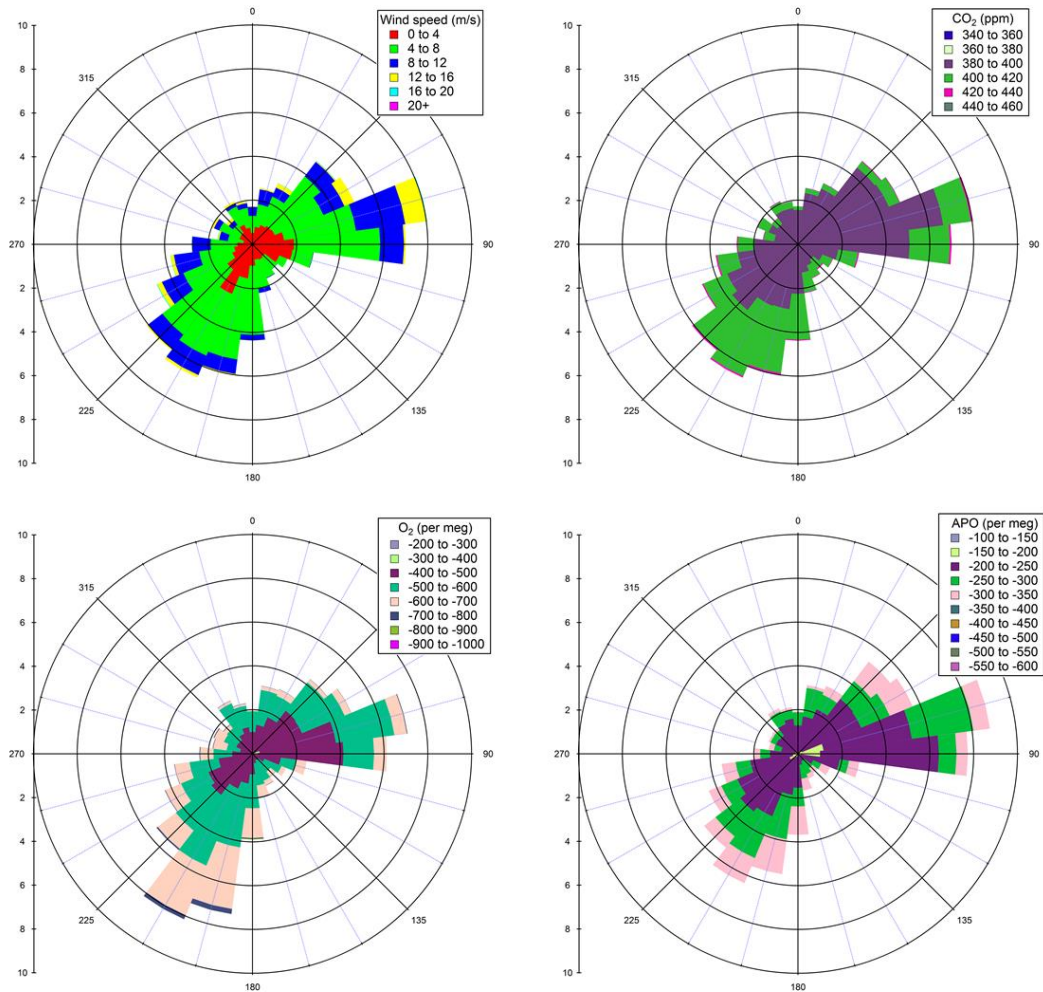


Figure 4.6. Wind rose and concentration roses for all data collected during the spring months of March, April and May at WAO. The directions observed are binned into 15° sectors and wind speeds (top left) CO<sub>2</sub> concentrations (top right), O<sub>2</sub> concentrations (bottom left) or APO concentrations (bottom right) are represented in colour coded in bands corresponding to different ranges shown in the legends. The radius of each band within a sector is proportional to the percentage of time this range of speeds or concentrations is observed with percentage values denoted on the left axis correspond to the concentric rings.

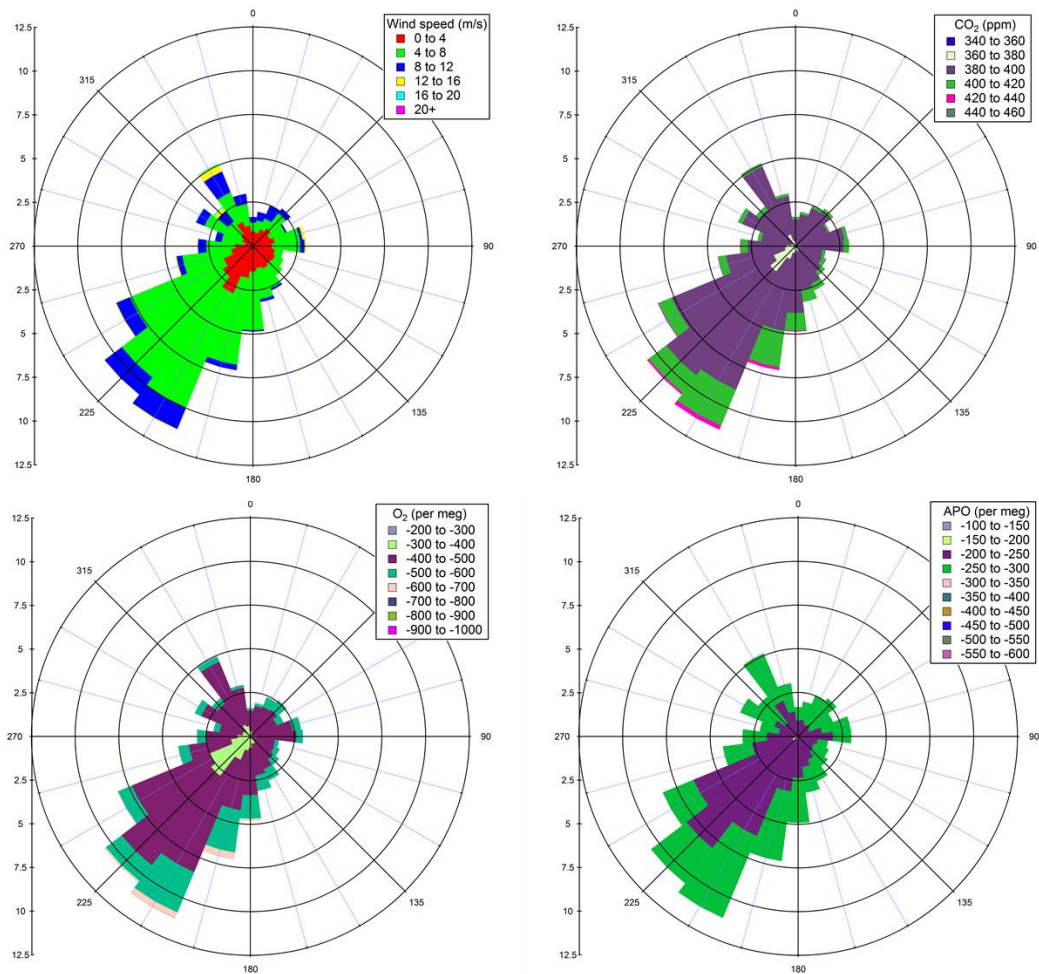


Figure 4.7. Wind rose and concentration roses for all data collected during the summer months of June, July and August at WAO. The directions observed are binned into 15° sectors and wind speeds (top left) CO<sub>2</sub> concentrations (top right), O<sub>2</sub> concentrations (bottom left) or APO concentrations (bottom right) are represented in colour coded in bands corresponding to different ranges shown in the legends. The radius of each band within a sector is proportional to the percentage of time this range of speeds or concentrations is observed with percentage values denoted on the left axis correspond to the concentric rings.

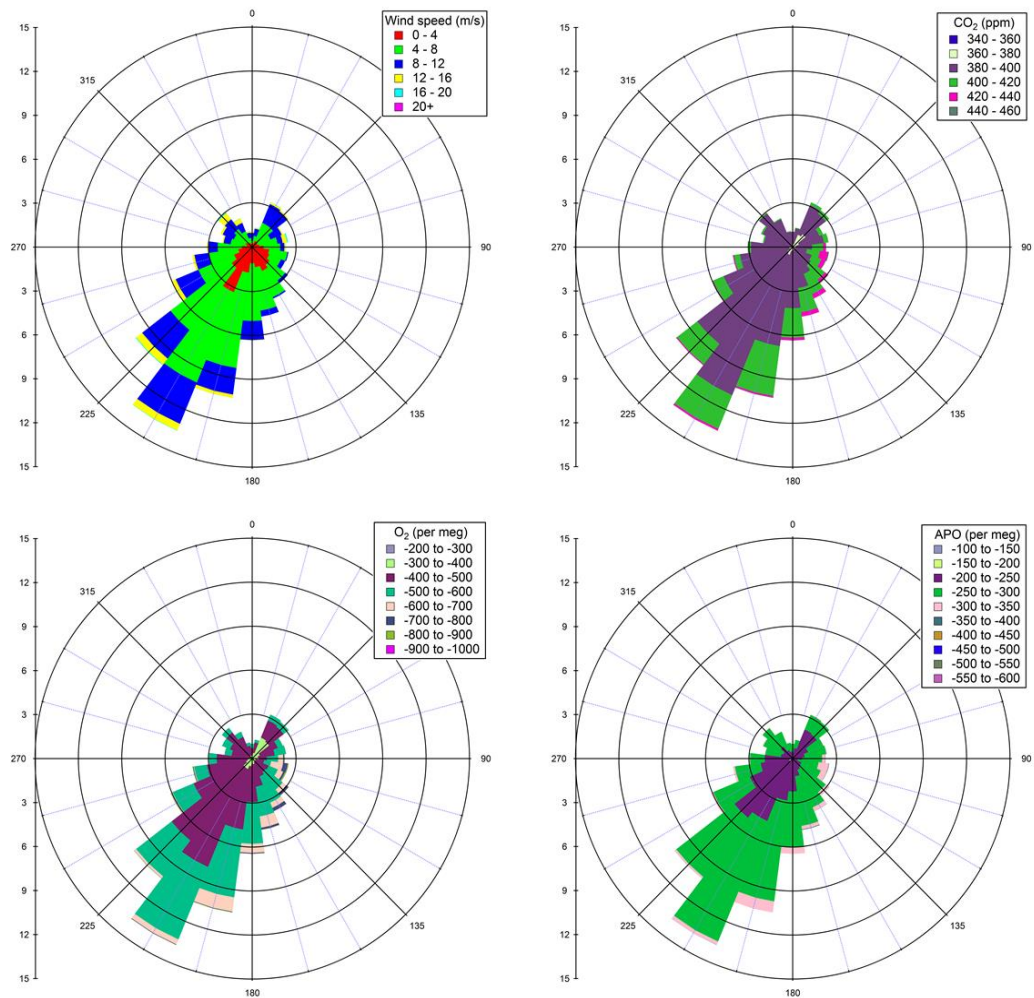


Figure 4.8. Wind rose and concentration roses for all data collected during the autumn months of September, October and November at WAO. The directions observed are binned into 15° sectors and wind speeds (top left) CO<sub>2</sub> concentrations (top right), O<sub>2</sub> concentrations (bottom left) or APO concentrations (bottom right) are represented in colour coded in bands corresponding to different ranges shown in the legends. The radius of each band within a sector is proportional to the percentage of time this range of speeds or concentrations is observed with percentage values denoted on the left axis correspond to the concentric rings.

From the seasonal plots in figures 4.5-4.8 it is clear that the south west quadrant dominates at most times of the year. This is particularly true in autumn (figure 4.8) and winter (figure 4.5) where the southwest quadrant is a more dominant source than during other periods at the expense of contributions from all other quadrants. In summer (figure 4.7) the southwest quadrant is still the most dominant contributor but there is a significantly larger contribution from the north west quadrant and less from the south east quadrant. The most markedly different season appears to be spring (figure 4.6) where there's a significant contribution

from the north east quadrant, almost equal to that from the south west quadrant. The percentage contribution of each quadrant to local wind direction for the different times of year are summarised in table 4.1 below:

Quadrant	All data	DJF	MAM	JJA	SON
North east	17%	9%	33%	16%	10%
South east	18%	18%	17%	14%	23%
South west	49%	56%	37%	48%	55%
North west	16%	17%	13%	22%	12%

Table 4.1. Summary of the percentage contribution of each of the four quadrants of wind directions arriving at WAO. The figures are given for the whole data set and then for subsets of the data filtered by time of year. DJF is for the months of December, January and February; MAM for March, April and May; JJA for June July and August; SON for September, October and November.

The seasonal concentration rose plots also show the seasonal cycle observed in the different species. Overall CO<sub>2</sub> concentrations are lower in summer than in winter while O<sub>2</sub> and APO concentrations are higher in summer than in winter; this has been discussed in chapter 3. Of more interest are the wind directions from which we see different concentration profiles. Figure 4.4, plotting all data, shows that the higher concentrations of CO<sub>2</sub> are more predominantly seen from wind directions in the south west and south east quadrants. Conversely the lowest concentrations of O<sub>2</sub> are seen in the south west and south east quadrants. This anti-correlation suggests that terrestrial biosphere or anthropogenic processes are most likely the cause of the elevated CO<sub>2</sub> and depleted O<sub>2</sub>. Air arriving at WAO from the south west quadrant is likely to either originate from or be mixed with air from London or industrial cities of the midlands. This air is likely to be polluted air and thus will include a significant fossil fuel signal. Air arriving from the south east quadrant will have most likely come from the direction of continental Europe. Air masses arriving at WAO that have come from the south east have passed over France, Belgium, The Netherlands and Germany, with just a short passage over the English Channel or North Sea. It is thus possible that the elevated CO<sub>2</sub> and depleted O<sub>2</sub> observed in the south east quadrant include influences from polluted air and from the significant terrestrial biosphere of continental Europe.

When examining the seasons individually the overall pattern is similar to the data taken as a whole. The higher CO<sub>2</sub> concentrations and lower O<sub>2</sub> concentrations are often observed more noticeably in the south west and south east quadrants. In winter (figure 4.5) this is very noticeable with significant contributions of CO<sub>2</sub> above 420 ppm and O<sub>2</sub> below -700 per meg seen in the two southern quadrants whereas these extremes of concentration are not observed very much at all for the two northern quadrants. In summertime (figure 4.7) the higher CO<sub>2</sub> concentrations and lower O<sub>2</sub> concentrations are more noticeable in the south western quadrant than they are in the south eastern quadrant. Interestingly in summer we also see a significant contribution from higher O<sub>2</sub> concentrations (> -400 per meg) in the south western and north western quadrants. The higher concentrations could be due to an oceanic signal from the northern Atlantic as summer outgassing of O<sub>2</sub> occurs to elevate the O<sub>2</sub> concentration reinforcing the already higher levels of O<sub>2</sub> due to terrestrial photosynthesis at this time of year. In the summer APO plot there is a large contribution from APO concentrations greater than -250 per meg in the south western quadrant so oceanic signals may indeed be having an influence. In the spring plots (figure 4.6) there is a strong contribution from the north eastern quadrant and quite a large variation in APO concentrations is observed in this quadrant. APO concentrations show significant contributions in the range from -150 to -350 per meg in the north eastern quadrant. This high variability may in part be a function of the time of year as during this spring period the seasonal cycle of APO transitions from the winter minimum to the summer maximum and so will show more variability. The variability also indicates that there are oceanic signals being observed at this time of year, driving the seasonality seen in APO. When the autumn plots (figure 4.8) are examined, we might expect to see a large variation in APO again as the seasonal cycle moves from the summer maximum to the winter minimum, however the plot is dominated by wind directions from the south western quadrant and APO concentrations between -200 and -300 make up the vast majority of the observations. It appears that it is possible to see an oceanic signal from the north eastern quadrant as air arrives at WAO from the North Sea and possibly from the Arctic Ocean beyond.

Despite the limitation that using wind directions recorded at the instant a measurement is taken does not provide a full history of the wind parcel arriving at WAO at that point in time, it does appear that some broad differences in concentrations arriving from different directions may be seen. It was decided to extend this approach and use wind direction to quickly filter all of the data. Given that this is a relatively crude method the data were split into four different sectors: arriving from Europe (90 – 180°); arriving from southern England and London (180 – 255°); arriving from northern England and Scotland (255 – 330°); and arriving from the North Sea (330 – 90°). The filtered data for each sector are presented in figures 4.9 – 4.12, data points corresponding to wind speeds less than 3 ms<sup>-1</sup> were removed completely as local influences will dominate the signal.

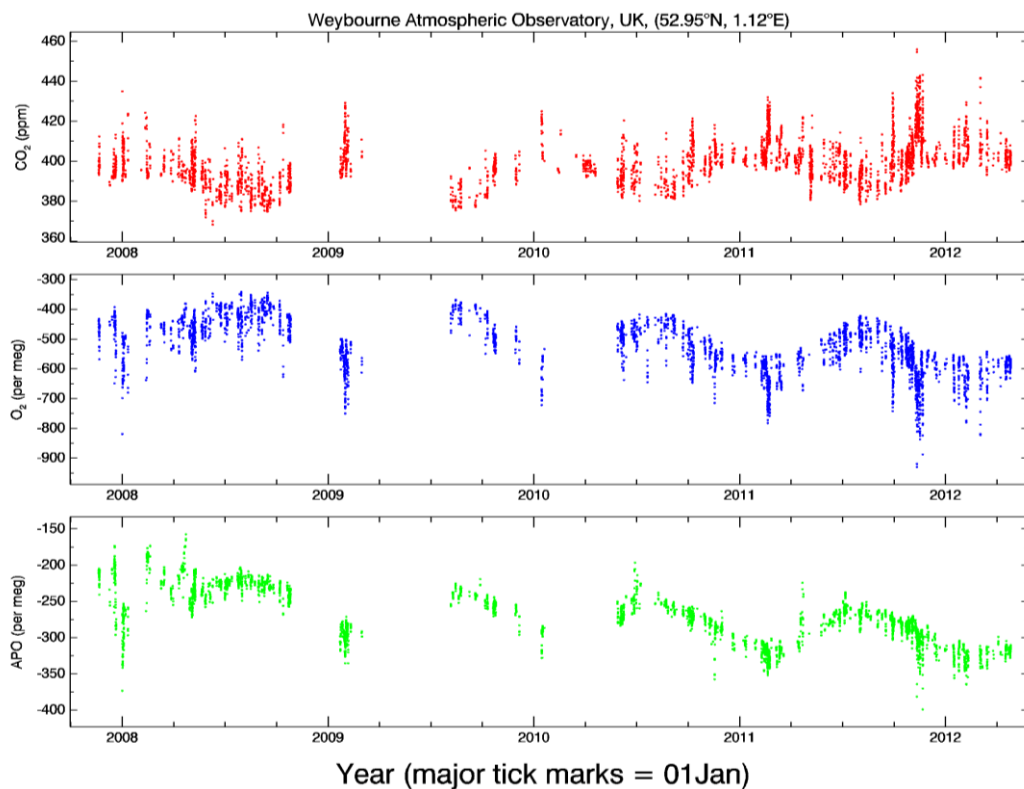


Figure 4.9. 2-minute averages recorded at WAO for all data arriving at WAO with a wind speed greater than 3 m s<sup>-1</sup> and with a local wind direction between 90 and 180° (continental Europe).

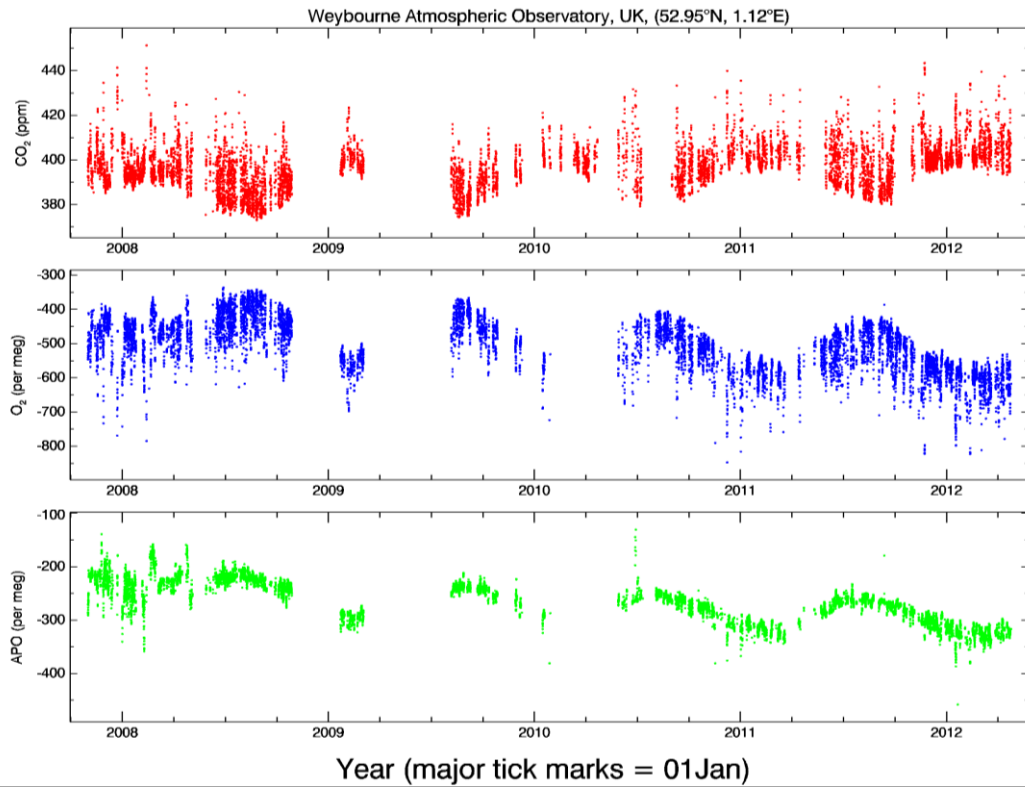


Figure 4.10. 2-minute averages recorded at WAO for all data arriving at WAO with a wind speed greater than  $3 \text{ m s}^{-1}$  and with a local wind direction between  $180$  and  $255^\circ$  (southern England and London).

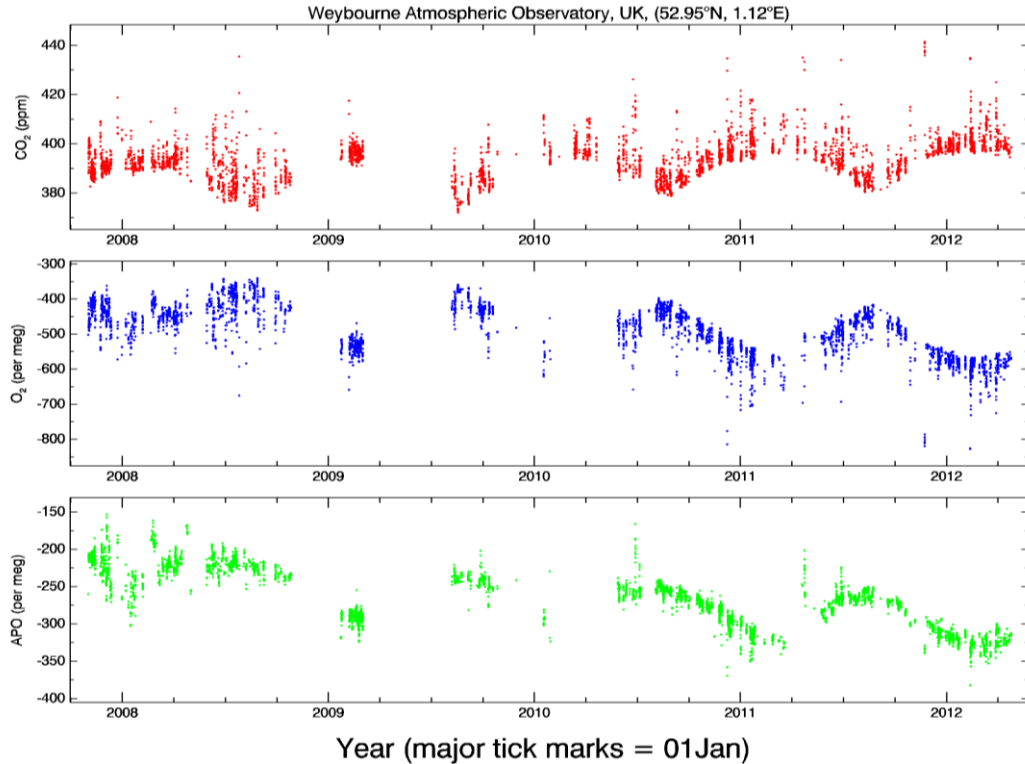


Figure 4.11. 2-minute averages recorded at WAO for all data arriving at WAO with a wind speed greater than  $3 \text{ m s}^{-1}$  and with a local wind direction between  $255$  and  $330^\circ$  (northern England and Scotland).

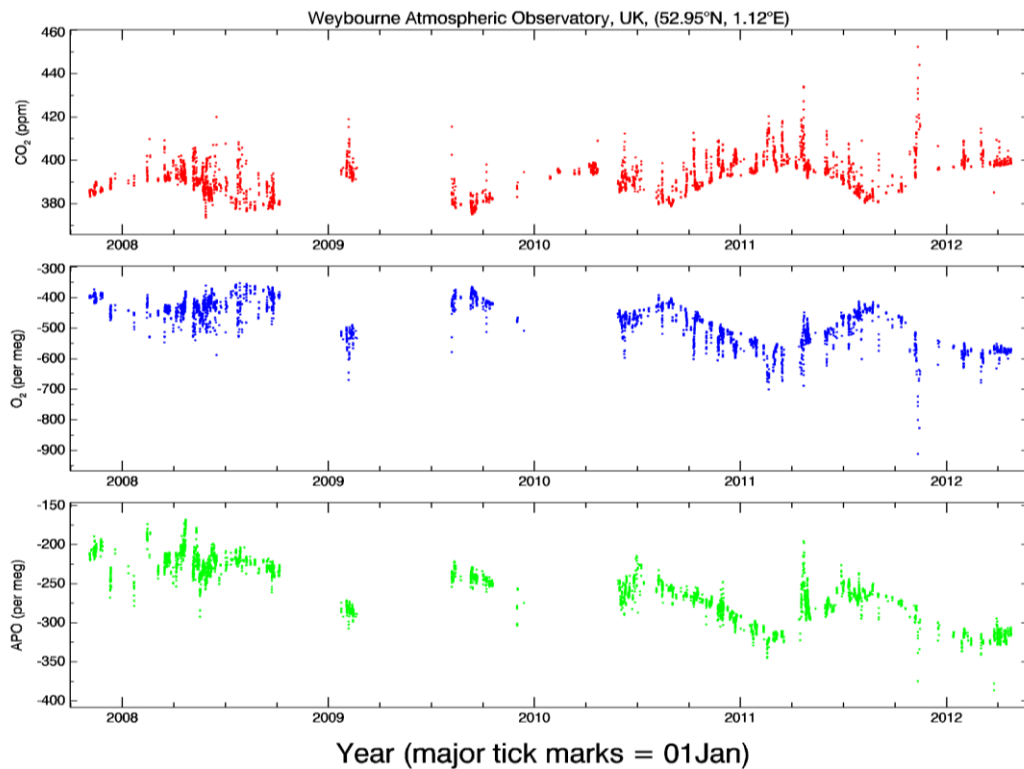


Figure 4.12. 2-minute averages recorded at WAO for all data arriving at WAO with a wind speed greater than  $3 \text{ m s}^{-1}$  and with a local wind direction between  $330^\circ$  and  $90^\circ$  (the North Sea).

Curve fits using the Hpspline program were then performed on the filtered data sets, using the same parameters used for the curve fits previously performed on the whole data set (presented in chapter 3). From these curve fits, seasonal amplitudes are calculated based on 12 months of data, calculated at a frequency of every 6 months. The seasonal amplitudes calculated for each species and for each wind sector are shown in tables 4.2 – 4.4.

Midpoint of 12 month period	CO <sub>2</sub> seasonal amplitude (ppm) 90-180°	CO <sub>2</sub> seasonal amplitude (ppm) 180-255°	CO <sub>2</sub> seasonal amplitude (ppm) 255-330°	CO <sub>2</sub> seasonal amplitude (ppm) 330-90°	CO <sub>2</sub> seasonal amplitude (ppm) all data
2009.5	24.3	17.0	16.3	20.4	17.9
2010	19.6	15.7	15.1	18.4	15.7
2010.5	14.9	9.4	15.2	14.2	13.5
2011	15.7	9.6	15.6	15.9	13.6
2011.5	22.5	12.2	15.9	18.8	13.9
<b>Average</b>	<b>19.4</b>	<b>12.8</b>	<b>15.6</b>	<b>17.5</b>	<b>14.9</b>

Table 4.2. Seasonal amplitudes observed at WAO for CO<sub>2</sub> based on curve fits of data filtered into four sectors of wind direction. Seasonal amplitudes are calculated by subtracting the seasonal minimum from the seasonal maximum concentration for a 12 month period of data and this was repeated every 6 months.

Midpoint of 12 month period	O <sub>2</sub> seasonal amplitude (per meg) 90-180°	O <sub>2</sub> seasonal amplitude (per meg) 180-255°	O <sub>2</sub> seasonal amplitude (per meg) 255-330°	O <sub>2</sub> seasonal amplitude (per meg) 330-90°	O <sub>2</sub> seasonal amplitude (per meg) all data
2009.5	188.1	150.7	141.6	161.5	155.3
2010	176.0	148.3	142.8	154.6	145.9
2010.5	134.3	117.2	130.1	117.4	121.3
2011	140.6	116	131.0	127.1	122.6
2011.5	164.0	117.6	134.4	143.4	126.1
<b>Average</b>	<b>160.6</b>	<b>130.0</b>	<b>136.0</b>	<b>140.8</b>	<b>134.2</b>

Table 4.3. Seasonal amplitudes observed at WAO for O<sub>2</sub> based on curve fits of data filtered into four sectors of wind direction. Seasonal amplitudes are calculated by subtracting the seasonal minimum from the seasonal maximum concentration for a 12 month period of data and this was repeated every 6 months.

Midpoint of 12 month period	APO seasonal amplitude (per meg) 90-180°	APO seasonal amplitude (per meg) 180-255°	APO seasonal amplitude (per meg) 255-330°	APO seasonal amplitude (per meg) 330-90°	APO seasonal amplitude (per meg) all data
2009.5	69.3	68.2	64.8	58.5	66.2
2010	67.0	68.6	69.9	51.7	58.9
2010.5	62.8	56.3	57.6	45.8	52.1
2011	62.5	60.0	58.2	53.0	57.3
2011.5	63.0	64.4	60.5	56.4	60.5
<b>Average</b>	<b>64.9</b>	<b>63.5</b>	<b>62.2</b>	<b>53.1</b>	<b>59.0</b>

Table 4.4. Seasonal amplitudes observed at WAO for APO based on curve fits of data filtered into four sectors of wind direction. Seasonal amplitudes are calculated by subtracting the seasonal minimum from the seasonal maximum concentration for a 12 month period of data and this was repeated every 6 months.

Plots of the amplitudes for each species are shown in figures 4.13 – 4.15, in order to show the variations between the four different wind sectors and the fit for all of the data.

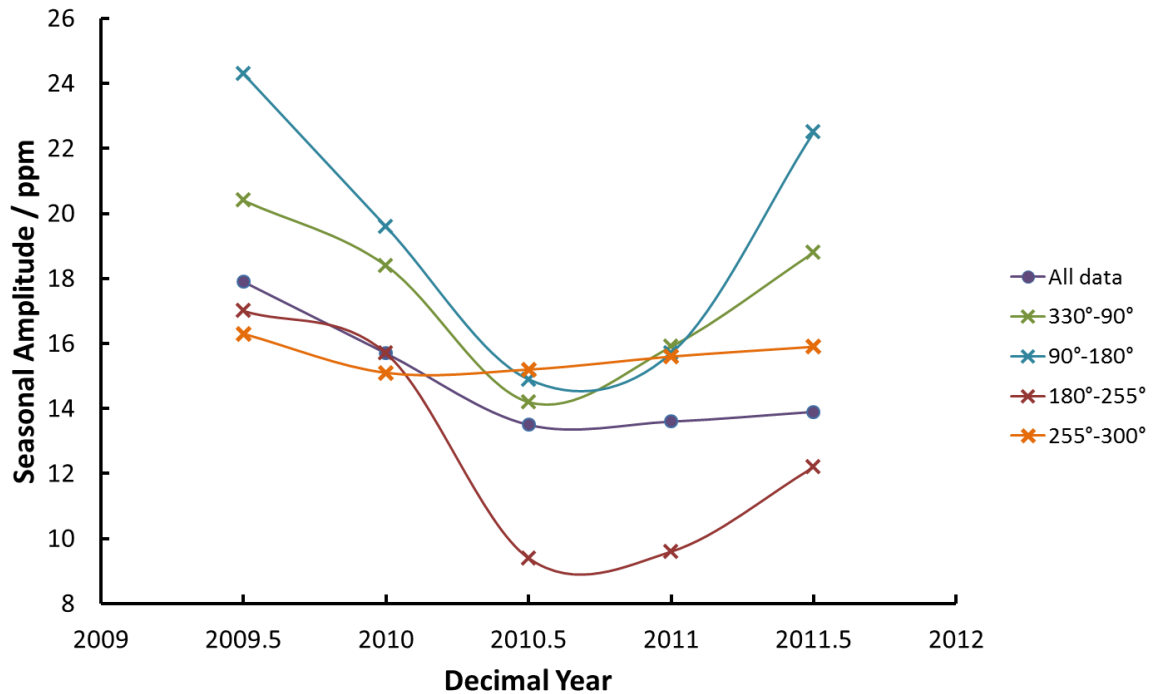


Figure 4.13. Plot of the annual seasonal amplitudes of CO<sub>2</sub> calculated based on curve fits of data filtered by the wind direction at the time the data were collected. Seasonal amplitudes are calculated for a 12 month period every 6 months, the points are plotted on the date corresponding to the mid-point of the 12 month period. Data taken from table 4.2.

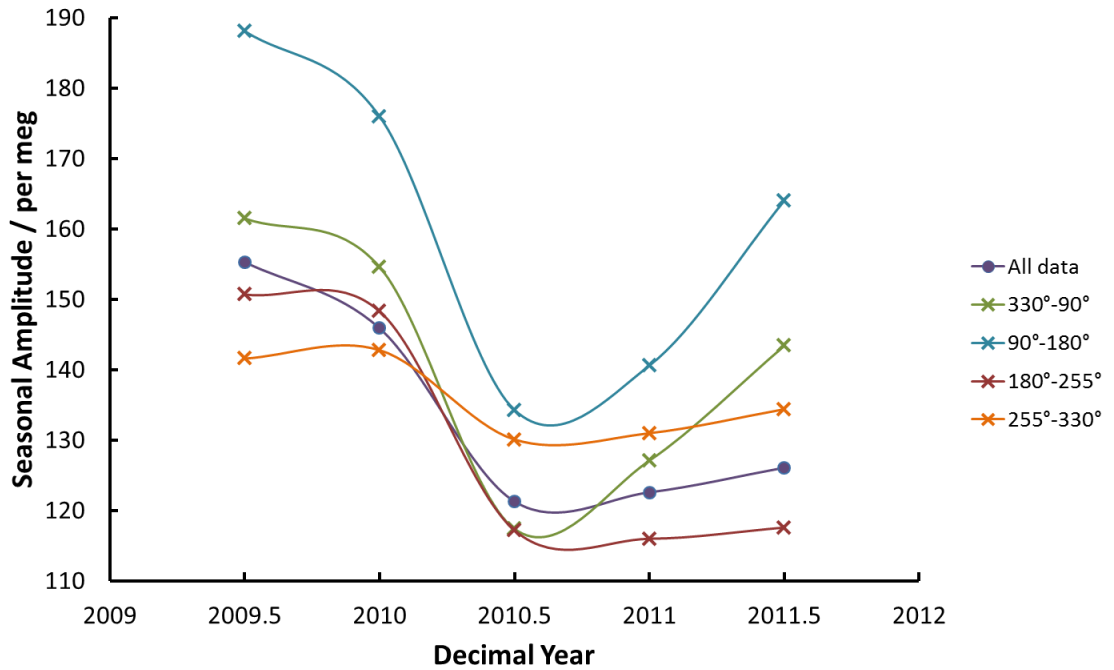


Figure 4.14. Plot of the annual seasonal amplitudes of O<sub>2</sub> calculated based on curve fits of data filtered by the wind direction at the time the data were collected. Seasonal amplitudes are calculated for a 12 month period every 6 months, the points are plotted on the date corresponding to the mid-point of the 12 month period. Data taken from table 4.3.

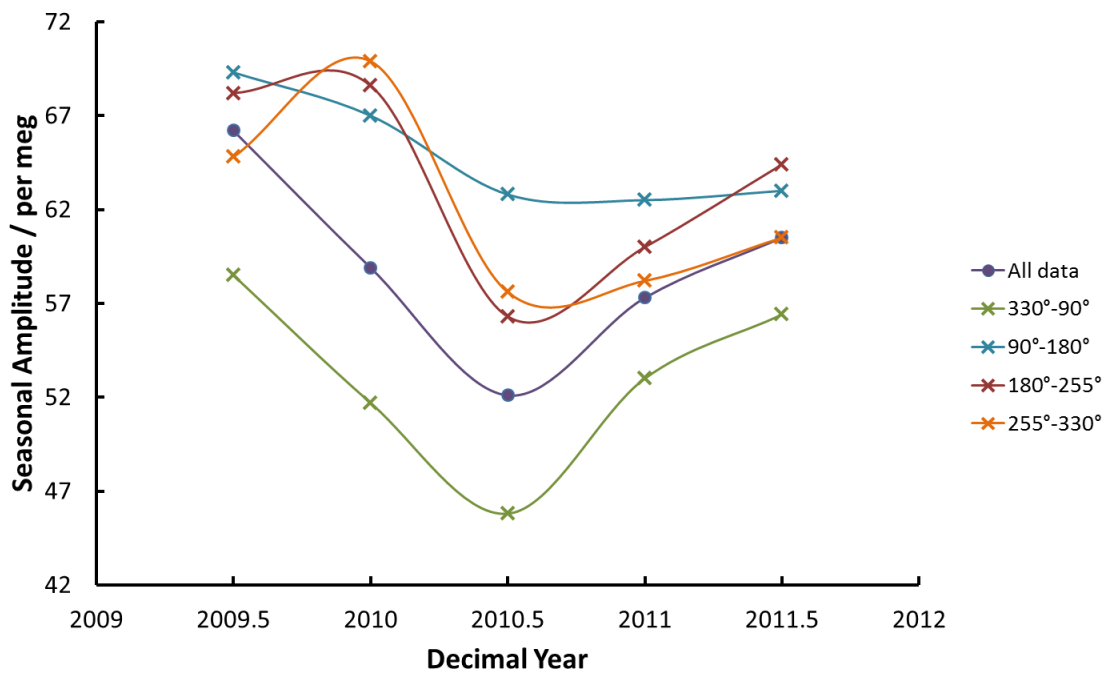


Figure 4.15. Plot of the annual seasonal amplitudes of APO calculated based on curve fits of data filtered by the wind direction at the time the data were collected. Seasonal amplitudes are calculated for a 12 month period every 6 months, the points are plotted on the date corresponding to the mid-point of the 12 month period. Data taken from table 4.4.

In this data I am not looking to draw firm conclusions on the trend in the seasonal amplitudes observed at WAO, the data record is too short and that is not the purpose of this analysis. Instead it is interesting to look at differences between the data from different wind sectors. For CO<sub>2</sub> and O<sub>2</sub> the variability in seasonal amplitude between different wind sectors follows similar patterns, this is to be expected from the interconnected nature of processes with respect to these two species. For CO<sub>2</sub> and more markedly for O<sub>2</sub>, the seasonal amplitudes observed for data based on the wind sector 90 – 180°, the Europe sector, is consistently higher than that observed for the other sectors. Although air from Europe must cross the English Channel or the North Sea before reaching WAO, continental Europe is the largest land mass close to WAO. The additional terrestrial biosphere associated with this may explain to some extent why the amplitude of the seasonal cycle for air from this sector is greater than for any other sector. Terrestrial processes are the major driver of the seasonal cycle in CO<sub>2</sub> and O<sub>2</sub> for Northern hemisphere sites, air reaching WAO from Europe is likely to have spent the longest residence time over the terrestrial biosphere and therefore will be most influenced by the processes associated with it and display the largest seasonal cycle. It is worth noting that the population density in Europe is generally less than in the UK, particularly southern and middle England. Most of England's forests were cleared centuries ago, either for housing and industry or for agricultural use. This relative lack of forests in England may also partially explain why the seasonal cycles in CO<sub>2</sub> and O<sub>2</sub> from the southern England and London region, and the northern England and Scotland region (which includes the Midlands), are less pronounced compared to the European sector.

The seasonal amplitudes in O<sub>2</sub> and CO<sub>2</sub> associated with the North Sea sector (330 – 90°) are still quite high, at many points higher than the seasonal cycle for the two wind sectors over England. This cannot solely be explained by the oceanic seasonal cycle in O<sub>2</sub> based on outgassing in the warmer summer months as the large seasonal amplitude is observed in CO<sub>2</sub> as well. The fact that the North Sea sector has a relatively large seasonal amplitude has 2 possible causes: the air that arrives at WAO from this sector also has a significant terrestrial influence, probably from mixing within the atmosphere and also the fact that the back trajectories of air

arriving at WAO from this direction include a significant residence time over land masses. The second influence could be that air from the 2 sectors incorporating the UK to the east has a significant oceanic component associated with them. This is entirely possible as before the air travels over the UK and to WAO it is likely to have come from the north Atlantic further west. The north Atlantic is a vast ocean and air could have been resident over it for some time before travelling across the UK to WAO. A combination of both of these explanations is likely to be the cause of the higher amplitudes observed in CO<sub>2</sub> and O<sub>2</sub> for the North Sea sector compared to the 2 UK sectors.

Figure 4.15 shows the variation in amplitudes observed in the APO seasonal cycle for the different sectors and for all data. The amplitude of the seasonal cycle in APO for the North Sea sector is consistently lower in magnitude than that observed for the other three sectors. This is a slightly surprising result as if oceanic processes dominate air arriving at WAO from this sector then the opposite might be expected since the seasonality in APO is dominated by oceanic processes and is insensitive to terrestrial processes. The reasons for this could be explained in a similar manner to the reason for the O<sub>2</sub> seasonal cycle being more pronounced in the North Sea sector than in the two UK sectors.

#### 4.5 Examination of pollution events.

In order to look at the different kinds of air that WAO sees at different times it is necessary to look at a number of short-term events in more detail. This involves picking out events of interest based on the concentrations observed at WAO and then looking at this shorter time frame in detail to gain a complete picture. The spatial history of the air that WAO sees at these times is examined using air mass footprints. The O<sub>2</sub>:CO<sub>2</sub> ratio during the events was also calculated using the Isoplot 4 plug in for Microsoft Excel developed at Berkeley Geochronology Centre (BGC). The O<sub>2</sub>:CO<sub>2</sub> ratio can be indicative of different sources of air and together with the footprints this can help identify the nature of the air that is being sampled. Polluted air signals are looked at first and then a period of clean air and oceanic signals is examined.

To identify possible polluted air the first thing to look at are the plots of CO<sub>2</sub>, O<sub>2</sub> and APO, in particular the APO trace. APO is calculated by weighting the CO<sub>2</sub> concentration using the molar exchange ratio for processes in the terrestrial biosphere, 1.1 (Severinghaus, 1995). The molar exchange ratio for burning fossil fuels are different from that for photosynthesis and respiration and are well defined; 1.17 for coal, 1.44 for oil and liquid fossil fuels and 1.95 for natural gas (Keeling, 1988). A global average of 1.39 was calculated in the 1990s (Manning and Keeling, 2006) using data from Marland et al (2008). Therefore when polluted air is being sampled we would expect to see a drop in APO as it is being calculated using a weighting on the CO<sub>2</sub> concentration that is too low for the processes being observed. When a drop in APO is observed for a short period of time and this coincides with elevated CO<sub>2</sub> concentrations and depleted O<sub>2</sub> concentrations then this event was examined further by calculating an O<sub>2</sub>:CO<sub>2</sub> ratio using Isoplot and by looking at the source of air using the footprints.

I looked at data from January 2010 to April 2012, this is the period after significant upgrades were made to the system during 2009 and I have the most confidence in the data quality for this period. The first significant pollution event identified was during the period 12<sup>th</sup> to 15<sup>th</sup> January 2010. During this period there are clearly elevated CO<sub>2</sub> and depleted O<sub>2</sub> levels and a reduction in APO can clearly be seen. Data for the week starting 8<sup>th</sup> January 2010 are shown in figure 4.16; the pollution event can clearly be seen in the last 2 days of the week.

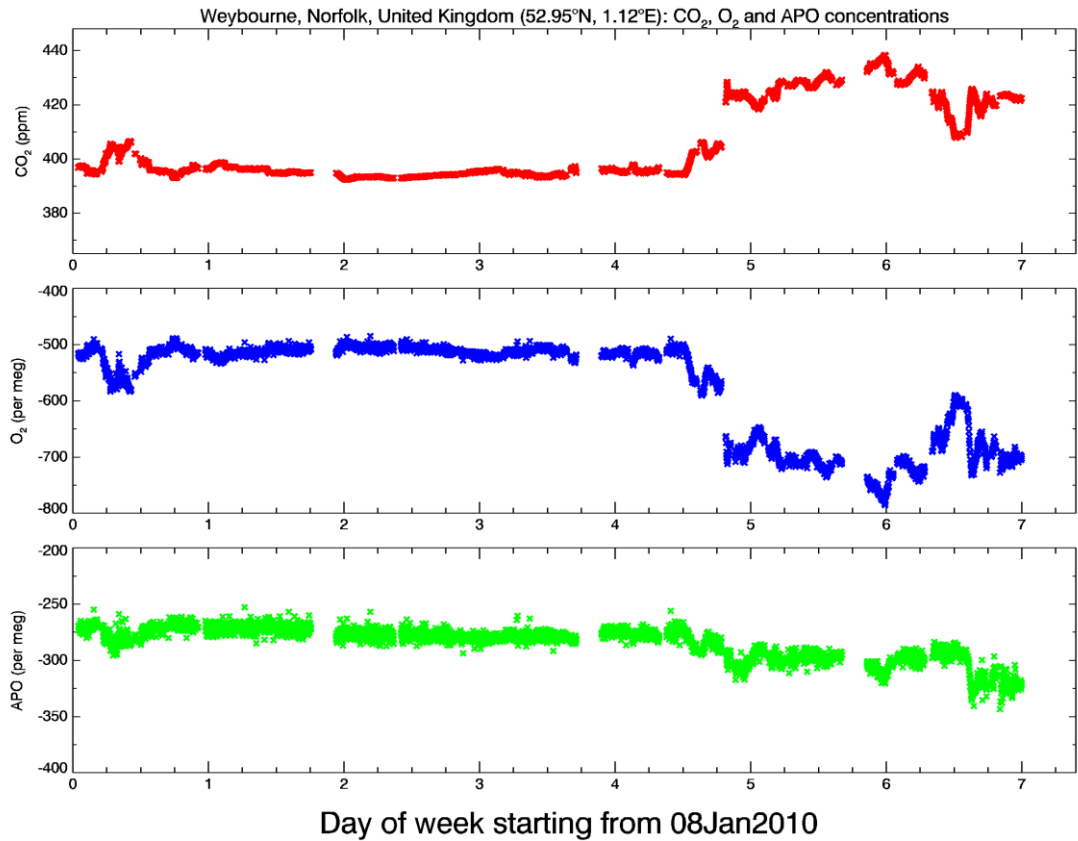


Figure 4.16. CO<sub>2</sub> (red), O<sub>2</sub> (blue) and APO (green) data for the week starting on the 8<sup>th</sup> January 2010. The sharp rise in CO<sub>2</sub> levels and drops in O<sub>2</sub> and APO levels starting on the 12<sup>th</sup> January can clearly be seen. This kind of trace is used to identify possible pollution events in the WAO record. Note that the APO y-axis has half the range of the O<sub>2</sub> axis in order to show the deviation in APO more clearly. The O<sub>2</sub> and CO<sub>2</sub> y-axis are visually comparable.

Isoplot was run on this data to determine the O<sub>2</sub>:CO<sub>2</sub> ratio for the period with the most elevated CO<sub>2</sub> levels, from the 13<sup>th</sup> January at 05:01 to 14<sup>th</sup> January 06:50, during this period CO<sub>2</sub> levels were above 425 ppm and O<sub>2</sub> levels were below -650 per meg. The resulting plot and gradient are shown in figure 4.17.

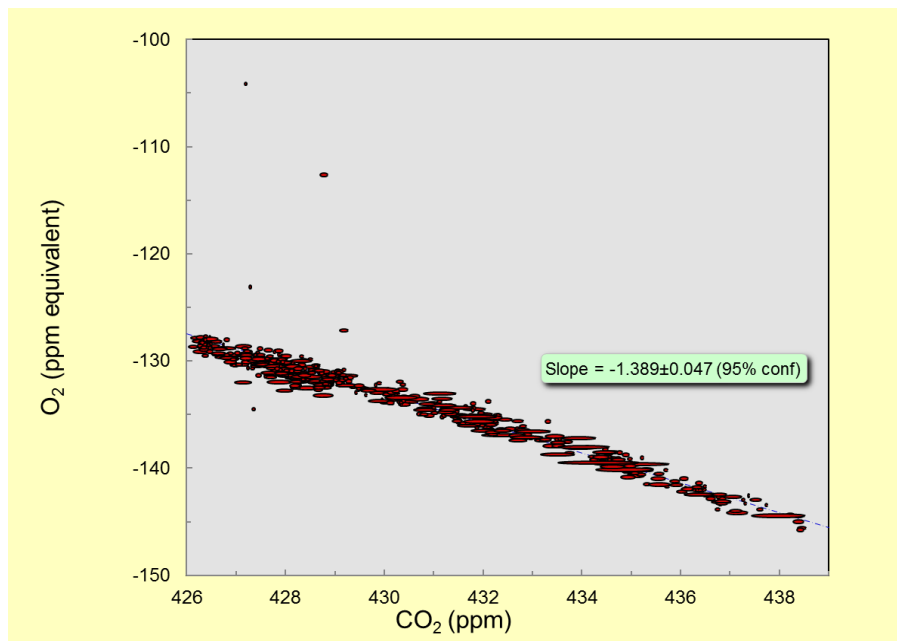


Figure 4.17. Isoplot of O<sub>2</sub> concentrations in ppm equivalent units versus CO<sub>2</sub> in ppm covering the time period 13<sup>th</sup> January at 05:01 to 14<sup>th</sup> January 06:50. The ovals represent a 2 minute data point with one standard deviation error in both species. The resultant slope of a linear fit through the data is an O<sub>2</sub>:CO<sub>2</sub> ratio 1.389 ±0.047.

The O<sub>2</sub>:CO<sub>2</sub> ratio during this period is 1.389, much higher than the expected ratio of 1.1 for processes in the terrestrial biosphere and indicative of a mixed fossil fuel signal of 1.39 (Manning and Keeling, 2006) or close to an oil and liquid fossil fuel signal of 1.44 (Keeling, 1988).

Subsequent examination of the air mass footprints during this time period shows that WAO was seeing a clear signal from continental Europe, as shown in figure 4.18. Most of the air is coming from Southern Germany and the Netherlands but with significant contribution from other European countries as well. The beginning of January 2010 was very cold and the signal is likely to be primarily the result of fossil fuel being burned for heating and power generation.

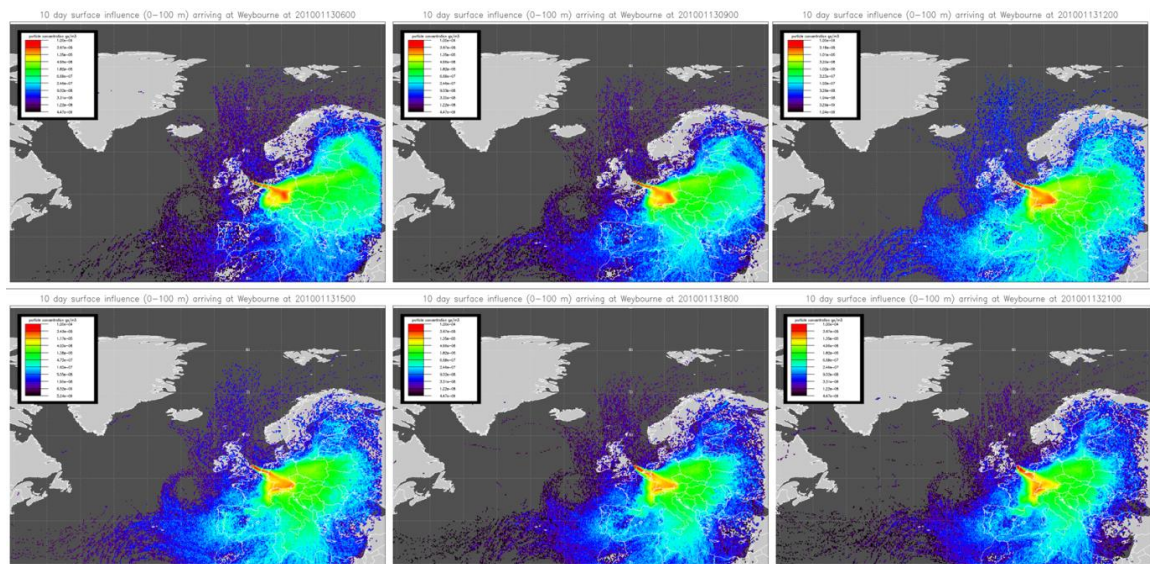
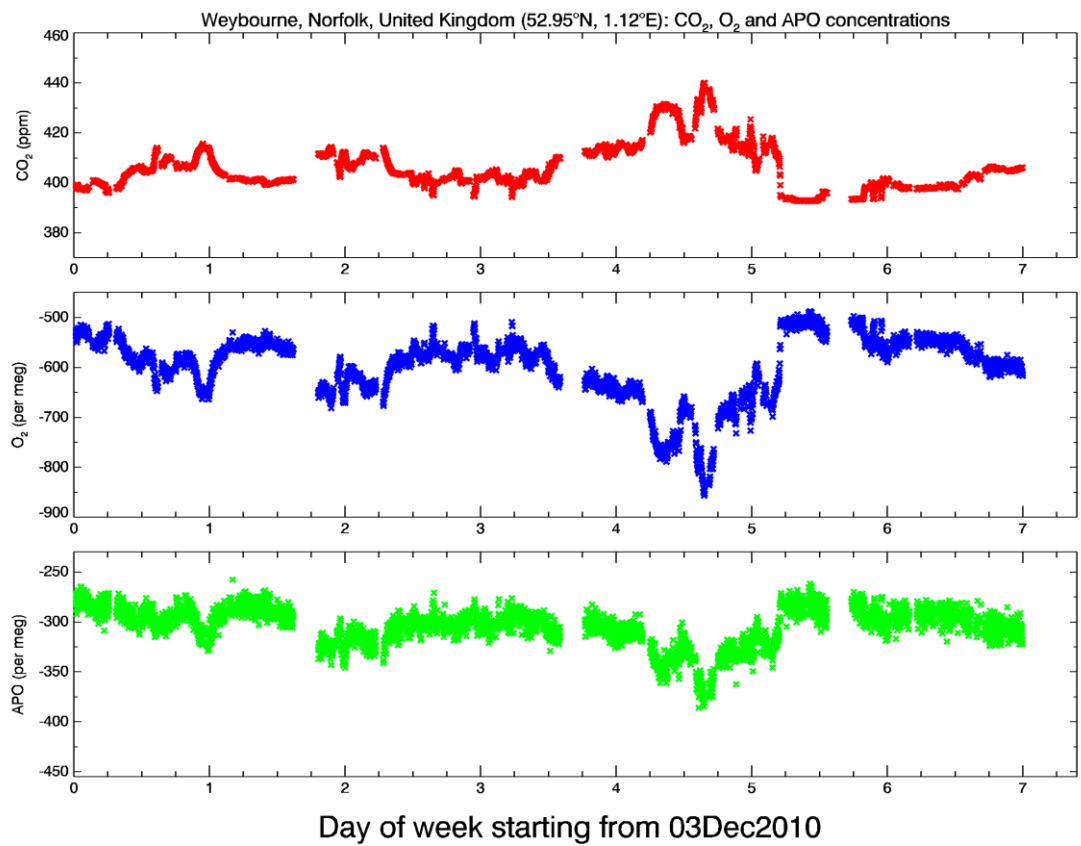
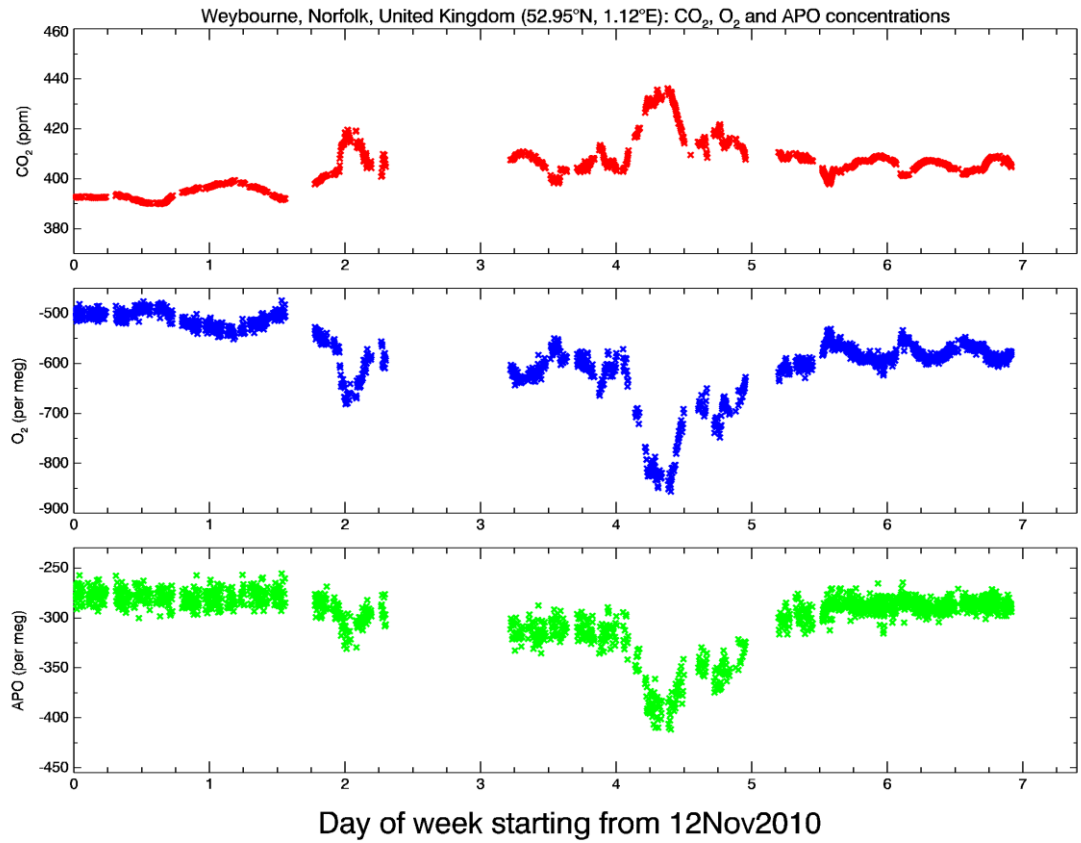


Figure 4.18. Footprints of the air seen at WAO in consecutive 3 hour time windows starting at 06:00 on the 13th January 2010 (top left) and running to 21:00 13th January (bottom right). The scale on each plot is a relative scale in  $\text{g s/m}^3$  and so cannot be directly compared exactly between plots, red and yellow colours indicate higher probabilities of particles and blues lower probabilities.

I next looked at three pollution events in November and December of 2010. Each was a short event lasting for less than 24 hours and each gave quite different  $\text{CO}_2:\text{O}_2$  ratios. The events occurred on the 16<sup>th</sup> November 2010, the 7<sup>th</sup> December 2010 and the 20<sup>th</sup> December 2010. The concentration plots for the three events are shown in Figure 4.19.



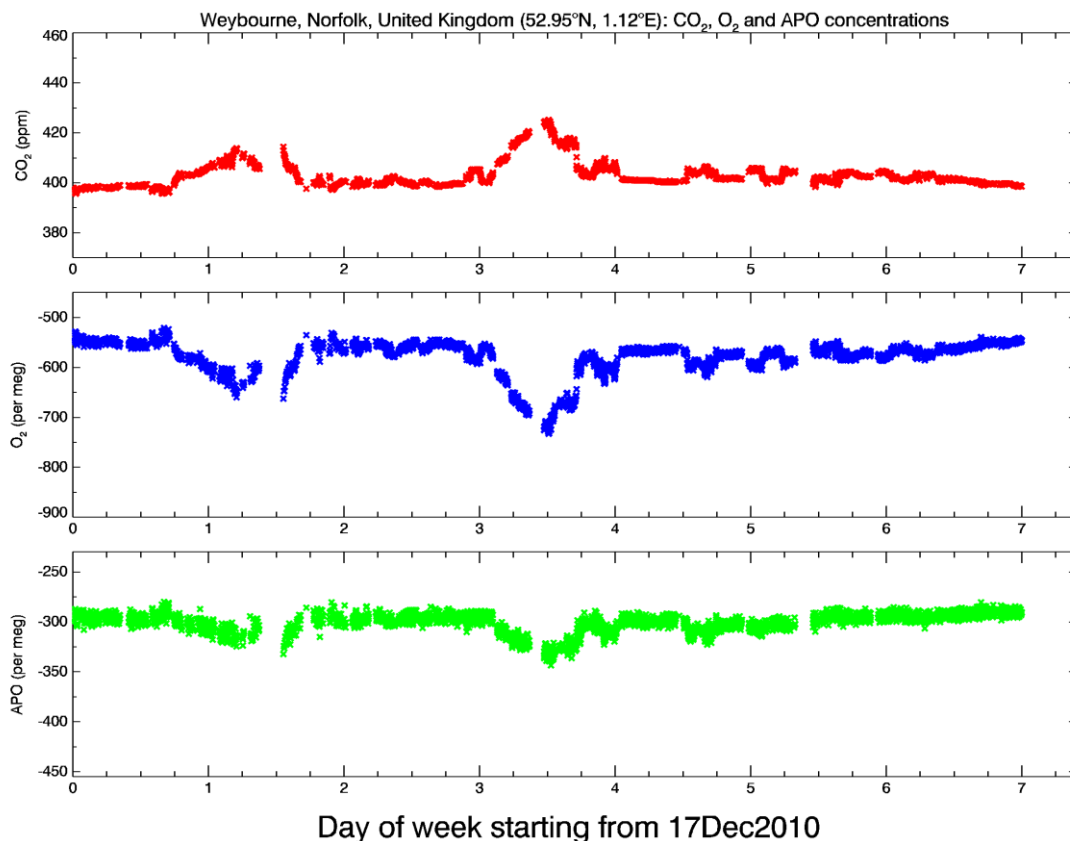


Figure 4.19. Concentration plots of CO<sub>2</sub> (red), O<sub>2</sub> (blue) and APO (green) for three events recorded at WAO. Note that the y-axis for APO is half the range of the O<sub>2</sub> y-axis. The O<sub>2</sub> and CO<sub>2</sub> y-axis are visually comparable. Each week is shown with the same axis to show the relative size of the deviations in concentrations between individual events.

The 2 minute data for each event, while CO<sub>2</sub> was at its maximum values, was plotted using Isoplot to generate the O<sub>2</sub>:CO<sub>2</sub> ratio for the event and the resulting ratios are summarised in table 4.5.

Event date	Time period analysed	O <sub>2</sub> :CO <sub>2</sub> ratio
16 <sup>th</sup> November 2010	04:10 – 11:27	1.63 ±0.15
7 <sup>th</sup> December 2010	06:11 – 18:29	1.420 ±0.029
20 <sup>th</sup> December 2010	06:00 – 16:48	1.284 ±0.043

Table 4.5. Summary of O<sub>2</sub>:CO<sub>2</sub> ratios for three pollution events in November and December 2010. Uncertainties are quoted at the 95% confidence level.

A footprint of the air being sampled at WAO during each event is shown in figure 4.20. Examination of the footprints for the three events shows that during the event on 16<sup>th</sup> November the air being sampled was predominantly from The south of England including London. The O<sub>2</sub>:CO<sub>2</sub> ratio of this air is quite high, 1.63,

indicating that it is polluted air and if it is from a mix of fossil fuels then it must include a significant amount of natural gas. During the event on the 7<sup>th</sup> December the footprint of the air being sampled shows that it has predominantly come from the north of England including industrial cities of the Midlands, Manchester and Sheffield. The O<sub>2</sub>:CO<sub>2</sub> ratio of 1.420 on the 7<sup>th</sup> December is much closer to that for oil and liquid fossil fuels being combusted. On the 20<sup>th</sup> December the footprint for the air being sampled shows that it was dominated by local sources including Norfolk and the north east of England including cities such as Hull. There is also more of a contribution from the Netherlands than for the other 2 events. The O<sub>2</sub>:CO<sub>2</sub> ratio of 1.284 is much lower and suggests that either the polluted air is diluted with clean air from the North Sea or that there is a significant contribution from a coal source bringing the O<sub>2</sub>:CO<sub>2</sub> ratio down.

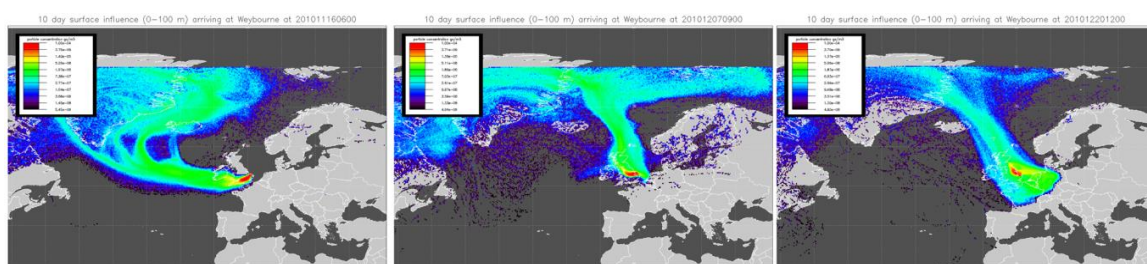


Figure 4.20. Footprints of the air sampled during pollution events observed at WAO on the 16<sup>th</sup> November, 7<sup>th</sup> and 20<sup>th</sup> of December. The scale on each plot is a relative scale in g s/m<sup>3</sup> and so cannot be directly compared exactly between plots, red and yellow colours indicate higher probabilities of particles and blues lower probabilities.

#### 4.6 Examination of clean air and oceanic signals

The situation of WAO and meteorology means that it is rare that it sees completely clean air for an extended period of time. As such it makes it hard to assign a background concentration for WAO and to pick out oceanic events from the short data record we currently have. However one week that clearly shows the potential of the WAO station is the week commencing the 23<sup>rd</sup> July 2011. The concentrations of CO<sub>2</sub>, O<sub>2</sub> and APO for this week are shown in figure 4.21.

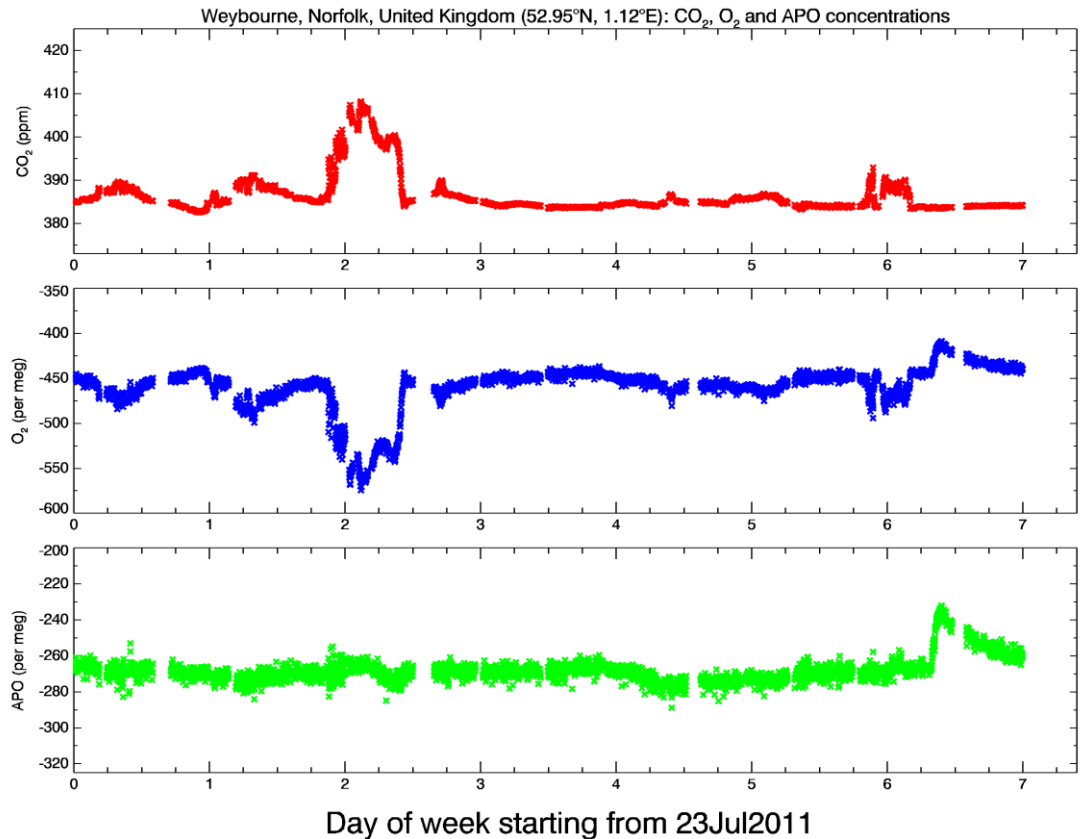


Figure 4.21. Concentrations of CO<sub>2</sub> (red), O<sub>2</sub> (blue) and APO (green) for the one week period 23rd to 29th July inclusive. The y-axis for CO<sub>2</sub> and O<sub>2</sub> are on visually comparable scales and that for APO is half the range of O<sub>2</sub>.

The week starts with quite a clean, stable signal as WAO is seeing air from the Arctic during the 23<sup>rd</sup> and 24<sup>th</sup> of July. Footprints from these 2 days are shown in figure 4.22.

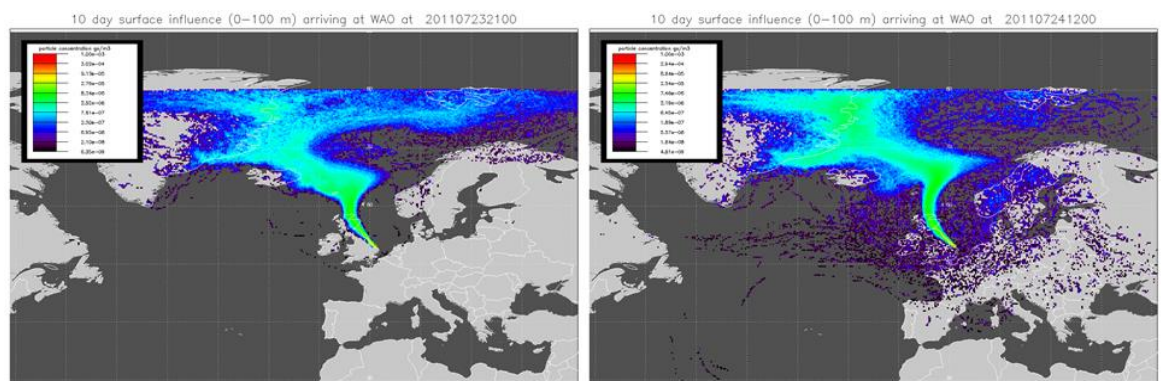


Figure 4.22. Footprints of the location probability of air sampled at WAO for the 10 days prior to the time at which it was sampled for 3 hour periods on the 23<sup>rd</sup> and 24<sup>th</sup> of July 2011. The scale on each plot is a relative scale in g s/m<sup>3</sup> and so cannot be directly compared exactly between plots, red and yellow colours indicate higher probabilities of particles and blues lower probabilities.

Towards the end of the 24<sup>th</sup> of July and into the middle of the 25<sup>th</sup> of July there is quite a large jump in the CO<sub>2</sub> concentrations being sampled. At the same time O<sub>2</sub> concentrations drop and there is a small dip in APO. This is characteristic of polluted air and this is borne out in the footprints that cover this time period. Figure 4.23 shows 3 footprints for 3 hour periods from midnight, 06:00 and 21:00 on the 25<sup>th</sup> July. The sampled air moves west slightly so that by 06:00 on the 25<sup>th</sup> July WAO is sampling air from the north of England and this links up with the polluted concentrations recorded at WAO. By 21:00 the sampled air has shifted back east slightly so once again we are seeing a clean Arctic air signal.

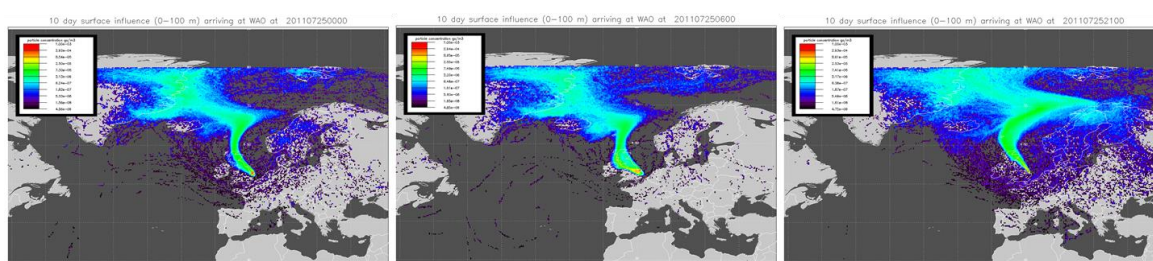


Figure 4.23. Footprints of the location probability of air sampled at WAO for the 10 days prior to the time at which it was sampled for 3 hour periods on the 25<sup>th</sup> of July 2011 starting at 00:00, 06:00 and 21:00. The scale on each plot is a relative scale in g s/m<sup>3</sup> and so cannot be directly compared exactly between plots, red and yellow colours indicate higher probabilities of particles and blues lower probabilities.

Throughout the 26<sup>th</sup> July we see a clean air signal at WAO and concentrations remain very stable. The footprint in figure 4.24 is taken at 12:00 on the 26<sup>th</sup> and is typical of the day as a whole; it shows a clean air signal from the Arctic. The signal remains quite stable throughout the 27<sup>th</sup> but there are signs that the concentrations recorded are slightly noisier. Small peaks in CO<sub>2</sub> and troughs in O<sub>2</sub> can be seen just before midday and towards the end of the day. The footprints for the 27<sup>th</sup> shown in figure 4.24 are from midnight and midday and they show the footprint to be shifting with WAO seeing more of a localised signal from the North Sea. The footprint also shows that WAO will see some air that has recently been present over Northern Europe and the Netherlands. This continental air is likely to be the cause of the slightly noisier signal with small pollution peaks and troughs in CO<sub>2</sub> and O<sub>2</sub>.

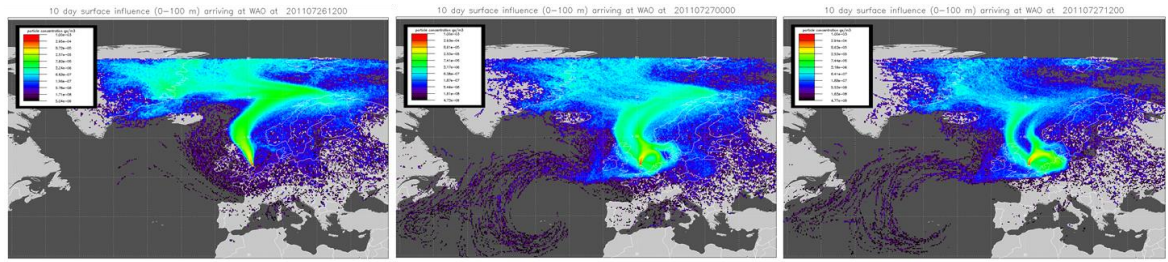


Figure 4.24. Footprints of the location probability of air sampled at WAO for the 10 days prior to the time at which it was sampled for 3 hour periods on the 26<sup>th</sup> of July starting at 12:00, and on the 27<sup>th</sup> July starting at 00:00 and 12:00. The scale on each plot is a relative scale in  $\text{g s/m}^3$  and so cannot be directly compared exactly between plots, red and yellow colours indicate higher probabilities of particles and blues lower probabilities.

Towards the end of the week, the concentrations plotted in figure 4.21 show elevated  $\text{CO}_2$  and depressed  $\text{O}_2$  concentrations at the end of the 28<sup>th</sup> July and into the beginning of the 29<sup>th</sup> July. This signal is indicative of polluted air being sampled and it is then followed by elevated  $\text{O}_2$  concentrations just before midday on the 29<sup>th</sup> which are clearly shown as an elevated APO concentration. This peak gradually reduces but then settles at a slightly higher  $\text{O}_2$  and APO concentration than seen earlier in the week. The footprints for this period in figure 4.25 show that late on the 28<sup>th</sup> the source of the air sampled at WAO is changing as it moves from seeing northern European, North Sea and Arctic air to include some more local sources of pollution from northern England during the early period of the 29<sup>th</sup>. The source continues to move and we can see from the footprints from 09:00 and 12:00 on the 29<sup>th</sup> that the air being sampled at WAO increasingly originates from the north Atlantic and this continues for the rest of the day, as shown by the footprint from 21:00. The air from the North Atlantic has a slightly higher  $\text{O}_2$  content and this is evident in the elevated  $\text{O}_2$  and APO concentrations observed at WAO. The cause of this higher concentration could be summer time outgassing of dissolved  $\text{O}_2$  from the North Atlantic waters as they will be significantly warmer than the Arctic Sea water seen earlier in the week.

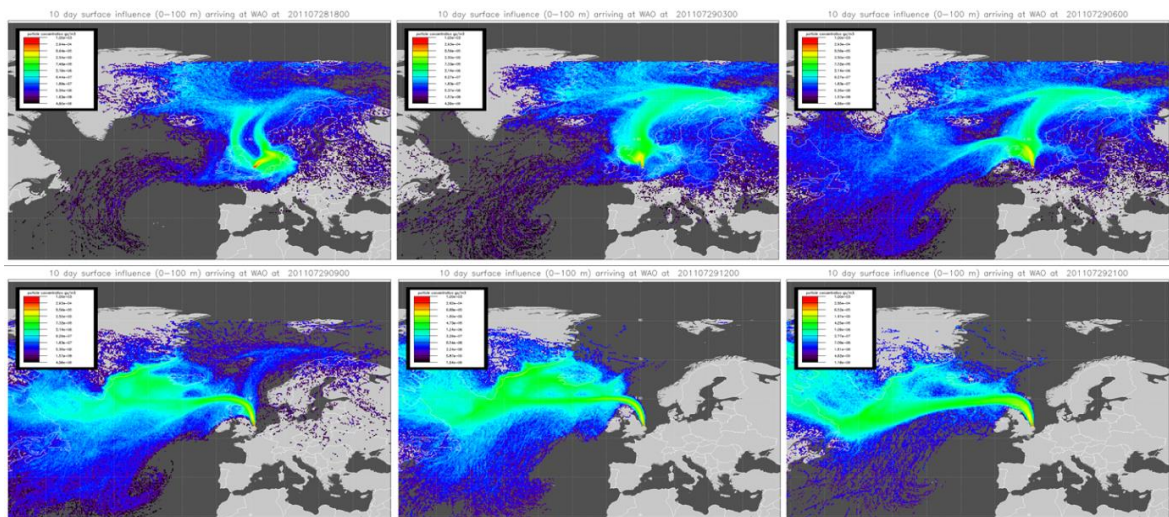


Figure 4.25. Footprints of the location probability of air sampled at WAO for the 10 days prior to the time at which it was sampled for 3 hour periods on the 28<sup>th</sup> of July starting at 18:00, and then on the 29<sup>th</sup> July starting at 03:00, 06:00, 09:00, 12:00 and 21:00. The scale on each plot is a relative scale in  $\text{g s/m}^3$  and so cannot be directly compared exactly between plots, red and yellow colours indicate higher probabilities of particles and blues lower probabilities.

#### 4.7 References

Arya, S. P. S.: Parameterizing the height of the stable atmospheric boundary-layer, *Journal of Applied Meteorology*, 20, 1192-1202, 10.1175/1520-0450(1981)020<1192:pthots>2.0.co;2, 1981.

Deardorf, J. W.: Numerical investigation of neutral and unstable planetary boundary-layers, *Journal of the Atmospheric Sciences*, 29, 91, 10.1175/1520-0469(1972)029<0091:nionau>2.0.co;2, 1972a.

Deardorf, J. W.: Parameterization of planetary boundary-layer for use in general circulation models, *Monthly Weather Review*, 100, 93, 10.1175/1520-0493(1972)100<0093:potpbl>2.3.co;2, 1972b.

Fleming, Z. L., Monks, P. S., and Manning, A. J.: Review: Untangling the influence of air-mass history in interpreting observed atmospheric composition, *Atmospheric Research*, 104, 1-39, 10.1016/j.atmosres.2011.09.009, 2012.

Jones, A., Thomson, D., Hort, M., and Devenish, B.: The UK Met Office's next-generation atmospheric dispersion model, NAME III, *Air Pollution Modeling and Its Applications Xvii*, edited by: Borrego, C., and Norman, A. L., 580-589 pp., 2007.

Keeling, R. F.: Measuring correlations between atmospheric oxygen and carbon dioxide mole fractions: A preliminary study in urban air, *Journal of Atmospheric Chemistry*, 7, 153-176, 1988.

Manning, A. C., and Keeling, R. F.: Global oceanic and land biotic carbon sinks from the Scripps atmospheric oxygen flask sampling network, *Tellus-B*, 58B, 95-116, doi:10.1111/j.1600-0889.2006.00175.x, 2006.

Marland, G., Boden, T. A., and Andres, R. J.: Global, Regional, and National Fossil Fuel CO<sub>2</sub> Emissions. In *Trends: A Compendium of Data on Global Change, Carbon Dioxide Information Analysis Center, Oak Ridge National Laboratory, U.S. Department of Energy, Oak Ridge, Tenn., U.S.A.*, 2008.

Ryall, D. B., and Maryon, R. H.: Validation of the UK Met. Office's name model against the ETEX dataset, *Atmospheric Environment*, 32, 4265-4276, 10.1016/s1352-2310(98)00177-0, 1998.

Severinghaus, J. P.: Studies of the terrestrial O<sub>2</sub> and carbon cycles in sand dune gases and in Biosphere 2, Columbia University, New York, U.S.A., 148 pp., 1995.

Stohl, A., Eckhardt, S., Forster, C., James, P., Spichtinger, N., and Seibert, P.: A replacement for simple back trajectory calculations in the interpretation of atmospheric trace substance measurements, *Atmospheric Environment*, 36, 4635-4648, 10.1016/s1352-2310(02)00416-8, 2002.

Zilitinkevich, S., and Baklanov, A.: Calculation Of The Height Of The Stable Boundary Layer In Practical Applications, *Boundary-Layer Meteorology*, 105, 389-409, 10.1023/a:1020376832738, 2002.

## **CHAPTER 5 - CONCLUSIONS AND OUTLOOK**

My thesis describes a new, in situ, continuous data set of high precision atmospheric CO<sub>2</sub> and O<sub>2</sub> measurements that I have collected at the Weybourne Atmospheric Observatory on the north Norfolk coast in the United Kingdom (52.95°N, 1.12°E). This is the first station ever to measure atmospheric CO<sub>2</sub> and O<sub>2</sub> in situ in the United Kingdom and is a valuable addition to the global network of greenhouse gas monitoring stations. This is particularly true for atmospheric O<sub>2</sub> since the number of sites measuring O<sub>2</sub> worldwide remains small – of the order of 25 – owing to the difficulty in making high precision measurements of O<sub>2</sub>.

A number of changes and upgrades I made to the analytical measurement system throughout 2009 have greatly improved the quality of the more recent data compared to the early period of data collection in 2007 and 2008. I improved the data quality of the early period via careful data processing and examining old station notebooks, however, further work is still needed, in particular to bring the calibration scales defined during this period in line with the more recent data. It was not possible to do this work in the timeframe of my thesis as it requires reanalysis of a number of calibration standards in the laboratories of international collaborators.

Based on so-called ‘Target Tank’ (TT) measurements since 2010, I demonstrate that the precision of the measurements are within the compatibility goals established by the United Nations World Meteorological Organization (WMO) for both CO<sub>2</sub> and O<sub>2</sub>. Based on 1228 consecutive pairs of TT measurements covering the period from August 2010 to April 2012, the average standard deviation between pairs, used as a measure for precision, is  $\pm 0.02$  ppm for CO<sub>2</sub> (WMO goal:  $\pm 0.1$  ppm) and  $\pm 1.1$  per meg for O<sub>2</sub> (WMO goal:  $\pm 2$  per meg). Taking half the value of the WMO compatibility goal as a guideline for internal repeatability (Manning and Crotwell, 2012), I do achieve this for CO<sub>2</sub> and am just outside of this goal for O<sub>2</sub>. The O<sub>2</sub> goal is particularly challenging to meet and my repeatability value compares very well with other laboratories around the world. Using data from ambient air measurements gives a more conservative estimate of the performance of the full analytical system, rather than measuring a high pressure cylinder, which does not pass through the air inlets, sample pump, and full drying system. The

standard deviation of thirty 2-minute data points taken during an hour of measurements when ambient concentrations remained stable gave a CO<sub>2</sub> precision of  $\pm 0.03$  ppm and an O<sub>2</sub> precision of  $\pm 2.0$  per meg, again both within the WMO guidelines. The short-term precision over a ten minute period is  $\pm 2.0$  per meg for O<sub>2</sub> and  $\pm 0.02$  ppm for CO<sub>2</sub> (calculated from standard deviations of the mean of 2 minute data points). The fact that these figures are based on different time periods and from different sources of air yet remain close to one another suggests that they do indeed provide a good indication of the system precision.

Despite the fact that precision is within the WMO compatibility guidelines for both CO<sub>2</sub> and O<sub>2</sub>, it is an ongoing and constant challenge to ensure that the performance of the system remains at this level or better. Careful diagnostic analyses must be performed regularly (several times per week) to ensure continuing data quality; in the case of WAO, I have largely automated such work via automated processing and plotting of a wide range of diagnostic parameters of the system such as pressures, temperatures and flow rates. O<sub>2</sub> precision can be compromised in a number of ways that must be monitored and prevented, for example by leaks or from aging fuel cells. Other areas can also be identified to improve O<sub>2</sub> precision, for example it is planned to replace the standard Swagelok 'tee' fitting used to connect all pressure sensors with one incorporating a dip tube in the shaft of the pressure sensor to further minimise dead volume and to help eliminate possible O<sub>2</sub>/N<sub>2</sub> fractionation at the tee (Stephens et al., 2007). In addition, I have realised that it is possible to achieve even better precision values from a Siemens Ultramat NDIR CO<sub>2</sub> analyser (Kozlova and Manning, 2009) and so this will be a focus of improvements made on the WAO O<sub>2</sub> and CO<sub>2</sub> system in the very near future. It is also important going forward to maintain close contacts with the larger carbon cycle community with respect to ongoing technological advancements in the field, and to continue regular involvement in intercomparison and round robin activities such as the international GOLLUM ([www.gollum.uea.ac.uk](http://www.gollum.uea.ac.uk)), Cucumbers ([www.cucumbers.uea.ac.uk](http://www.cucumbers.uea.ac.uk)) and WMO Round Robin programmes.

Plots of Working Tank (WT) concentrations as defined after every Working Secondary Standard (WSS) calibration for both CO<sub>2</sub> and O<sub>2</sub>, showed that O<sub>2</sub> concentrations in the WTs became depleted as pressure in the cylinders decreased.

This has been noted previously by Manning (2001) and by Kozlova and Manning (2009). The O<sub>2</sub> depletions experienced at WAO were generally less than 2 ppmEquiv, in line with Manning (2001). No consistent depletion effect was noted in CO<sub>2</sub> concentrations. The O<sub>2</sub> depletion is insightful in terms of possible implications to the stability of O<sub>2</sub> in primary and secondary calibration standards, but is not a problem, however, in WTs, since part of my calibration methodology is to allow WT concentrations to be redefined after every WSS calibration, and then to use this redefinition until the subsequent WSS calibration.

In chapter 3, the data records of atmospheric CO<sub>2</sub>, O<sub>2</sub> and the tracer Atmospheric Potential Oxygen (APO) were presented along with curve fits applied to the data using the Fortran 'Hpspline' program. APO is a tracer defined as O<sub>2</sub> + 1.1 x CO<sub>2</sub> and is conservative with respect to land biosphere processes. It is thus an atmospheric indicator of oceanic processes, and of fossil fuel combustion. From the WAO curve fits I found that atmospheric CO<sub>2</sub> is increasing by about 2.4 ppm yr<sup>-1</sup> while O<sub>2</sub> is decreasing by about 25 per meg yr<sup>-1</sup> and APO is also decreasing by about 13 per meg yr<sup>-1</sup>. These values agree well with data from other European stations at similar latitudes (Thompson et al., 2009; van der Laan-Luijkx et al., 2010; Kozlova et al., 2008; Popa et al., 2010), when taking into account station location and the fact that fossil fuel emissions are accelerating again, following a slow-down during the global financial crisis in 2008 – 2009 (Peters et al., 2012) that influenced the records from other stations.

The length of my WAO data record makes a thorough investigation of interannual variability in growth rates impossible, but a preliminary investigation showed some variability that could be linked to UK fossil fuel burning from bottom-up inventories. This work should be repeated and updated as the WAO record grows, and when the calibration issues in the 2007 and 2008 data are rectified. Also as the data record grows, the parameters used in the Hpspline curve fits should be reanalysed so that interannual variability is incorporated into the fits.

The average amplitude of the seasonal cycles observed at WAO between 2009 and 2012 was about 15 ppm for CO<sub>2</sub>, 134 per meg for O<sub>2</sub> and 59 per meg for APO. The fact that the APO amplitude is approximately half of the O<sub>2</sub> amplitude suggests that

oceanic and terrestrial processes contribute in approximately equal measures to the O<sub>2</sub> seasonality observed at WAO. The amplitude values are in line with those reported by other coastal stations at similar latitudes that also have a significant contribution from the terrestrial biosphere in the concentrations that they observe.

I performed a comparison of the observed APO seasonal cycle with that predicted by an Ocean General Circulation Model (OGCM) forced by meteorological values from three different sources, and coupled to a marine biogeochemistry model. This comparison appeared to show that the APO seasonality observed at WAO is in closest agreement to the model results for the circumpolar region north of 45°N, rather than the smaller, more localised regions investigated. This is indicative of the air masses arriving at WAO being influenced by and representative of a large area. This model – data comparison work is preliminary and could be extended, for example by examining the influence of filtering the WAO observations based on the back trajectory history of the sampled air, repeating with a longer observational record, using heat fluxes to provide a better estimation of APO concentrations by incorporating the effect of oceanic N<sub>2</sub> fluxes, and incorporating APO observations of additional coastal European stations, and finally by comparing with other marine biogeochemistry models (see e.g. Stephens et al., 1998; Battle et al., 2006). Finally, ‘inverting’ the WAO APO observations with an atmospheric transport model could result in quantifying APO fluxes as determined by the concentration measurements, which could then be directly compared to the model simulation flux results.

The ranges of atmospheric concentrations routinely observed at WAO on seasonal and shorter time scales show that WAO experiences air masses from a variety of different sources. This is also reflected in the fact that the Hpspline curve fits do not follow what would be considered a ‘clean-air’ or ‘background’ signal, owing to contributions from local terrestrial biosphere and pollution. The variety of air masses experienced is also reflected in the fact that the APO seasonal variability observed agreed most closely with the largest geographic region modelled.

In Chapter 4 I examined in more detail the shorter term variations experienced at WAO and discussed the different possible causes of these variations. A clear diurnal cycle can often be observed in the WAO CO<sub>2</sub> and O<sub>2</sub> data. This cycle is mainly driven by changes in atmospheric boundary layer height leading to the diurnal rectifier effect. CO<sub>2</sub> concentrations increase and reach a maximum overnight as respiration dominates while the ABL is lower due to lower temperatures and less convection. CO<sub>2</sub> concentrations then decrease during the day when the ABL rises and therefore dilutes the surface concentrations measured at WAO. During the day photosynthesis is the dominant process but it is hard to discern direct photosynthetic signals from the rectifier effect. O<sub>2</sub> concentrations are anti-correlated to the CO<sub>2</sub> concentrations, reflecting the stoichiometric link of the two species in the processes respiration and also photosynthesis, although this plays a more minor role in the diurnal observations. The magnitude of the diurnal cycles in CO<sub>2</sub> and O<sub>2</sub> vary seasonally throughout the year reflecting the change in magnitude of the difference between day time and night time ABL heights throughout the year and also the activity of the terrestrial biosphere from season to season. In the winter months, when terrestrial biosphere activity is low and there are 8 hours of daylight or less, the diurnal amplitude becomes almost indiscernible, whereas in the summer months, diurnal amplitudes are greatest. APO does not exhibit a diurnal cycle at WAO, since the oceanic processes primarily responsible for variations in APO do not occur quickly enough to be visible on a diurnal timescale. Although some ocean events such as upwelling or ventilation, and phytoplankton blooms can occur very rapidly, and do influence O<sub>2</sub> and CO<sub>2</sub> concentrations in the water column, these changes are not reflected in atmospheric variability on diurnal time scales since air-sea equilibration times are much slower than daily time scales.

Examination of the meteorological data collected at WAO reveals that the dominant wind sector for air masses arriving at WAO is the south west quadrant. WAO does experience air from all directions, depending on the weather conditions, and appears to experience a larger than usual influence from the north east quadrant during the spring months of March, April and May.

Binning data based on the wind direction at the time of sampling into four regions (the North Sea, continental Europe, south England and London, north England and Scotland) and then reprocessing these filtered data with Hpspline reveals some differences in the curve fits. The magnitude of seasonal amplitudes are markedly higher for air arriving from the European sector reflecting the influence of continental Europe and the large associated terrestrial biosphere. This, however, is a somewhat crude method of filtering data; the nature of atmospheric circulation patterns suggest that air arriving at WAO from one sector may have had a significant influence from other sectors before arriving at Weybourne. This is illustrated particularly well by the UK Met Office's Numerical Atmospheric dispersion Modelling Environment (NAME model) back trajectory 'footprints' showing 10 day histories of air masses before they are sampled at Weybourne. Looking forward, it should be possible to use the NAME footprints to filter data and separate out the different signals observed at WAO to build up individual time series of the different signals. Such a data filtering technique has been used to determine 'baseline' concentrations for different atmospheric species at the Mace Head, Ireland monitoring station (Manning et al., 2011).

A number of different events observed at WAO were identified based on CO<sub>2</sub>, O<sub>2</sub> and APO concentrations and these were examined in more detail. Pollution signals could be clearly observed and were identified in air that had recently passed over southern England, the Midlands and industrial northern England or from Europe. The O<sub>2</sub>:CO<sub>2</sub> ratios of this polluted air were found to be characteristically high with ratios ranging from 1.2 to 1.6. These ratios are indicative of a pollution signal caused by fossil fuels and the range of values could represent different mixes of fossil fuel sources being observed (Keeling, 1988; Manning and Keeling, 2006).

Stable air observations were also explored, and showed that WAO sometimes experiences background signals, and sometimes with a significant oceanic influence from both the North Atlantic Ocean and from the Arctic Ocean. This result suggests that WAO has the capacity to observe oceanic events and that it may be possible to use footprint based filtering to define a background concentration for the WAO data as the record is extended into the future.

As a summary to my thesis, a high precision, in situ, continuous measurement system for CO<sub>2</sub> and O<sub>2</sub> has been developed and a data record begun at WAO. A single air sampling line is used to make concurrent, continuous measurements of both CO<sub>2</sub> and O<sub>2</sub>, and connecting the two analysers in series in such a manner is a particularly useful and calibration gas-efficient method of making these measurements. This WAO system is the first continuous, high precision atmospheric CO<sub>2</sub> and O<sub>2</sub> system making measurements in the United Kingdom. Continuous measurements offer significant advantages over discrete flask sampling, for example to identify the causes of short-term phenomena and variations in atmospheric signals. For the time series to be of most use, the data record must be maintained and data processed and analysed on a regular basis. This will allow better investigation of interannual variability observed at WAO, and will maintain or improve the precision and compatibility of the data. The use of back trajectory footprints are extremely useful in identifying the history of sampled air and are of great help in attributing different events and signatures to the observations of O<sub>2</sub> and CO<sub>2</sub>. The fact that WAO experiences air from a variety of sources, UK, continental Europe, Arctic and Atlantic should be an advantage to the station as it could contribute to regional studies focussed on any of these areas. One possible future application could be to help independently verify the UK's anthropogenic greenhouse gas emissions. There is also work presently underway to extend the WAO analytical system to include a Gas Chromatograph (GC) for measuring other major greenhouse gases (CH<sub>4</sub>, N<sub>2</sub>O, SF<sub>6</sub>) that will provide a suite of complementary measurements and extend the potential use of the O<sub>2</sub> and CO<sub>2</sub> data records via multi-species analysis, for example as carried out in exploratory fashion in Worthy et al. (2009) and Kozlova (2010).

## 5.1 References

Battle, M., Mikaloff Fletcher, S., Bender, M. L., Keeling, R. F., Manning, A. C., Gruber, N., Tans, P. P., Hendricks, M. B., Ho, D. T., Simonds, C., Mika, R., and Paplawsky, B.: Atmospheric potential oxygen: New observations and their implications for some atmospheric and oceanic models, *Global Biogeochemical Cycles*, 20, doi:10.1029/2005GB002534, 2006.

- Keeling, R. F.: Measuring correlations between atmospheric oxygen and carbon dioxide mole fractions: A preliminary study in urban air, *Journal of Atmospheric Chemistry*, 7, 153-176, 1988.
- Kozlova, E. A., Manning, A. C., Kisilyakhov, Y., Seifert, T., and Heimann, M.: Seasonal, synoptic, and diurnal scale variability of biogeochemical trace gases and O<sub>2</sub> from a 300 m tall tower in central Siberia, *Global Biogeochemical Cycles*, 22, 10.1029/2008GB003209, 2008.
- Kozlova, E. A., and Manning, A. C.: Methodology and calibration for continuous measurements of biogeochemical trace gas and O<sub>2</sub> concentrations from a 300-m tall tower in central Siberia, *Atmospheric Measurement Techniques*, 2, 205-220, 10.5194/amt-2-205-2009, 2009.
- Kozlova, E. A.: Multi-Species Atmospheric Continuous Measurements as a Tool to Study Changes in the Carbon Cycle, School of Environmental Sciences, University of East Anglia, Norwich, 218 pp., 2010.
- Manning, A. C.: Temporal variability of atmospheric oxygen from both continuous measurements and a flask sampling network: Tools for studying the global carbon cycle, Scripps Institution of Oceanography, University of California, San Diego, La Jolla, California, U.S.A., 202 pp., 2001.
- Manning, A. C., and Keeling, R. F.: Global oceanic and land biotic carbon sinks from the Scripps atmospheric oxygen flask sampling network, *Tellus-B*, 58B, 95-116, doi:10.1111/j.1600-0889.2006.00175.x, 2006.
- Manning, A. C., and Croftwell, A. M.: Minimising uncertainty and error in atmospheric measurement of CO<sub>2</sub>: Part I. Analysers, calibration and gas handling, *Atmos. Meas. Tech. Discuss.*, *submitted*, 2012.
- Manning, A. J., O'Doherty, S., Jones, A. R., Simmonds, P. G., and Derwent, R. G.: Estimating UK methane and nitrous oxide emissions from 1990 to 2007 using an inversion modeling approach, *Journal of Geophysical Research-Atmospheres*, 116, 10.1029/2010jd014763, 2011.
- Peters, G. P., Marland, G., Le Quere, C., Boden, T., Canadell, J. G., and Raupach, M. R.: Rapid growth in CO<sub>2</sub> emissions after the 2008-2009 global financial crisis, *Nature Clim. Change*, 2, 2-4, 10.1038/nclimate1332, 2012.
- Popa, M. E., Gloor, M., Manning, A. C., Jordan, A., Schultz, U., Haensel, F., Seifert, T., and Heimann, M.: Measurements of greenhouse gases and related tracers at Białystok tall tower station in Poland, *Atmospheric Measurement Techniques*, 3, 407-427, 10.5194/amt-3-407-2010, 2010.
- Stephens, B. B., Keeling, R. F., Heimann, M., Six, K. D., Murnane, R., and Caldeira, K.: Testing global ocean carbon cycle models using measurements of atmospheric O<sub>2</sub> and CO<sub>2</sub> concentration, *Global Biogeochemical Cycles*, 12, 213-230, 1998.

Stephens, B. B., Bakwin, P. S., Tans, P. P., Teclaw, R. M., and Baumann, D. D.: Application of a differential fuel-cell analyzer for measuring atmospheric oxygen variations, *Journal of Atmospheric and Oceanic Technology*, 24, 82-94, doi:10.1175/JTECH1959.1171, 2007.

Thompson, R. L., Manning, A. C., Gloor, E., Schultz, U., Seifert, T., Hänsel, F., Jordan, A., and Heimann, M.: In-situ measurements of oxygen, carbon monoxide and greenhouse gases from Ochsenkopf tall tower in Germany, *Atmospheric Measurement Techniques*, 2, 573-591, 10.5194/amt-2-573-2009, 2009.

van der Laan-Luijkx, I. T., Karstens, U., Steinbach, J., Gerbig, C., Sirignano, C., Neubert, R. E. M., van der Laan, S., and Meijer, H. A. J.: CO<sub>2</sub>, ΔO<sub>2</sub>/N<sub>2</sub> and APO: observations from the Lutjewad, Mace Head and F3 platform flask sampling network, *Atmos. Chem. Phys.*, 10, 10691-10704, 10.5194/acp-10-10691-2010, 2010.

Worthy, D. E. J., Chan, E., Ishizawa, M., Chan, D., Poss, C., Dlugokencky, E. J., Maksyutov, S., and Levin, I.: Decreasing anthropogenic methane emissions in Europe and Siberia inferred from continuous carbon dioxide and methane observations at Alert, Canada, *Journal of Geophysical Research-Atmospheres*, 114, 10.1029/2008jd011239, 2009.

## **ABBREVIATIONS**

ABL - Atmospheric Boundary Layer  
a.g.l. - above ground level  
a.s.l. - above sea level  
APO - Atmospheric Potential Oxygen  
BGC - Berkeley Geochronology Centre  
CCL - Central Calibration Laboratory  
CFC - Chlorofluorocarbon  
CO - Carbon monoxide  
CO<sub>2</sub> - Carbon dioxide  
CO<sub>3</sub><sup>2-</sup> - Carbonate  
CSV - Comma Separated Values  
CT - Cold Trap  
DIC - Dissolved Inorganic Carbon  
ECMWF - European Centre for Medium-Range Weather Forecasts  
FT - Fridge Trap  
GC – Gas Chromatograph  
GDP - Gross Domestic Product  
GOLLUM - Global Oxygen Laboratories Link Ultra-precise Measurements  
GHG – Greenhouse Gas  
H<sub>2</sub> - Hydrogen  
H<sub>2</sub>CO<sub>3</sub> - Carbonic acid  
HCO<sub>3</sub><sup>-</sup> - Bicarbonate  
HFC - Hydrofluorocarbon  
ID - Inner Diameter  
IPCC – Intergovernmental Panel on Climate Change  
JPL - Jet Propulsion laboratory, USA  
LSCE - Laboratoire des Sciences du Climat et de l'Environnement, France  
MFC - Mass Flow Controller  
MPI-BGC - Max Planck Institute for Biogeochemistry, Germany  
N<sub>2</sub> - Nitrogen  
NAME - Numerical Atmospheric dispersion Modelling Environment  
NCAR - National Center for Atmospheric Research, USA

NCAS - National Centre for Atmospheric Science, USA  
NCEP - National Center for Environmental Prediction, USA  
NIES - National Institute for Environmental Studies, Japan  
NIWA - National Institute of Water and Atmospheric Research, New Zealand  
NO - Nitrous oxide  
NO<sub>2</sub> - Nitrous dioxide  
NOAA - National Oceanic and Atmospheric Administration, USA  
NDIR - Non-Dispersive Infra Red  
O<sub>2</sub> - Oxygen  
O<sub>3</sub> - Ozone  
OD - Outer Diameter  
OGCM - Ocean General Circulation Model  
SIO - Scripps Institution of Oceanography  
SO<sub>2</sub> - Sulphur dioxide  
TT - Target Tank  
UEA - University of East Anglia  
UK - United Kingdom  
USA - United States of America  
USB - Universal Serial Bus  
WAO - Weybourne Atmospheric Observatory  
WMO - World Meteorological Organisation  
WSS - Working Secondary Standard  
WT - Working Tank  
ZT - Zero Tank